ABSTRACT

An In-Line Microwave Steam Quality Sensor

Christopher D. Faulkner, M.S.E.C.E

Mentor: B. Randall Jean, Ph.D.

Saturated steam is a widely used industrial medium for the efficient transfer of
energy. The proportion of saturated vapor steam to saturated condensate of the steam mixture
is referred to as the steam quality. Accurate and reliable measurements of steam quality
provides critical information for process control that effects the efficiency of energy transfer
as well as protecting machine parts that come in contact with the steam mixture flow. Though
many methods currently exist for measuring steam quality all have significant drawbacks in
their use because of the measurement mode used.

This thesis describes a microwave sensor that uses the permittivity of the steam
mixture to enable an accurate and inline measurement of the quality of steam. A documented
history of the theory, design, development, and testing is describe herein, with ending
commentary on project potential.

An In-Line Microwave Steam Quality Sensor

by

Christopher D. Faulkner, B.S.

A Thesis

Approved by the Department of Electrical and Computer Engineering

_____

Kwang Y. Lee, Ph.D, Chairperson

Submitted to the Graduate Faculty of
Baylor University in Partial Fulfillment of the
Requirements for the Degree
of

Master of Science in Electrical and Computer Engineering

Approved by the Thesis Committee

_____

B. Randall Jean, Ph.D., Chairperson

_____

Yang Li, Ph. D

_____

Stephen T. McClain, Ph.D.

Accepted by the Graduate School

May 2014

_____

J. Larry Lyon, Ph.D., Dean

TABLE OF CONTENTS

LIST OF FIGURES

LIST OF TABLES

LIST OF ABBREVIATIONS

AL – Aluminum

CFM – Cubic Feet per Minute

CSRR- Complementary Split Ring Resonator

CST MWS – CST Microwave Studio

E-field – Electric Field

EOR – Enhanced Oil Recovery

FFT – Fast Fourier Transform

GMS – Guided Microwave Spectrometer

GPM – Gallons Per Minute

H-field – Magnetic Field

ID –Inner Diameter

OD – Outer Diameter

OP – Orifice Plate

PDNA – Pulsed Dispersion Network Analyzer

PEC- Perfect Electrical Conductor

PMC – Perfect Magnetic Conductor

POC – Proof of Concept

PPWG – Parallel Plate Waveguide

PVC – Polyvinyl Chloride

RF – Radio Frequency

RPM – (unit) Revolutions per Minute

R^2 – Coefficient of Determination

RWG – Rectangular Waveguide

SAGD – Steam Assisted Gravity Drainage

SMA – Subminiature version A

SRR– Split Ring Resonator

SS – Stainless Steel

SQ – Steam Quality

SQS – Steam Quality Sensor

TEM – Transverse Electromagnetic Mode

VME – Volumetric Mixing Equation

VNA – Vector Network Analyzer

Z_{xxxx} – characteristic impedance of the transmission line section named "xxxx"

Z_{CL} – characteristic impedance of the coupling line section

Z_0 – characteristic impedance of a transmission line

ACKNOWLEDGMENTS

CHAPTER ONE

Background

1.1 Motivation

Measuring a material's permittivity provides an accurate and repeatable method of precisely determining the relative composition of unknown mixture of known materials. Permittivity is the measure of resistance to the formation of an electric field (E-field) in the material. Coupling electromagnetic fields into steam allows the steam's effective permittivity to be observed. The application of material mixing models and observations of electromagnetic wave propagation in the steam can be used to determine the steam's quality.

Steam describes the state of water when heated to the vapor phase. The properties of saturated steam can be represented by a two-phase region on a temperature-enthalpy diagram Fig. 1, where H_2O can exist as either water (liquid phase) or steam (vapor phase) depending upon the enthalpy of H_2O. In thermodynamics, steam quality (SQ) is the mass ratio of the vaporous steam to the total mixture mass of the vapor and liquid components, (1).

$$SQ = \frac{m_{vapor}}{m_{vapor} + m_{liquid}} \qquad (1)$$

Saturated steam is fundamentally a mixture of liquid and vapor H_2O, only the constituents are two phases of H_2O instead of different materials. Saturated steam exists along constant temperature lines on a pressure-enthalpy diagram; where in the input of energy to the steam only raises its enthalpy and quality, not its pressure. The quality of steam

1

is often approximated by use of a calorimeter, but these devices are inaccurate and possess limitations [1]. The accuracy of a process controls SQ measurement determines the efficiency at which energy can be transferred and equipment lifespan guaranteed. The lower enthalpy of low quality steam reduces the energy transfer of fixed mass flow steam loops forcing the operator to run the system longer to achieve the same energy transfer. A low SQ is avoided in wet-steam turbines where water drop erosion of the high speed turbine blades reduces turbine reliability. To avoid water droplet formation caused by low quality steam from damaging the turbines careful and accurate steam quality measurement is necessary. Thus a market exists for a low cost instrument capable of measuring steam quality to a higher accuracy than currently available using a calorimeter device.
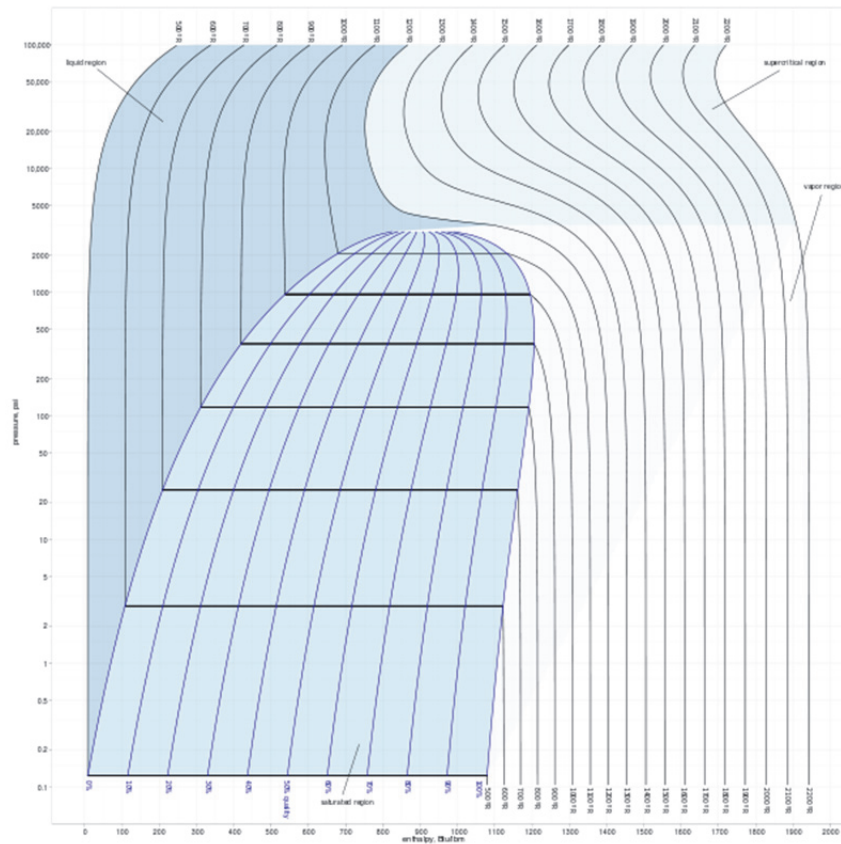
Fig. 1: Pressure-Enthalpy Diagram Steam [2]

1.2 Orifice Plates

A common low-cost technique for measuring flow rate in a pipe is inserting an orifice plate (OP) into the flow, Fig. 2. An orifice plate is a metallic disk that has had a bore hole machined into it. Placement and shape of the bore hole vary depending on purpose and manufacturer, but it is commonly a circular bore located in the center of the plate. The ratio of the diameter of the bore hole to the diameter of the process pipe is referred to as the orifice plate's beta value.
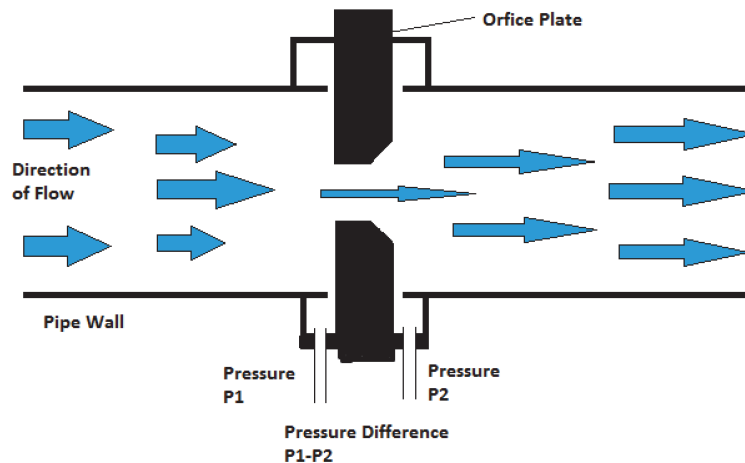
Fig. 2: Orifice Plate as Mass Flow Rate Meter

The constriction produced by the plate causes the flow to accelerate, thereby producing a pressure drop across the OP as the flow velocity increases. The pressure differential created across the OP enables the calculation of mass flow rate of the fluid using the Bernoulli principle. The Bernoulli principle method of flow rate measurement, shown in Fig. 2, requires minimal equipment: two flanges, an orifice plate, and a differential pressure meter which makes such a measurement low cost. For fluids that can be modeled as incompressible, such as saturated steam, there is a permanent pressure drop that occurs and is a function of the orifice plate's beta value. The permanent pressure loss increases with

smaller beta values. Large amounts of permanent pressure loss are undesirable to the operator

of the steam system so small beta orifice plates are not preferred s they increase operating

costs. The alternative structure with which a Bernoulli principle measurement can be made

is a venture tube. The permanent pressure drop of a venture tube is much less than an orifice

plate, but costs many times more as their manufacture is more complex.

The characterization of orifice plates is done by their pressure rating and their beta

factor. The beta of an orifice plate is the ratio of the inner diameter of the pipe to the diameter

of the plate bore in the orifice plate as shown in (2). The mass flow rate of the fluid can then

be calculated using the calculated beta and known fluid density via the Bernoulli equation,

(3). [3, p. 109:120]

$$\beta = \frac{D_{Bore}}{D_{PIPE,ID}} \tag{2}$$

$$\dot{m} = \frac{C_d}{\sqrt{1-\beta^4}} A_2 \sqrt{2\rho * (P_1 - P_2)} \tag{3}$$

1.3 Steam Quality and Permittivity

Jean [4] had previously built a steam quality sensor using a differential path length

approach which provided excellent sensitivity to permittivity changes a point in the process

pipe. In doing so, Jean developed a volumetric mixing equation for use in two material

mixtures to determine the effective permittivity of the water steam mixture in terms of steam

quality and used here forth to model the permittivity of steam at varying qualities.

$$\varepsilon_{eff}(SQ) = \left[\frac{SQ \cdot (\frac{\rho_w}{\rho_s})}{1 + \left(\frac{\rho_w}{\rho_s} - 1\right) \cdot SQ} \cdot \sqrt{\varepsilon_s} + \frac{1 - SQ}{1 + \left(\frac{\rho_w}{\rho_s} - 1\right) \cdot SQ} \cdot \sqrt{\varepsilon_w} \right]^{1/2} \tag{4}$$

4

The relationship between steam quality and permittivity is shown in Fig. 3. The densities and permittivities of the components were at a temperature of 340 ^{O}F and at 1.03Mpa with quality values ranging from 30% to 100%. Note the variance in the permittivity is very small at higher qualities with a 1% change in SQ resulting in a difference in permittivity less than 0.01for steam above 70% quality. Below 30% SQ, the change in permittivity per unit quality is so large that a microwave technique capable of detecting above 70% will be sufficient for the lower end measurements. The model does rely on accurate pressure and temperature information to establish both the density and static permittivity of water and steam. Precompiled tables exist for both density and static permittivity measurements though there are large variances in reported values [5].
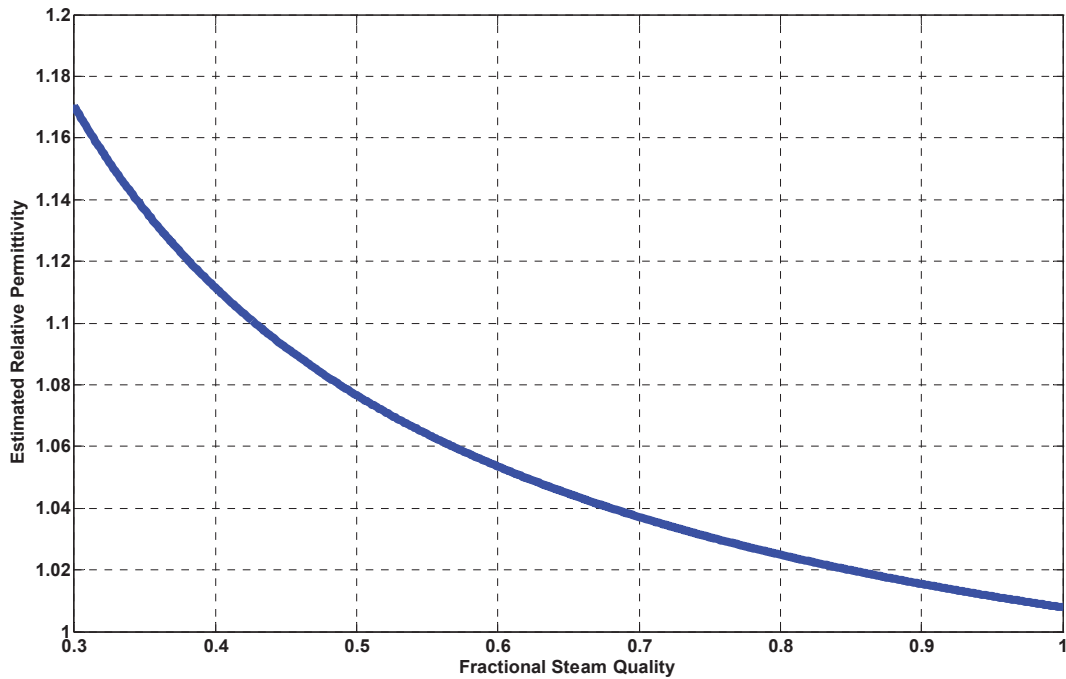
Fig. 3: Steam Quality vs Permittivity at 340°F / 150psi

The resultant permittivity shown in Fig. 3 displays the need for steam quality sensor that is extremely sensitive to small permittivity changes. Microwave resonators are high frequency structures which have electromagnetic resonance dependent upon the permittivity and permeability of the material contained in and around the geometry of the structure. The geometry of microwave resonators determines the configuration of the electromagnetic fields propagating around and through the structure .The careful selection of resonator geometry can result in very dramatic resonant frequency shifts by small variations in either the permittivity or permeability of dielectric material surrounding the resonant structure. By designing a microwave resonator highly sensitive to permittivity variations, the sensitivity requirements for the device measuring the frequency shifts is reduced while maintaining a high overall sensitivity.

CHAPTER TWO

Proof of Concept

2.1 Conceptual Design

The first step in realizing a microwave steam quality sensor was to establish its

necessary specifications for the intended application. This step proved more challenging than

anticipated as early information was sparse concerning the technical details of steam systems.

The design requirements for the steam quality sensor (SQS) were chosen based on our

understanding of the problem of steam quality measurement in an industrial environment.

The following requirements were then set for the SQS: must be capable of inline

measurement, must minimally impact steam flow, must minimally impact the existing steam

loop, must be capable of measuring relative permittivity values between 1.0078 (100% SQ)

and 1.17 (30% SQ), and should be able to measure permittivity values such that a 1% steam

quality accuracy is obtained.

The fundamental concept of the design was the use of a microwave resonant structure

to allow an accurate in-line measurement of the permittivity of saturated steam while

flowing. The requirements above were developed in collaboration with the industrial

measurement experience of Dr. Randall Jean and the thermodynamic insight of Dr. Stephen

McClain. The exact properties of the saturated steam that the sensor would encounter:

pressures, temperatures, and flow rates are highly dependent on specific steam processes.

Therefore, design parameters were selected as further insight was gained into end-

applications of the sensor with the progression of research done during the course of the design.

Product marketability of a sensor system that was minimally intrusive and requiring little steam loop modifications that could be easily integrated into existing steam systems was the initial project target. Many current steam loops use an orifice plate based differential pressure meter to measure steam flow. Substituting the OP with a structure that could serve as a flow constrictor while providing SQ measurement was a highly marketability combination.

Replacing the orifice plate with a microwave resonator requires a method of coupling energy to the resonator and a system that measures the electromagnetic resonance of the structure. The SQS excitation structure was designed to be installed on the upstream side of the OP leaving the remainder of the steam system unchanged, while gauging steam quality and flow rate at the same point in the steam loop. The signal source and receiver chosen for the experiments reported is a pulsed dispersion network analyzer (PDNA) system developed by Brandon Herrera [6]. The excitation structure therefore had to be a two port system as the PDNA is only capable of a transmission measurement, commonly referred to as S_{21}, which references a two port system or network.

2.2 Proof of Concept Design

2.2.1 Complementary Split-Ring Resonator

In 2006, Bonache et al. published a paper on a very interesting resonant structure that produced multiple resonances and was electrically small compared to the resonant frequencies produced [7]. It is known as a complementary split-ring resonator (CSRR) and is

the dual to the more commonly used split-ring resonator (SRR) often employed as a left hand filter in RF applications. Commonly used on printed circuit boards as filters for micro strip transmission line, the high Q of the resonances are very dependent on the permittivity of the substrate of the circuit board for the CSRR case. The planar metallic subtraction method of constructing CSRRs provides a simple construction method. The gaps in the rings of the CSRR are analogized to the bore hole opening found in the orifice plates. Orienting a substrate-free CSRR perpendicular to the flow of saturated steam permits the steam to flow through the gaps of the CSRR. The permittivity of the saturated steam thereby influences the resonance of the CSRR and will change with changing steam qualities.

Another advantage of CSRRs is the resonant frequency that is produced is typically much lower than similarly sized resonant structures. Having the resonant frequency of the CSRR fall within a bandwidth below the cutoff frequency of the process pipe, ensures measurement of the resonance is not affected by steam loop structures up or down stream from the sensor. The process pipe can be thought of as a circular waveguide when composed of metal. Electromagnetic waves are incapable of propagation down a waveguide below the waveguide's cutoff frequency. The cutoff frequency of a circular waveguide mode is given in (5) from Pozar [8, pp. 117-126]. The first waveguide mode to propagate in a circular waveguide is the mode with the first root if the derivative of the Bessel function $J_n(k)$, thus the mode to propagate is the TE_{11} mode with a zero of 1.841.

$$f_{c_{nm}} = \frac{p'_{nm}}{2\pi a\sqrt{\mu\varepsilon}} \tag{5}$$

From (5) it can be seen that the cutoff frequency of a round pipe behaving as a circular waveguide is dependent upon the material filling the pipe, ε and μ and the pipe radius, a. For a 4-inch ID steel pipe, the cutoff frequency of the TE_{11} mode is listed in Table

9

1 as a function of steam quality with air added for comparison. The use of circular rings with large radii, allows each ring of the CSRR to have maximal circumference, which ultimately translates to a minimal resonant frequency.

Table 1: Cutoff Frequency of 4-inch ID Conducting Pipe vs Steam Quality

Steam Quality	Cutoff Frequency
10%	1.3289 GHz
20%	1.5112 GHz
30%	1.5869 GHz
40%	1.6284 GHz
50%	1.6545 GHz
60%	1.6725 GHz
70%	1.6857 GHz
80%	1.6957 GHz
90%	1.7036 GHz
100%	1.7100 GHz
AIR	1.7167 GHz
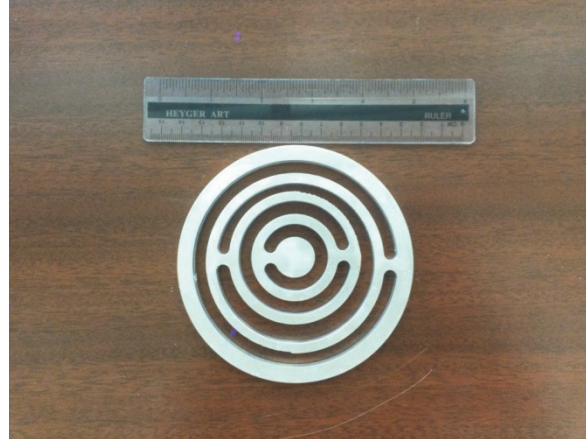
Fig. 4. Proof of concept CSRR

The initial design of the proof of concept (POC) CSRR was provided by Dr. Stephen McClain from the Baylor Mechanical Engineering Department. The CSRR was constructed from 6.35mm (¼") thick aluminum (AL) 6061 by Ashley Orr in the Baylor Machine Lab. The CSRR was milled beginning with the outer most ring. During the milling process the

aluminum temperature increased, and as the inner rings were milled rotation of the drill bit caused the CSRR to distort giving rise to the visible spacer offsets and poor tolerances on the annular gap thicknesses. The CSRR was dimensioned to fit snuggly within a schedule-40 4-inch diameter polyvinyl chloride (PVC) pipe coupler, which has actual an internal diameter of 114.3mm. The ring dimensions of the POC CSRR are shown in Fig. 5.
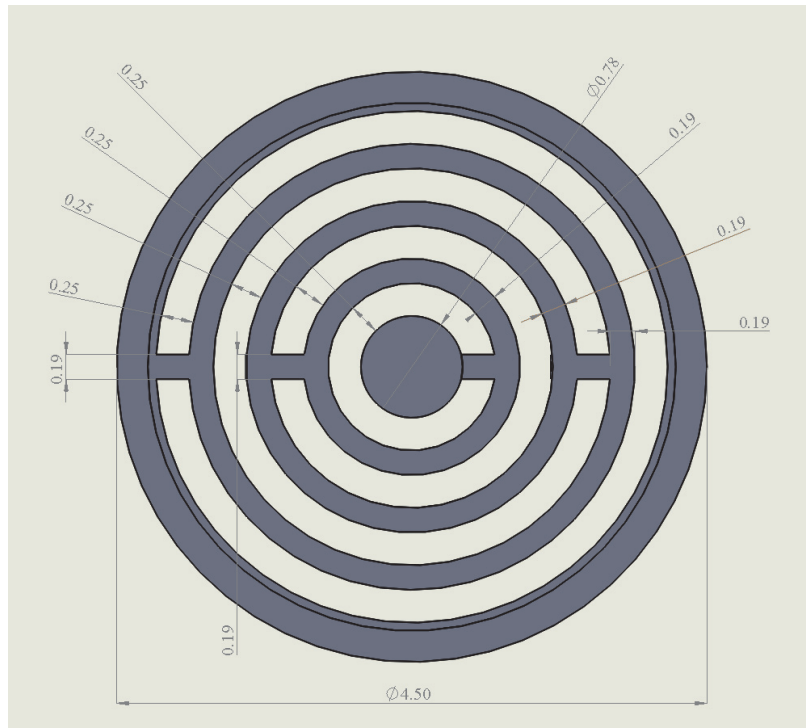
Fig. 5. CSRR dimensions (Inches)

2.2.1 Proof of Concept Excitation Structure

Development of a structure that could couple electromagnetic energy into the CSRR while it was mounted in the PVC pipe coupler was identified. The selected solution was to use a 3.175mm (1/8") steel rod soldered between two panel mount type N connectors each affixed to the PVC coupler with two 4-40 thread, 25.4mm length pan-head nylon machine

screws with 4-40 thread nylon hex nuts on the pipe inside to secure it. The rod was mounted

so that its height above the CSRR was approximately 5mm. The chosen rod height produces

a characteristic impedance, Z_0, of the path across the plate as 126Ω. The type-N connectors

each were grounded to the CSRR using a single 25.4mm 4-40 thread 316 stainless steel (SS)

machine screw. The machine screws threaded into holes drilled in the CSRR. The POC type-

N connectors had type-N to SMA adapters install so a vector network analyzer (VNA) could

be connected. The SS grounding screws connecting the coaxial cable ground to the CSRR

protruded about 2.5mm into the outer most ring. Nylon machine screws were used for the

non-grounded mounting above the CSRR to prevent electromagnetic interference effects

from free floating conductors close to the CSRR. The 2nd outermost ring was distorted due to

manufacturing causing one side to collapse to an annular gap of 4.1mm and the other to

expand to 8.6mm.

Fig. 6: POC SQS Side and Top View

2.3 Proof of Concept Testing

Testing of the POC sensor was accomplished using a modified centrifugal fan

apparatus that had been developed by Baylor Electromechanical Systems [9]. The

apparatus's original purpose was to test performance curves for different fan blades to verify manufacturer supplied data. It was then decommissioned and put in storage. In its original state the test stand was comprised of: a centrifugal fan, a fan controller, 4-inch clear acrylic tubing, an orifice plate holder with interchangeable orifice plates, differential pressure sensors, a flow dampener, manometers, and interfacing electronics. The test stand was found to be fully functional with the exception of the interfacing electronics and damping mechanism, thus no repairs were needed before conversion to an air/water test stand. A Dwyer RMC adjustable flow meter was added and attached to the laboratory sink faucet with 3/8-inch inch plastic tubing used to transport water. The 3/8-inch water tubing was routed from the flow meter to a right angle PVC joint attached to a 9-inch PVC extender on the back of the orifice plate. The flow-damping system was no longer need so it was disassemble and removed from the apparatus. The end of the water tube was inserted approximately 50-100mm into the flow, downward facing the ground. When the centrifugal fan rotation was higher than 2000RPM, the water stream became adequately disbursed in the flow by the flow turbulences caused by the 90^0 bend. At lower fan speeds or at a water flow rate higher than 7.57 L/min, the water maintained a more central distribution in the pipe.

The distribution of water in the pipe is important because the process steam is anticipated to be distributed radially about the pipe so that the test stand should reproduce expected behavior. Whereas the actual distribution is unknown, it is anticipated that higher quality steam will reside in the center of the flow with the lowest quality steam at the pipe wall. The behavior of the distribution was assumed because the pipe wall will be exchanging heat with a much colder environment, removing heat from the steam, thus leading to

condensation along the wall. Secondly, the velocity of the flow will decrease at the pipe wall so that the more dense water will accumulate there.
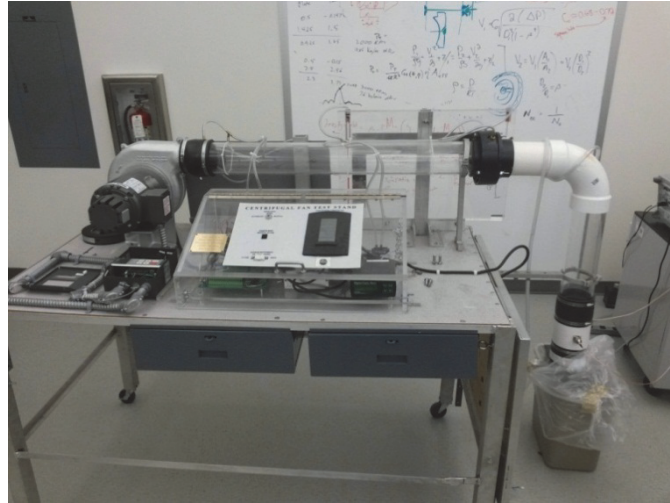
Fig. 7: Air/Water Test Stand Front View
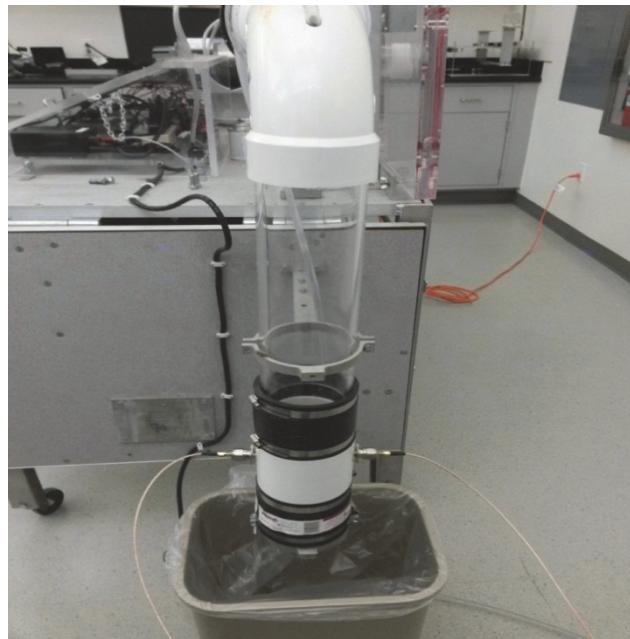
Fig. 8: Air/Water test stand side view

The fixture demonstrated the second prediction as much of the water flowed along the surface of the PVC pipe as compared to the pipe center. The observed water flow condition is

hopefully caused by a poor method of water injection, not a fundamental test flaw, and therefore can be improved with a better nozzle that can disperse the water into smaller droplets.

To include the POC steam quality sensor (SQS) in the flow loop another piece of 4-inch clear acrylic tube was cut to a length of 406mm. The tubing was then coupled to a dual notched 89mm long 4-inch PVC pipe with a 4-inch diameter black clamping rubbing coupler. The POC SQS was then installed and another 101mm long PVC spacer and clamping rubber coupler was used to rest the chain on the mount formerly holding the dampener. Water collection was achieved via a plastic bin placed beneath. The water back spray from the bin contained using a clear plastic sheet to prevent damaging measurement equipment with water spray.

The POC SQS was connected to an Agilent vector network analyzer (VNA) [10] to measure the resonance shifts as the air and water mixture was varied. The air was used as the vaporous steam model as their relative permittivities are approximately the same; tap water was used to model the liquid phase. The fan speed was then set at 3500 revolutions per minute (RPM) and the water flow rate was varied in steps of 0.1 gallons per minute (GPM) from 0.4 to 1.5 GPM. The water flow rate was not accurately measurable at 1.3 GPM as the flow meter was there was instability in the flow control of the meter. The S_{21} measurement was then taken using 1s averaging on the VNA with a range from 300 kHz to 3 GHz using an FFT size of 1601 frequency points. The magnitude response of the transmission coefficient from the test is shown in Fig. 9. The linear relationship between null frequency and water flow rate with a best fit linear approximation is shown in Fig. 10, Fig. 11, and Fig. 12.
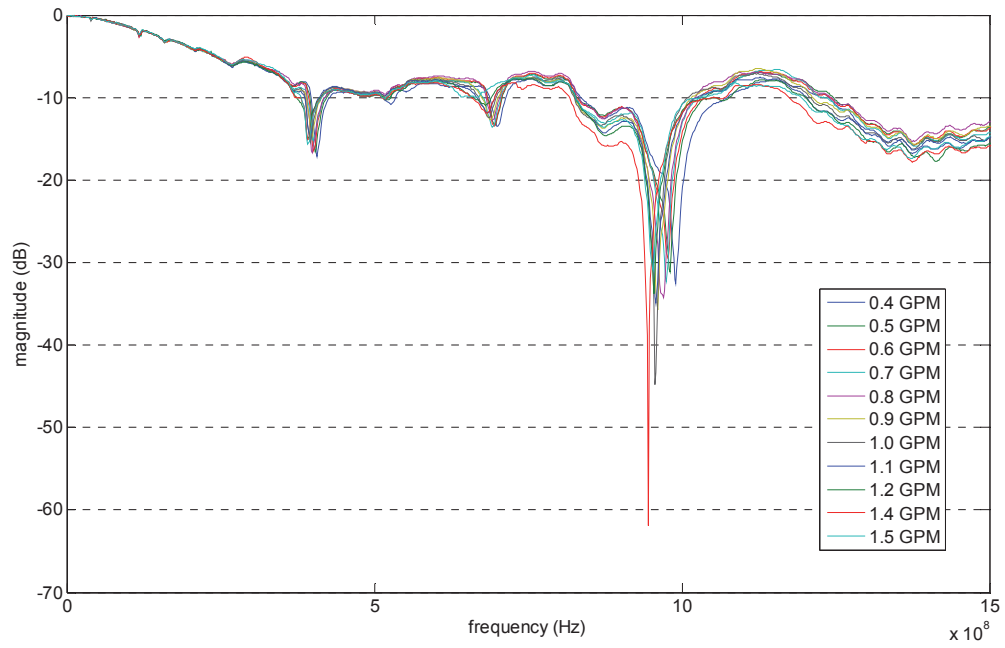
Fig. 9: Transmission measurement of the POC SQS
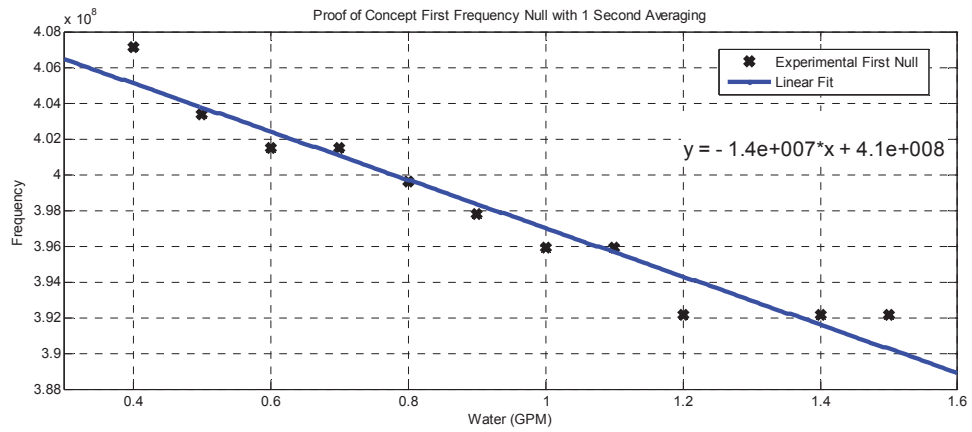
Fig. 10: POC First Null Frequency Tracking

16
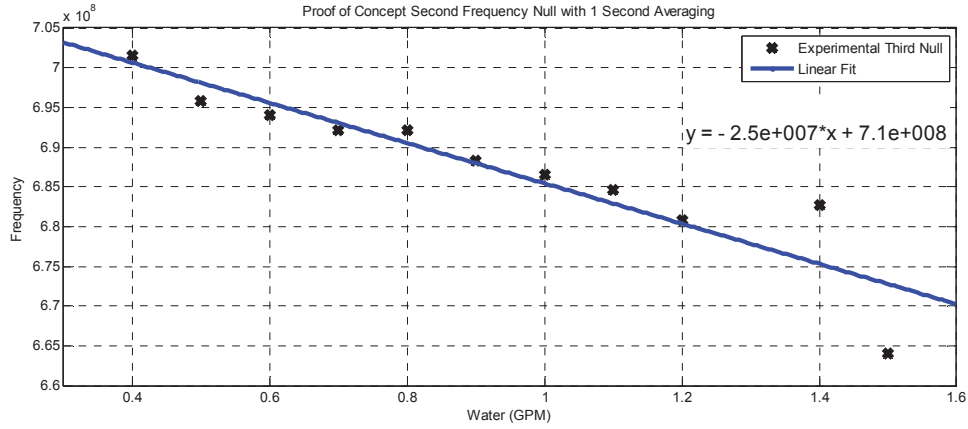
Fig. 11: POC Second Null Frequency Tracking
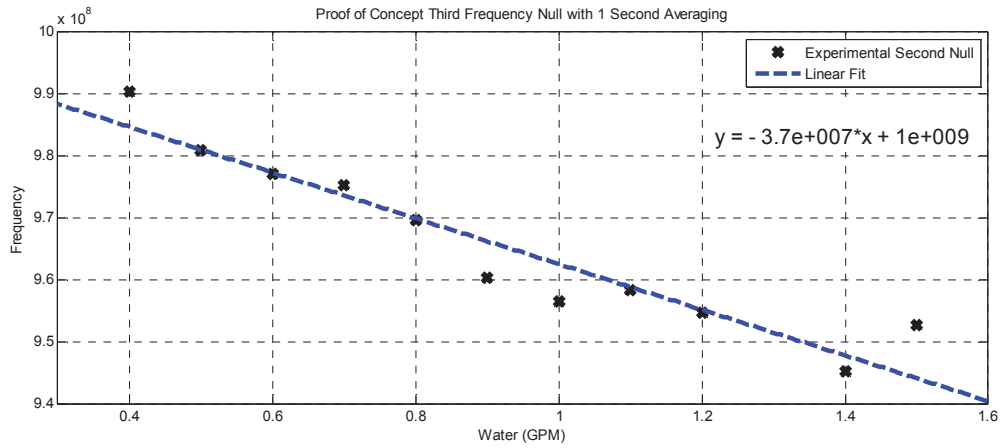
Fig. 12: POC Third Null Frequency Tracking

2.4 Conclusions

The tests showed conclusively that the prototype CSRR assembly could be excited

and observed to produce a measurable shift in the resonant frequencies of the different CSRR

rings. For these data, it was assumed that the air used had 0% humidity, velocity under Mach

0.4, and was fully constrained by the piping system so that there was no air loss through

cracks or gaps. These assumptions are important since the low velocity of the flow means

that it can be treated as incompressible and the incompressible Bernoulli equation for finding

17

mass flow rate is applicable. The test stand laboratory manual provided calibrated

volumetric flow rates for several of the different orifice plates available for use. The orifice

plate used in the POC SQS test was the 3.019" bore, 4.026" pipe inner diameter (ID). At

3500 RPM, the orifice plate pressure differential reading was 0.9167kpa (3.68 inH$_2$O). The

pressure reading across the orifice plate corresponds to a volumetric flow rate of

approximately 7.645 kL/min (270 ft^3/min) [9, p. 14]. The calculated mass flow rate of dry air

at 0.1534 kg/s using a dry air density is 1.204 kg/m^3.

Table 2: Frequency Null R^2 Values

Null Position	R^2 Value
1st	0.9386
2nd	0.8484
3rd	0.9034

It is evident that the concept of using a multi-resonant structure like a CSRR has

merit for use in steam quality sensing. The relationship between frequency nulls and water

flow rate have very good correlation based upon calculated coefficient of determination (R^2)

values in Table 2. Table 3 shows the test results in terms of the mass fraction of the air over

the combined air and water mass flow rates. The first column shows the volumetric flow

rates of water used during the test with the equivalent mass flow rate of the water at 25^{0}C

shown in the second column. For a fixed volume within the pipe, the application of the

volumetric mixing equation with air and water as components gives a vapor quality per

second value. If the flow rates are allowed to be constant for a sufficient duration the

equivalent vapor or modeled steam quality can be assumed to be time invariant and the vapor quality within the fixed volume is also considered to be constant. This vapor quality is expressed as the mass ratio of air to the combined mass of the air and water flow rates and is shown in column three of Table 3.

Table 3: POC SQS modeled Vapor Quality using an Air Flow Rate of 0.1534 kg/s

Water Volumetric Flow Rate	Water Mass Flow Rate	Vapor Quality
0.4 gal/min	0.0252 kg/s	85.9 %
0.5 gal/min	0.0315 kg/s	83.0 %
0.6 gal/min	0.0378 kg/s	80.2 %
0.7 gal/min	0.0441 kg/s	77.7 %
0.8 gal/min	0.0504 kg/s	75.3 %
0.9 gal/min	0.0567 kg/s	73.0 %
1.0 gal/min	0.0630 kg/s	70.9 %
1.1 gal/min	0.0693 kg/s	68.9 %
1.2 gal/min	0.0756 kg/s	67.0 %
1.4 gal/min	0.0882 kg/s	63.5 %
1.5 gal/min	0.0945 kg/s	61.9 %

CHAPTER THREE

Transverse Electromagnetic Mode Wire Excitation

The first phase of the development of the SQS was the construction of a computer

model that would emulate the electromagnetic behavior of the sensor geometry interacting

with steam. The emulation was accomplished using CST Microwave Studio (CST MWS), a 3

dimensional electromagnetic (EM) field solver [11]. The use of CST MWS allowed for low

cost behavioral testing of various sensor designs and provided results more rapidly than a

build and measure approach. Chapter 3 reviews some of the simulations performed using a

transverse electromagnetic (TEM) mode excitation structure to provide better insight into the

behavior of steam in the presence of a CSRR excited using a broadband signal.

 Each of the following simulations provides insight into the sensor behavior and the

progression of decision making that occurred during SQS development. The model designs

in chapter 3 used the same four-ring orifice plate structure used in the POC model described

in chapter 2. The frequency response of four-ring orifice plate was sensitive enough to the

permittivity of the air-water so that shifts in the S21 frequency nulls could be discerned. Thus

design time was devoted to improving the coupling structure and understanding its behavior

instead of redesigning the geometry of the rings.

3.1 Semi-Circular Rod

The research shifted to developing better sensor geometry to maximize coupling

between the CSRR and the transmission line to and from the VNA. The impedance mismatch

between the 50Ω Z_0 SMA cable and the much higher POC transmission line impedance

needed improvement. The goal was to have a Z_0 close to 50 Ω to achieve minimal wave reflections at the transition from SMA coax to the transmission line inside the pipe, referred to as the coupling transmission line section here forth.

The orifice plate can be envisioned in terms of a microstrip transmission line where the ground plane is interrupted by a CSRR that filters the transmitted signal. CSRR behavior is commonly described in literature through use of microstrip filters where the CSRR is etched beneath the microstrip line in the ground layer beneath with a layer of dielectric material between [12]. A CST model was developed replacing the circular cross-section rod with a semi-circular rod making its cross-section a half-circle. The half-circle rod was kept at same height above the CSRR plane as the POC, approximately 5mm. A 6.35mm (¼") diameter rod was used as the simulation coupling section conductor. The rod was halved to acquire a half-circle cross section then attached to the SMA center conductor in the model. Rounded supports were added to back of the CSRR where the rings connect to another in order to increase the overall structure stiffness. The model is shown from different angles in Fig. 14 and Fig. 15.

The change in rod cross section was warranted because the semi-circular rod offers a lower coefficient of drag of 0.42. For comparison, the coefficient of drag of a flat rectangular plate, commonly used in microstrip excitation structures, is 1.1 [3, p. 511]. This reduction in drag coefficient in reduces the drag force upon the rod caused by fluid flow which in turn decreases the required mechanical holding strength of the rod support.

The use of a semi-circular TEM structure was done in lieu of circular rod so the TEM coupling section conductor could have more separation from the ground plane and still achieve the same impedance. For example, a 6.35mm diameter wire in air would have to be

1.2mm above a PEC plane to have a 50Ω impedance. A semi-circular wire modeled as a thick micro strip trace with a trace thickness of 1.6 mm and a trace width of 6.35mm, requires a height of 1.8mm to achieve a Z_0 of 50.6Ω. Since the semi-circular cross section is very similar to a thick microstrip trace, an approximated characteristic impedance for the semi-circular rod was done by approximating it to microstrip line with a top conductor thickness equal to a quarter of its width. The characteristic impedance of a thick microstrip trace is given below in (6) [13]. The impedance approximation results in the semi-circular rod having a Z_0 of 85.3 Ω compared to the POC's coupling section Z_0 of 126 Ω.

$$Z_0 = \frac{87.0}{(\epsilon_r + 1.41)^{1/2}} \ln\left[\frac{5.98H}{0.8W + T}\right] \tag{6}$$
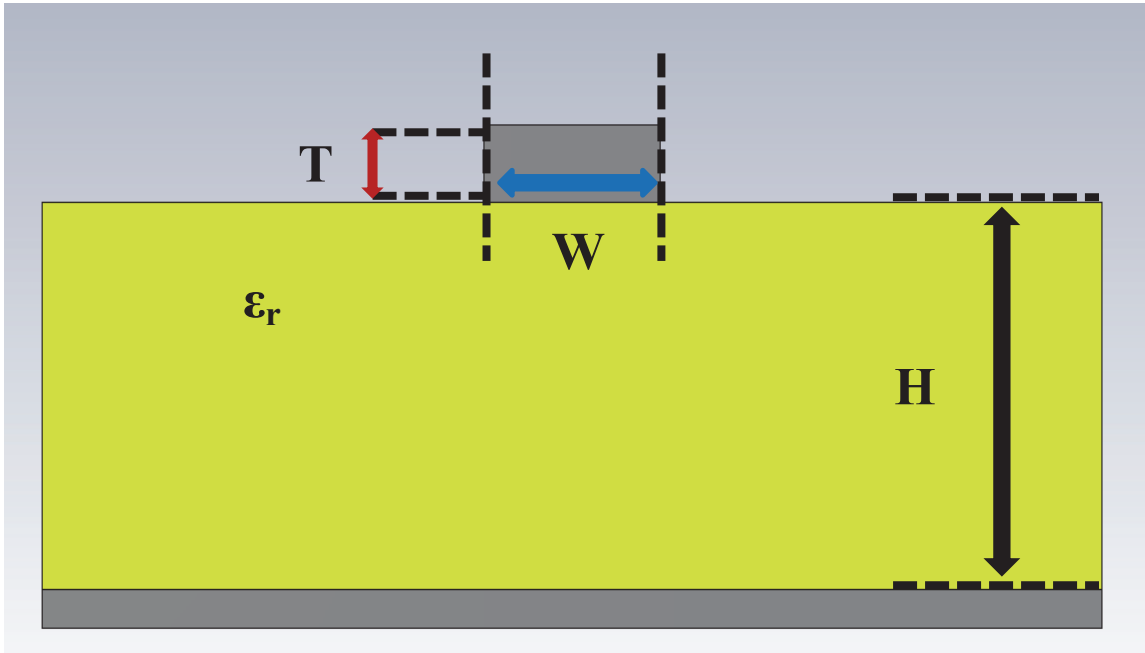
Fig. 13: Microstrip over Ground Plane Parameters
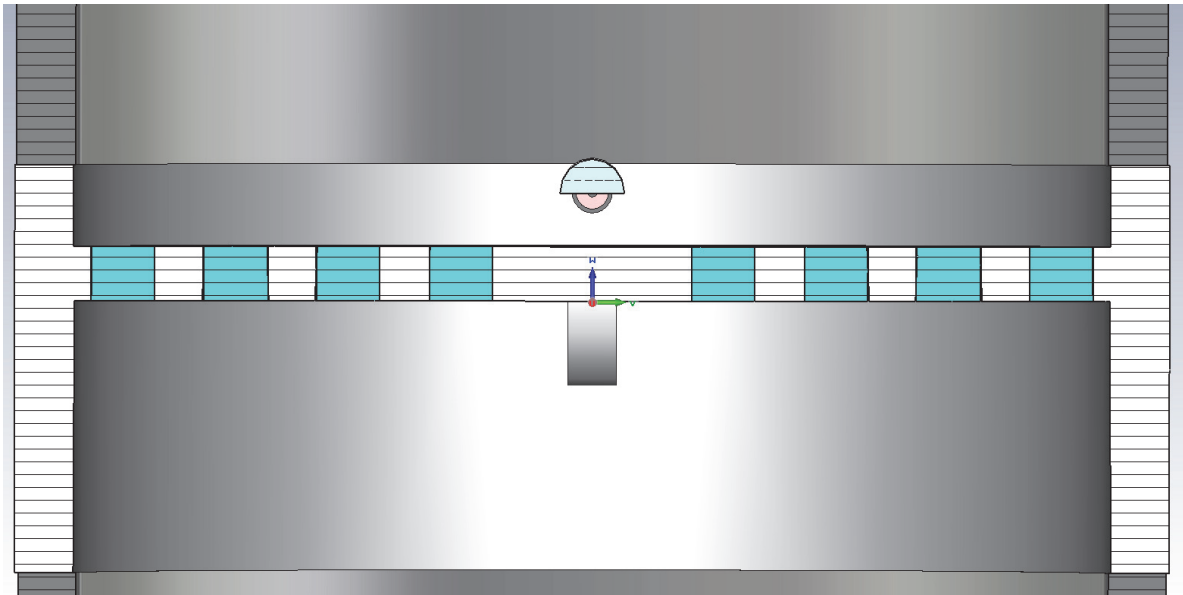
Fig. 14: Semi-circular TEM Rod Excitation Simulation
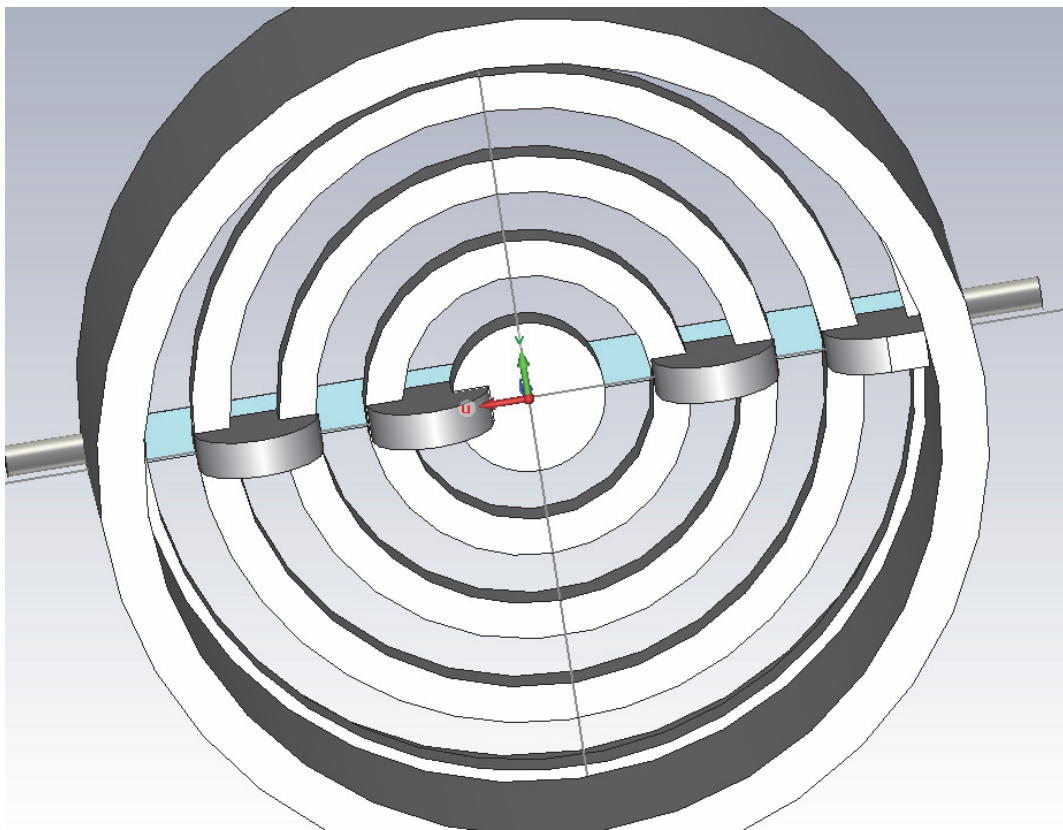
Fig. 15: CSRR Ring Extended Ring Supports
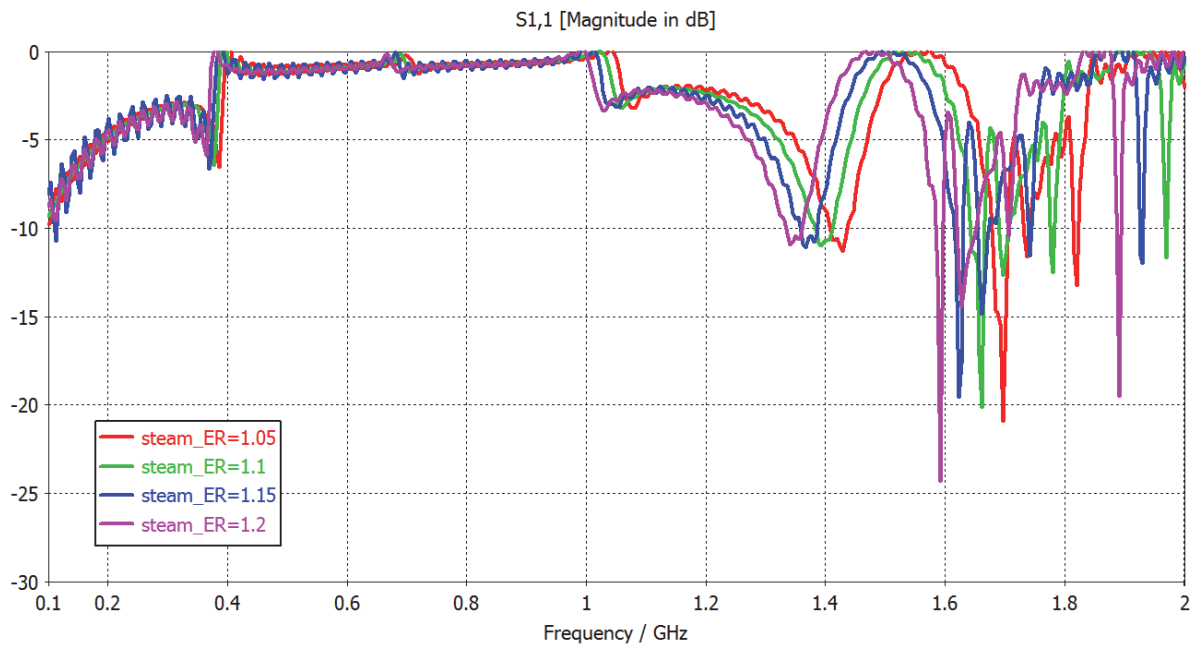
Fig. 16: |S11| Semi-Circular Rod Excitation Simulation
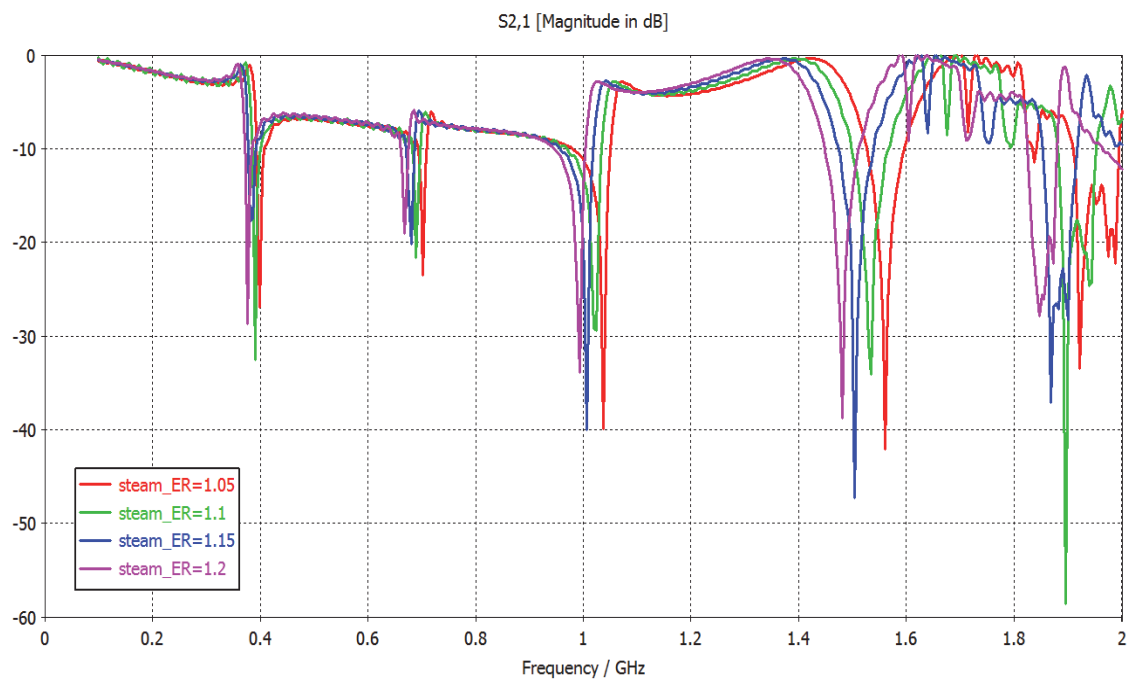
Fig. 17: |S21| Semi-Circular Rod Excitation Simulation
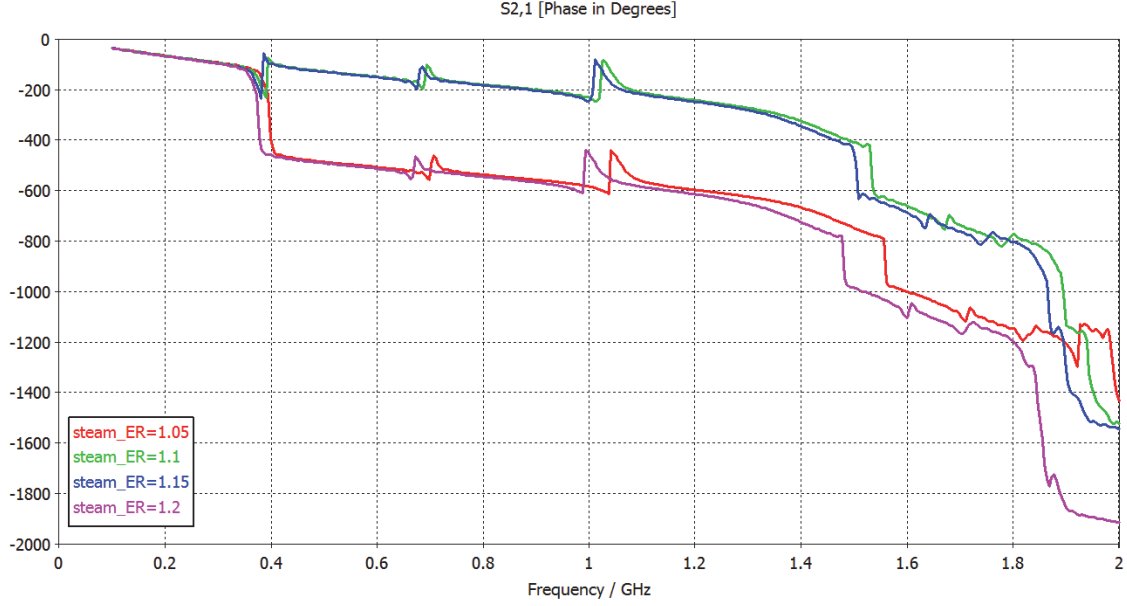
Fig. 18: Phase of S21 Semi-Circular Rod Excitation

Several important lessons were learned from the simulation. First, the rod was still poorly impedance matched, resulting in poor energy coupling into the CSRR. This is expected behavior since the reflection coefficient magnitude between the coaxial and coupling section is 0.2625. Secondly, the CSRR maintains its meta-material behavior when excited using the model structure. The first conclusion can be seen in the $|S_{11}|$ plot in Fig. 16. One observes that the magnitude rarely dips below -5dB. The high S11 does not, however, affect the performance of the system. The system performance is graded by the resonant quality of the S21 frequency stop-bands which appears as nulls in the S21 shown in Fig. 18. The strength of the perpendicular E-fields between the coupling rod and the CSRR was still sufficiently strong to excite the resonator and produce high quality nulls as seen in Fig. 17. The second conclusion arises from S21 behavior near these nulls. One can observe in Fig. 17 around 400MHz the signal peaks slightly before immediately dropping a minimum of 20dB

25

to a null. This immediate peak then null or null then peak response is not typical for ordinary resonators, but is very prevalent in SRR and CSRR and could provide an alternative [14].

The steam used in the model was uniformly distributed and homogenous throughout the entire pipe and CSRR rings. The relative permittivity of the model's saturated steam was swept between 1.05 and 1.2 in increments of 0.05; no losses were considered for the steam. The frequency shift of the nulls in the signal transmitted from port one to port two can be compared in Table 4.

Table 4: Semi-Circular Rod S21 Null Frequencies

Steam Relative Permittivity	1st Null Frequency	2nd Null Frequency	3rd Null Frequency	4th Null Frequency
1.05	399.2 MHz	702.6 MHz	1.0371GHz	1.5608 GHz
1.1	390.4 MHz	689.4 MHz	1.0221 GHz	1.5344 GHz
1.15	383.5 MHz	680.4 MHz	1.0063 GHz	1.5036 GHz
1.2	377.2 MHz	667.4 MHz	0.9930 GHz	1.4816 GHz

The semi-circular rod design focused on using a coaxial type structure in the pipe wall with the coupling rod affixed to it via a solder joint. The design utilizes fundamental and simple transitions from coaxial to wire micro strip transmission line making it well understood electrically. The design has problems at the transition from coaxial transmission line to the coupling rod. For the design, fluid flow exerts force on the rod surface matched only by the shear strength of the joint between the center coaxial conductor and rod. Thus, this style of connection is only feasible for cold, low mass flow environments, similar to the POC testing, where a low amount of force is exerted upon the coupling rod. The difference in the POC design and the semi-circular rod is the semi-circular shape of the rod allows for a lower Z_0 with increased height between the plane and conductor. The model design using

half-rod coupling structure excites the four-ring CSRR quite well. The CSRR produces also has a phase advance shown in Fig. 18 as the upward sloped notches which is behavior only observed in meta-materials indicative of backwards energy propagation. The CSRR resonances are sufficiently sensitive to frequency to make extraction of permittivity possible. A structural support to aid in mechanical strength of the CSRR ring joints follows.

3.2 CSRR Structural Support Bar

One of the problems with the POC CSRR was that the rings could withstand very little force before deflection occurred. A simple press of ones thumb could move the innermost ring a couple millimeters or more. Additional ring supports shown in the previous semi-circular model provided the CSRR rings with increased the mechanical rigidity without sacrificing their strength of resonance. While the rings in the previous simulation were supported by additional braces, it was determined that those would still be inadequate to stop ring deflection and vibration in environments harsher than the air/water test apparatus.

Theory states most of the electromagnetic fields for TEM microstrip transmission lines are contained between the top conductor and the ground beneath with small amounts of fringing fields around. Similarly, it is postulated that the electric field strength between the TEM rod and the CSRR are strong with only weak electric fields existing on the downstream side of the CSRR as seen in Fig. 19. Since most of the electromagnetic fields are contained between the coupling rod and the CSRR rings, the inclusion of a supporting bar attached some distance behind the CSRR to provide a rigid support is possible. It was postulated that such a support would only dampen or distort the resonance of the CSRR rings slightly, but the extent was unknown. A CST model was therefore created using a semi-circular TEM rod

excitation model with a 4.76 x 4 mm PEC bar located 6mm downstream of the CSRR, but

connected to its current ring brace as shown in Fig. 20.
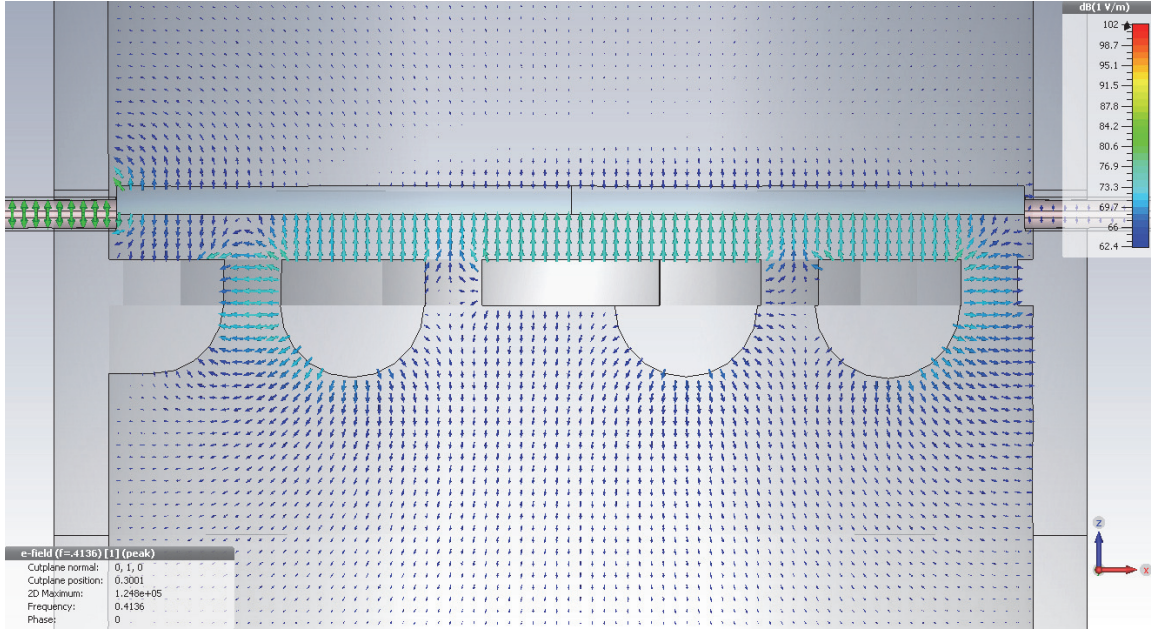
Fig. 19: Electric Field between TEM Rod and CSRR at 0.4136GHz, No Support Bar
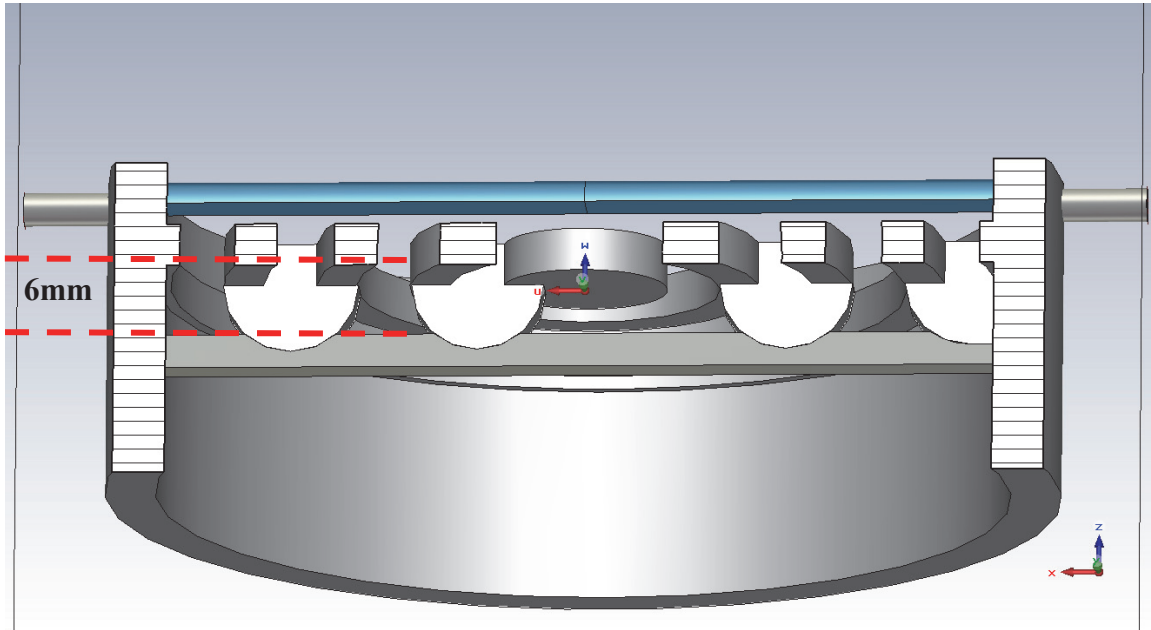
Fig. 20: Addition of CSRR Support Bar to Model

Two simulations were run, one with and one without the support bar each time sweeping the permittivity of the steam from 1 to 1.2 in steps of 0.05. Other than the support bar structure the models are identical. Adding the support bar shifted all the resonances higher with more pronounced shifts for the larger rings. This is expected as the support bar adds small amounts of capacitance to each ring by reducing the effective distance between rings. Table 5 below shows the position of the nulls beginning with the lowest frequency null for the (air) ε_r =1.00 permittivity case. Note, this simulation was not concerned with null depth thus losses in the steam were not accounted for by using conductivity model for the imaginary part of the steam permittivity.

Table 5: |S21| Null Frequency Comparison for ε_r =1.00

Null Number	Null Frequency No Support Bar	Null Frequency With Support Bar
1	0.4136 GHz	0.9281 GHz
2	0.7174 GHz	1.1339 GHz
3	1.0653 GHz	1.6337 GHz
4	1.6043 GHz	(> $F_{Pipe\ Cutoff}$)

The addition of the support bar to the simulated CSRR provided better than expected results for the S21 response of the system. The comparison of simulated system S21 null frequencies with and without the support bar is given in Table 5. The depth of the nulls remained approximately the same with the primary difference the upshifting of the supported structures frequency response for the first three nulls. The 4th null is not comparable between supported and unsupported CSRR models as the null had been frequency shifted past the cutoff of the pipe and thus was interfered with by wave propagation. Fig. 21 shows a comparison of the

model S21 with and without the support bar from which the above conclusions were drawn.
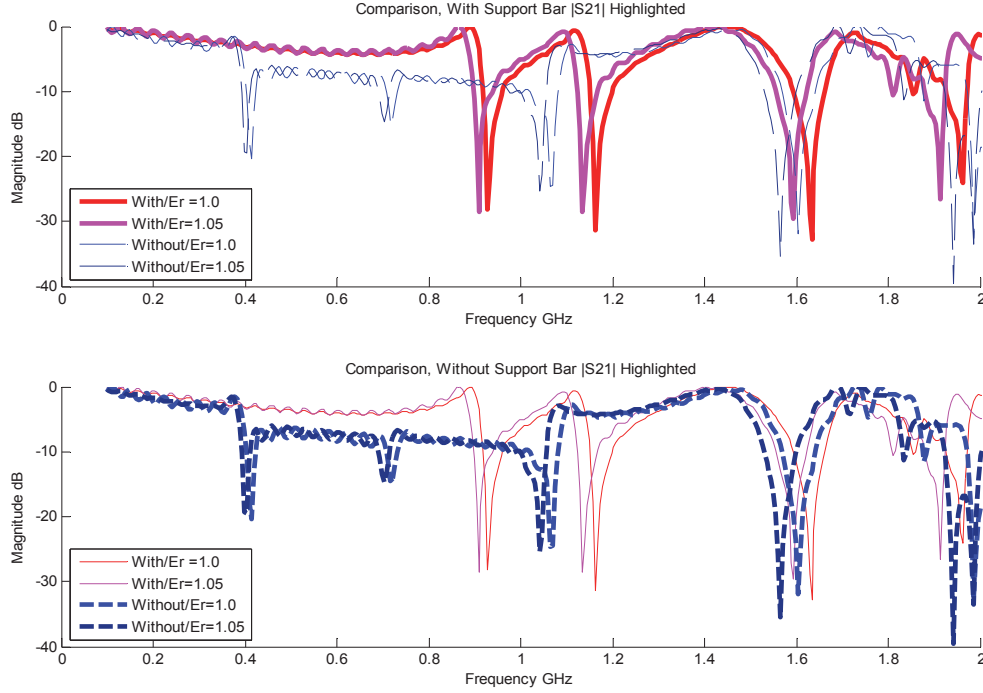
Fig. 21: |S21| Simulation Results with and without support

Fig. 22 displays the |S21| result of the support bars distance to the back of the CSRR ground plane being swept from 0mm or no separation to 7 mm away, in 1mm increments. The cyan trace in Fig. 22 is the system response with a support bar to CSRR distance of 6mm. This 6mm distance will be used in the simulations following that also include the support bar until the finalized excitation is developed. A 6 mm was an optimal design choice as it left three nulls below the cutoff frequency of the pipe, yet was not unreasonably distant from the CSRR.

The CST model was solved using time domain solver. This solver simulates a broadband time domain pulse applied at the waveguide ports of the model. The time domain solver samples at discrete time points the pulse in the structure. The energy contained in the simulation decays very slowly in the time domain, because the simulation contains a

resonator which stores a large amount of power. Because of this the default CST time domain solver step size of 30ns the simulation still has 10uW of power contained within. The simulation was rerun changing the time window step size 60ns at the expense of computation time. The values of the null depths are expected to be more accurate than previous simulations, but the resulting computational time increased taking 6 hours with GPU hardware acceleration. The simulation was still unable to resolve the energy in the simulation to the desirable level of accuracy of 1nW, because the field energy decays at an extremely slow rate. The duration of the time window step has no effect on the frequency position accuracy of the nulls and will only increase the depths of the nulls seen.
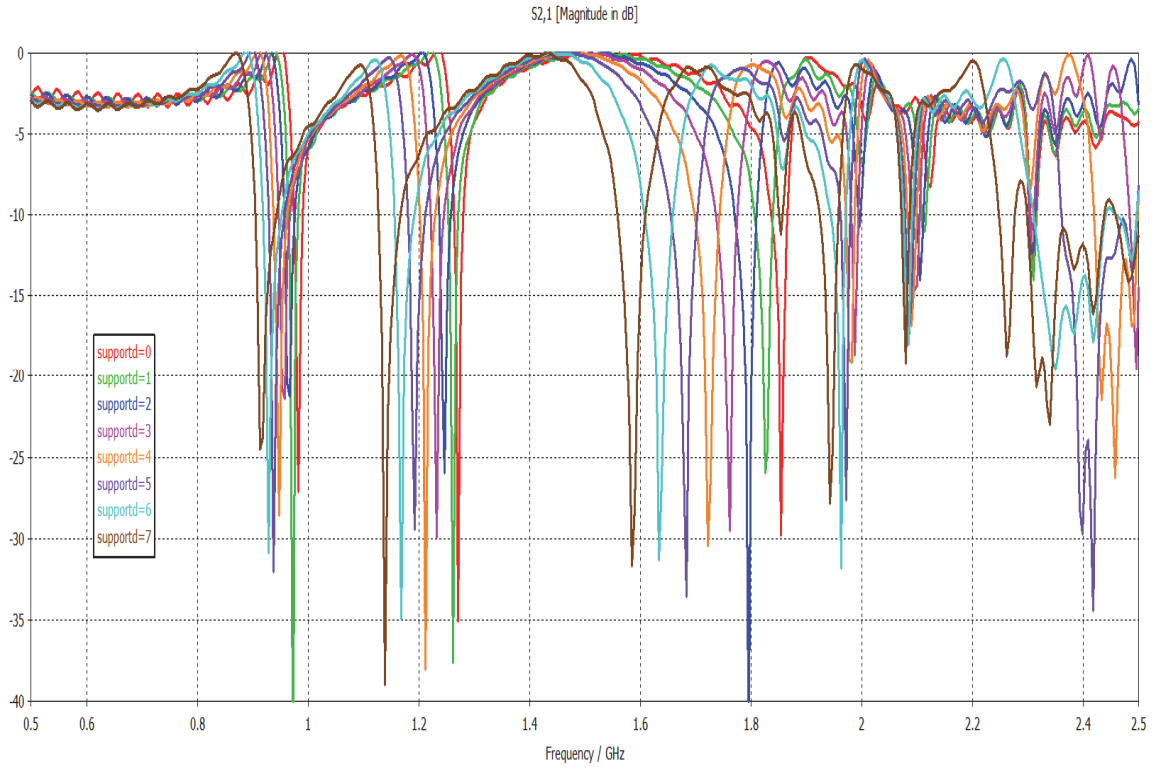
Fig. 22: Support Bar Distance from CSRR Sweep, 1mm
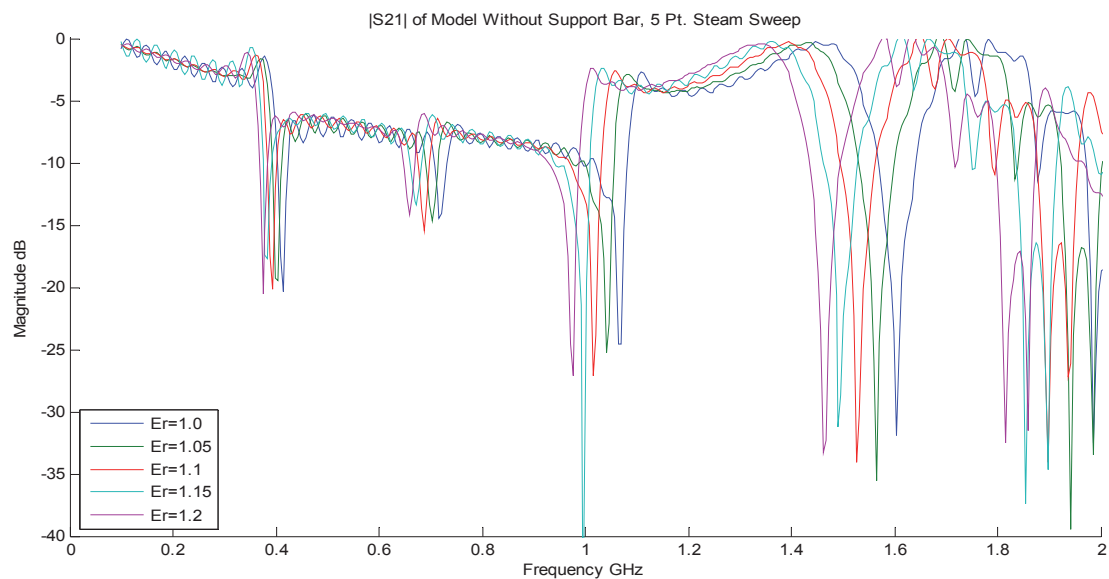
Fig. 23: |21| Simulation Full Sweep without Support Bar
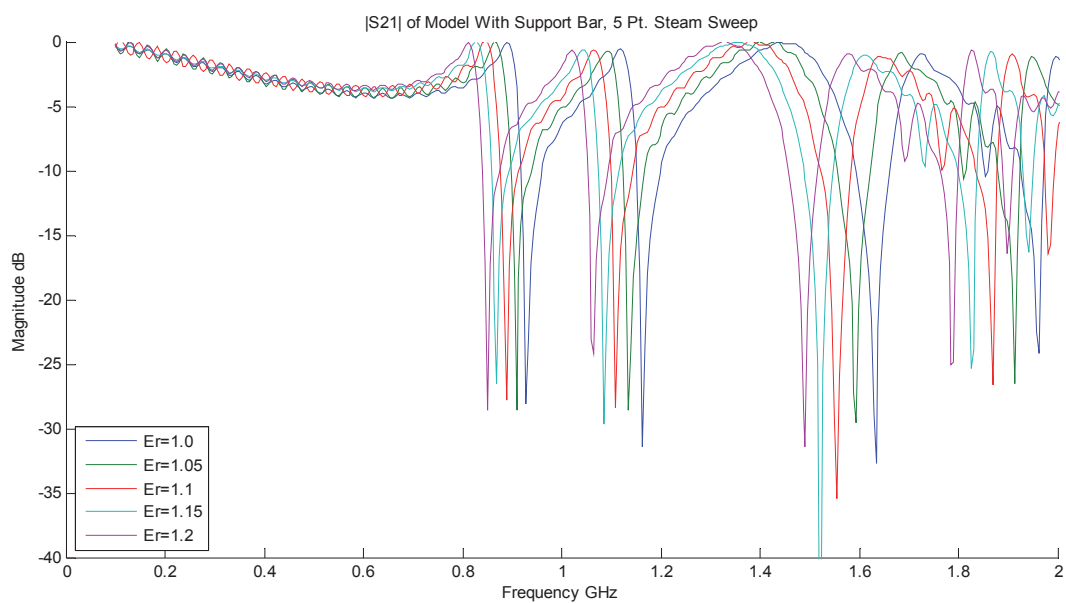
Fig. 24: |S21| Simulation Full Sweep with Support Bar

32
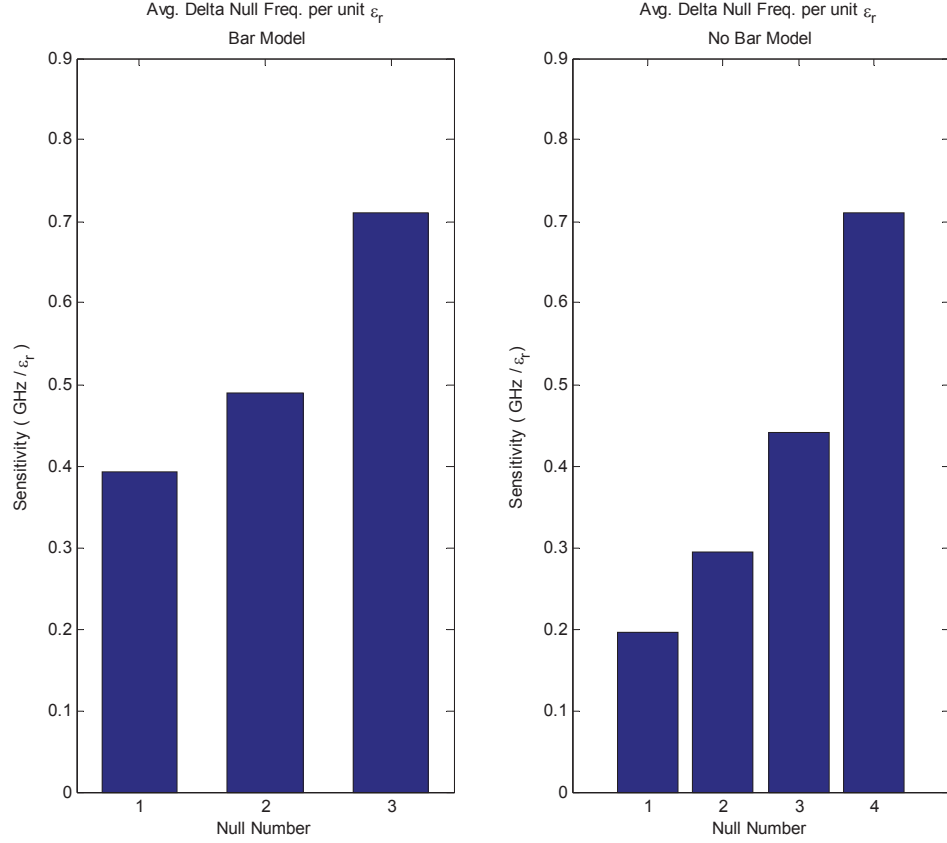
Fig. 25: Sensitivity Analysis of Bar on |S21| Nulls

The addition of the support bar had little effect on the frequency response of the CSRR to changing steam permittivity. The primary effect the support bar was to increase the frequency of the resonances, as seen in Fig. 25. The Fig. 25 shows expected frequency shift from the null's orginal frequency in a vacuum divided by the permittivity step size to provide a metric of the permittivity change sensitivity of the CSRR. The sensitivty limits in this simulation were found to be largely due to the frequency bin size of fourier transform function. The frequency resolution of the simulation was just under 3MHz over the 3GHz simulation bandwidth. A moderate simulation mesh cell count (381,738) could have slightly limited the volume of steam inside the rings also negatively affecting the simulated

sensitivity. None the less, it is still evident that the addition of downstream ring stabilizing structures to the CSRR will not impede the meaasurement of steam permittivity.

3.3 CSRR Annular Quality Determination

The distribution of steam quality and flow through a pipe is not uniform, but varies annularly as previously mentioned. The steam quality is instead anticipated to vary radially from the central axis of the pipe with the lowest steam quality along the pipe wall. The geometry of the CSRR was previously shown to be advantageous in that the gaps between rings do not necessitate the same permittivity to be in each gap for the CSRR to resonate. It was postulated that the permittivity of each gap could be extracted by observing the frequency response of the nulls and correlating a shift in the frequency of a null from its resonance in free space to the permittivity contain with in that gap. A four-ring CSRR would theoretically allow for a measurement of four different steam permittivity values by observing the resonant of each of the 4 nulls.

Thus, the number of frequency nulls produced by an unsupported CSRR should be equal to the number of CSRR rings it contains. Unknown was the dependence of each ring resonance to the material of the other rings. The model developed in this section investigates whether each ring possesses an independent resonance or if dependent upon the dielectric in the neighboring gaps the degree of dependence.

 The model was created with steam rings in the CSRR that whose permittivities could be varied independently of the others and from the steam contained in the pipe. The CSRR and steam rings were simulated in CST using a wire over ground plane excitation technique. The rings were ordered as shown in Fig. 26.The simulation was performed using a model similar to the one the support bar from the previous section. The support bar was once again

34

placed at 6mm behind the CSRR but was modeled with steel-1010 to better approximate losses in the CSRR rings. The same model was then modified by removing the support bar to see an unsupported CSRR's behavior and simulated. As the depth of the nulls was currently of interest, no conductive loss was added to the steam nor was the time window size larger than the default value of 30ns.
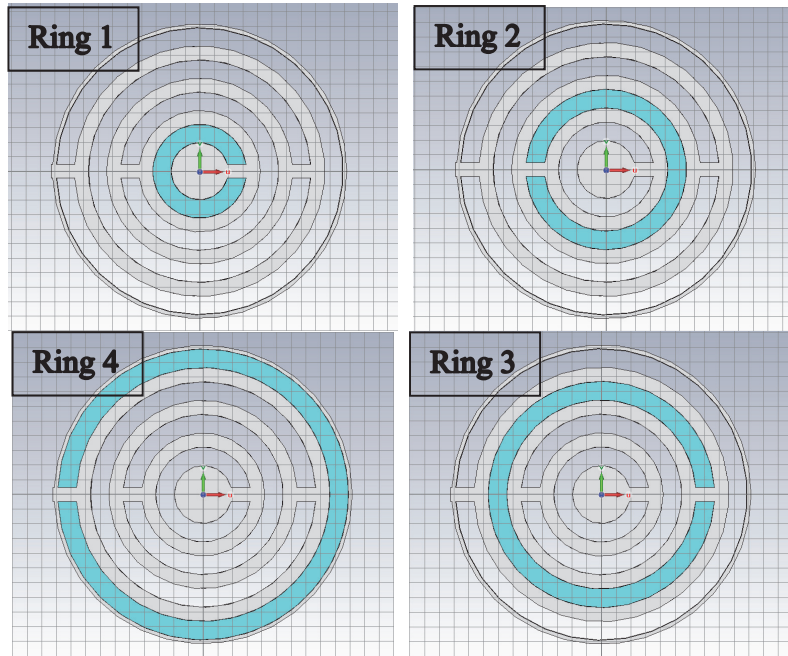
Fig. 26: Steam Ring Numbering

Both models were simulated with a smaller fast Fourier transform bin size than the previous simulations as precisely determining the position of frequency nulls and small shifts required additional frequency accuracy. The number of bins was raised to 3801 to give a 500 kHz frequency resolution in the range from 0.1 GHz to 2.0 GHz. The relative permittivity swept in the rings also changed from 1.0-1.1 to 1.00785-1.17, the anticipated values for 100% and 30% quality steam, respectively, at 175^0C and 1.03Mpa. The simulation mesh cell

size used for the gaps between rings of the CSRR was made finer to reduce the discretization effects of the Cartesian coordinates system mapping cylindrical geometry.

An observation had made in a previous simulation that mesh cell size inside the rings may affect frequency position of the nulls by overly discretizing the circle rings. Thus, the size of the hexahedral mesh used in the rings was 0.7mm in the Z or vertical direction, 1.5mm in the x or left right axis and 1.4mm in the up down axis when observing Fig. 26. This increased the total model mesh cell count to 940,752 which greatly increased simulation time. The distance between the rod and the CSRR was also decreased to 1.8mm which results in an approximate characteristic impedance of 50 Ω in order to minimize reflections at the boundary of the coupling section to the coaxial lines. The following figures show the frequency response of the bar and unbarred model as the permittivity of rings were varied individually.
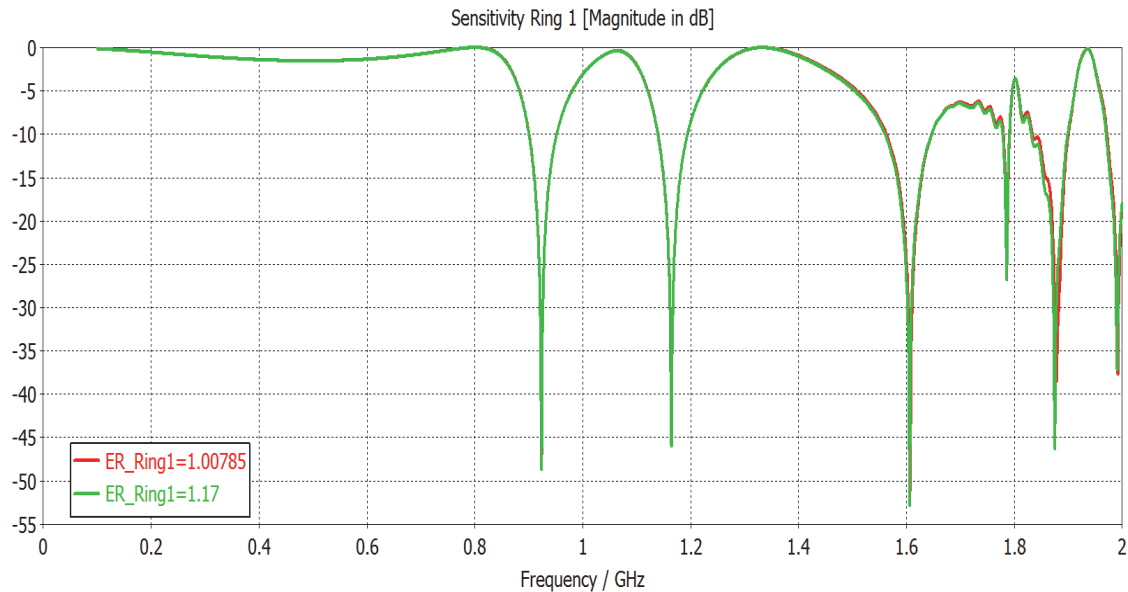
Fig. 27: |S21| Permittivity Sweep Ring 1, Model with Bar
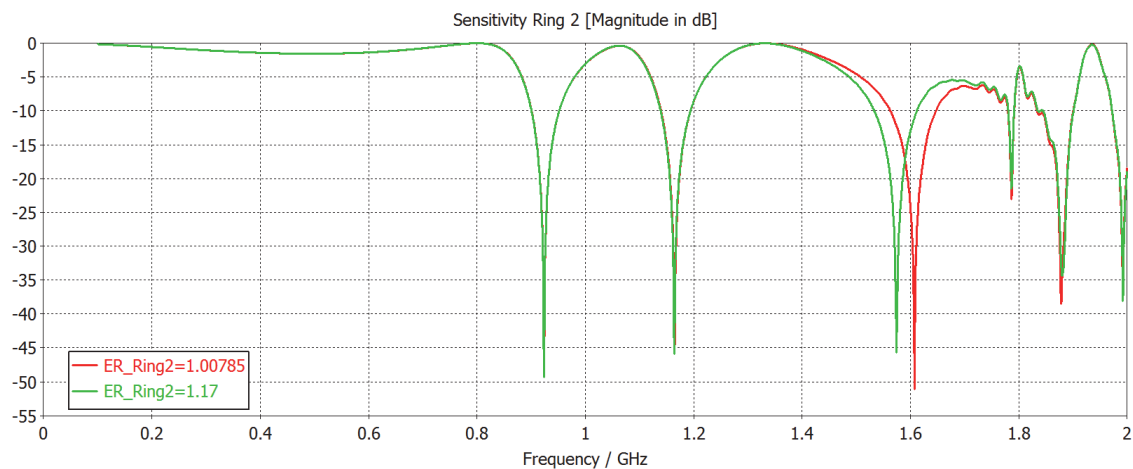
Fig. 28: |S21| Permittivity Sweep Ring 2, Model with Bar
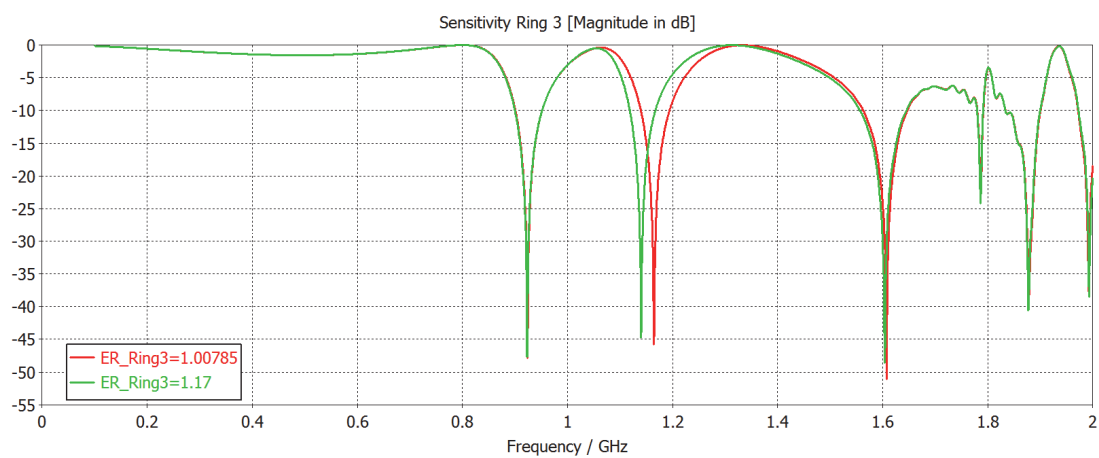
Fig. 29: |S21| Permittivity Sweep Ring 3, Model with Bar
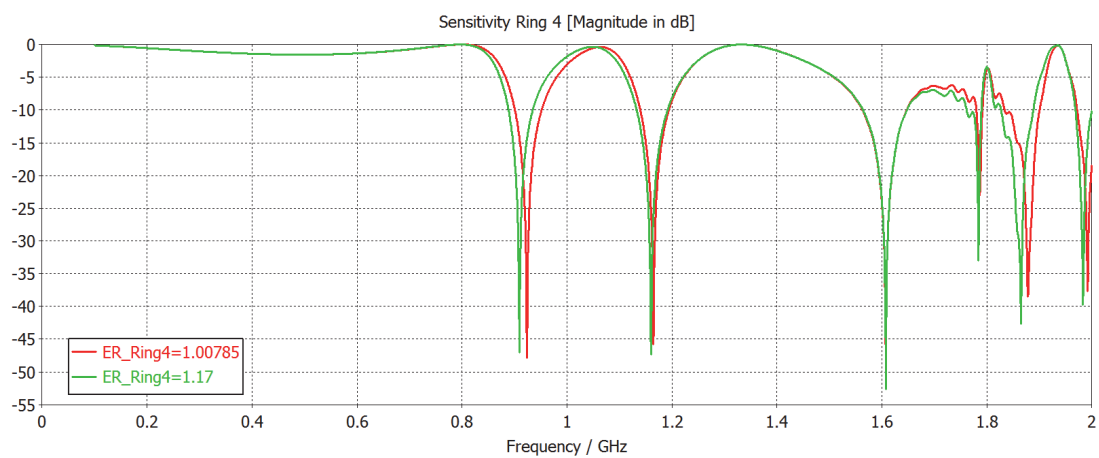
Fig. 30: |S21| Permittivity Sweep Ring 4, Model with Bar
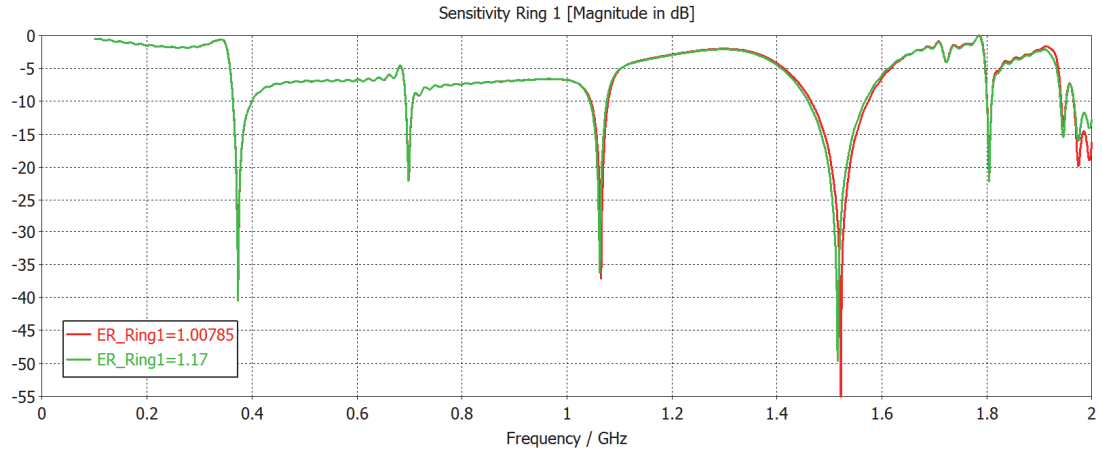
Fig. 31: |S21| Permittivity Sweep Ring 1, Model with No Bar
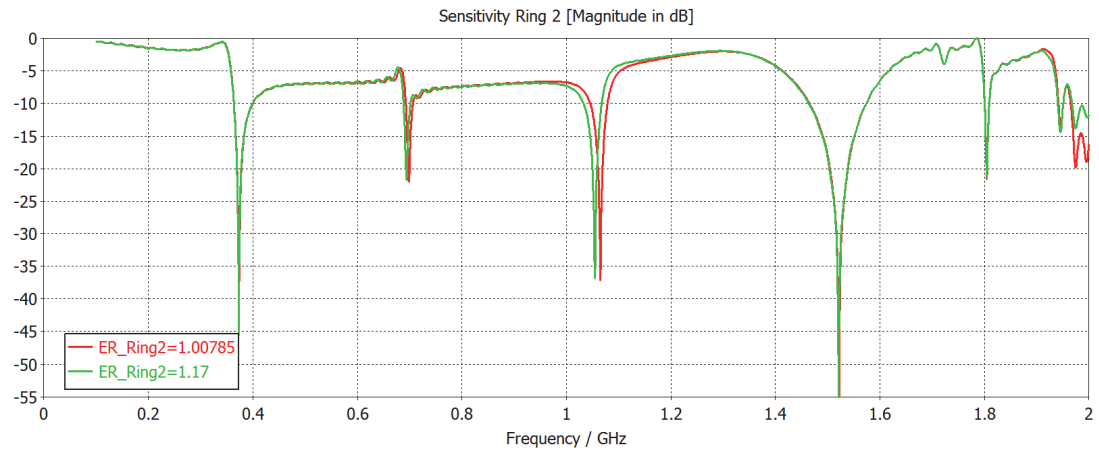
Fig. 32: |S21| Permittivity Sweep Ring 2, Model with No Bar
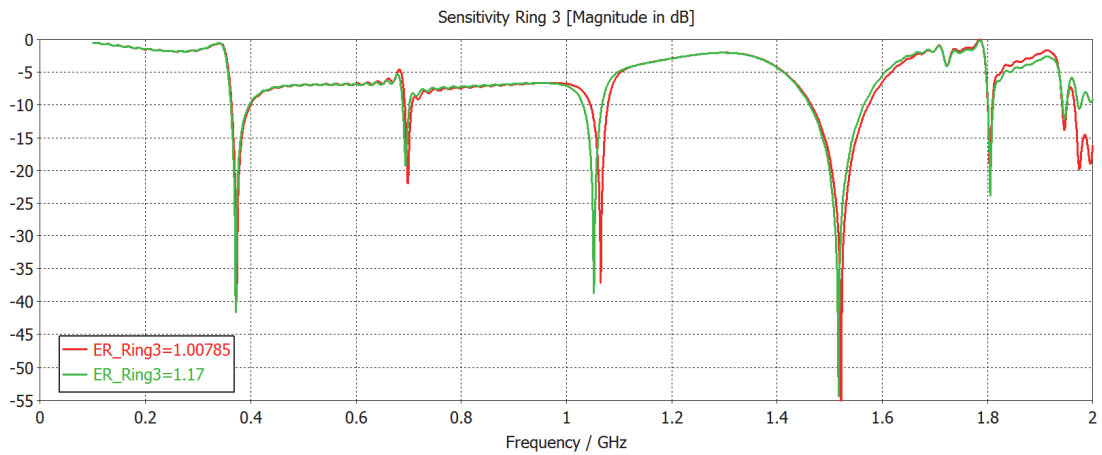
Fig. 33: |S21| Permittivity Sweep Ring 3, Model with No Bar
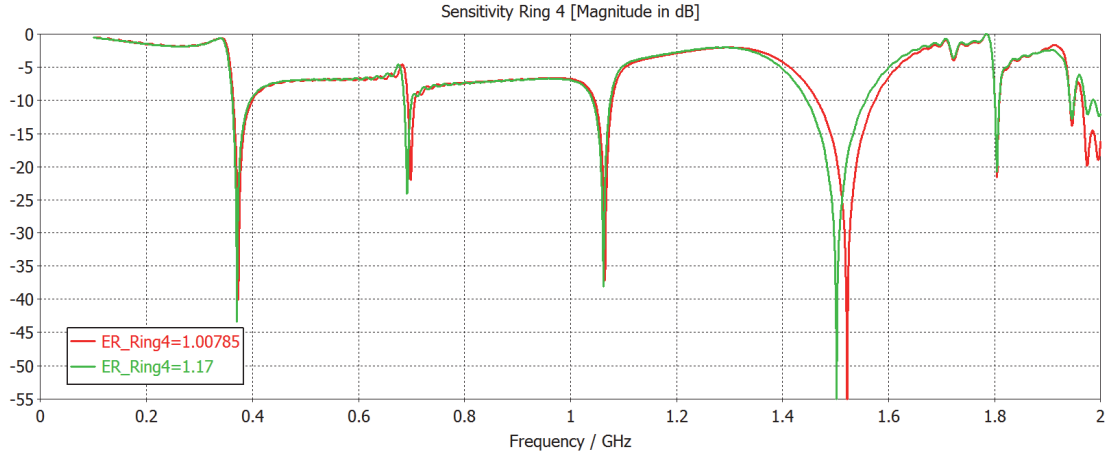
Fig. 34: |S21| Permittivity Sweep Ring 4, Model with No Bar
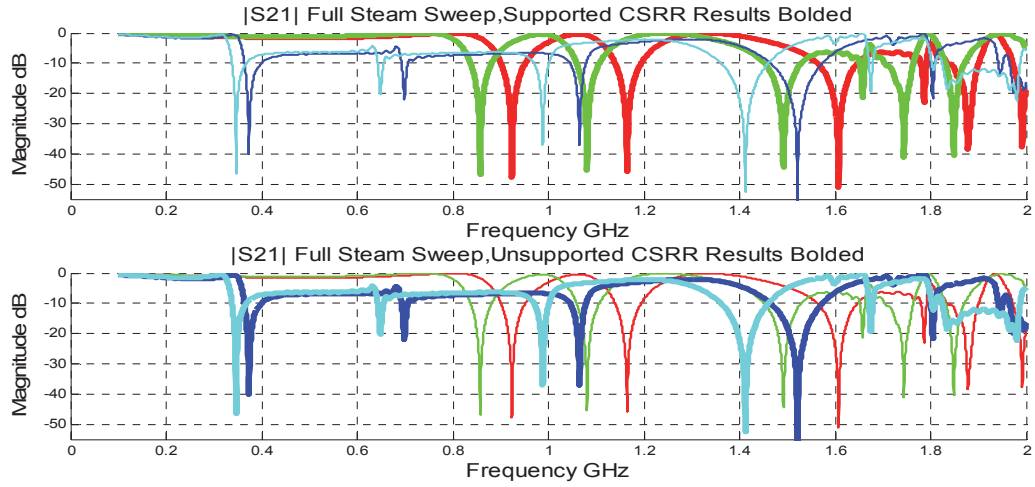
Fig. 35: Entire Pipe Steam Sweep, CSRR Supported / Non-supported Comparison

Table 6 and Table 7 show the frequency shifts of the S21 response of the simulation as the permittivity in the CSRR rings is varied. The lowest frequency null is labeled as null 1. The CSRR rings are labeled starting with the center ring as ring 1 and ring 4 the closest CSRR ring to the pipe wall. This was done to test correlation between CSRR ring resonance and S21 frequency nulls. The data in Table 6 shows the change in frequency of the null from

30% to 100% SQ for a supported CSRR and Table 7 shows the results from a simulated model without a support bar on the CSRR.

Observing the data from the supported CSRR simulation in Table 6 , the lack of a 4th null under cutoff frequency of the 4-inch pipe, 1.71GHz, prevents measurement of permittivity variations in the most centrally located ring 1.When the permittivity in ring 2 was varied a frequency shift was clearly visible in the 3rd null at a very large 33.5MHz shift. When the permittivity in ring 3 was varied, a frequency shift was detectable in the 2nd moving the null 24.5MHz. The 1st null shifted in frequency only when the permittivity in ring 4 was varied, the null shifted 14.0 MHz. These results match expectations that the frequency of the lowest frequency null is due primarily to the resonance of the largest ring. The sensitivity of the nulls when the entire pipe permittivity changes shows that the SQS permittivity using a TEM excitation method is largely due to the permittivity between the TEM conductor and the CSRR, not the permittivity of the material in the rings of the CSRR. The supported CSRR behaves more similarly to resonators in parallel than the unsupported equivalent discussed below.

Table 7 shows the results from a simulation using an unsupported CSRR with the remaining model made identically as the supported model. The results from the simulation were mixed, while some of the null frequencies did shift with varying permittivity, they did so in a less correlated manner than the supported structure. This implies that a CSRR structure without a support bar has more interdependent resonances than the supported CSRR. The frequency shift caused by variations in permittivity in rings 2 and 3 of the unsupported was also notably less than the support CSRR. Overall, an unsupported CSRR was observed to have null frequencies less sensitive to individual ring permittivities than a

40

supported CSRR. It is therefore recommended that a support structure between rings be employed if annular quality is further researched.

Table 6: S21 Frequency Nulls Permittivity Sensitivity for Supported CSRR Model

Δ Null Frequency	Permittivity Swept				
	Ring 1 only	Ring 2 only	Ring 3 only	Ring 4 only	Entire Pipe
ΔF Null 1	0.0 MHz	0.0 MHz	0.0 MHz	14.0 MHz	66.0 MHz
ΔF Null 2	0.0 MHz	0.5 MHz	24.5 MHz	4.5 MHz	83.5 MHz
ΔF Null 3	1.5 MHz	33.5 MHz	3.5 MHz	0.0 MHz	115.5 MHz

Table 7: S21 Frequency Nulls Permittivity Sensitivity for Non-Supported CSRR Model

Δ Null Frequency	Permittivity Swept				
	Ring 1 only	Ring 2 only	Ring 3 only	Ring 4 only	Entire Pipe
ΔF Null 1	0.5 MHz	0.5 MHz	2.0 MHz	3.0 MHz	27.0 MHz
ΔF Null 2	0.5 MHz	4.5 MHz	4.0 MHz	7.0 MHz	50.5 MHz
ΔF Null 3	3.0 MHz	10.5 MHz	13.0 MHz	3.0 MHz	77.0 MHz
ΔF Null 4	6.0 MHz	0.5 MHz	5.0 MHz	20.0 MHz	109.0 MHz

3.4 TEM Wire Deflection

One of the concerns about an excitation method that used a wire was the impact the steam flow on the wire. The primary concern is deflection of the wire caused by high velocity steam flow. A model was built using a circular cross-section PEC excitation wire with a radius of 6.35mm as shown in Fig. 36. The coupling wire across the CSRR in the flow of the steam was constructed such that it would deflect in a manner caused by uniformly applying a load to the wire. A design compromise had to be made for the Z_0 of the coupling wire transmission line in the model. A Z_0 of 50Ω would match the impedance of the coupling section to the SMA cables but would call for the wire to be only 1.2mm above the CSRR. This allowed for very little travel towards the CSRR before the excitation wire shorted against the rings of the CSRR giving the steam quality sensor an unreadable response. Thus

the coupling wire was placed 1.8mm above the CSRR and assuming a minimum permittivity

of 1.075 for the steam resulted in a maximum Z_0 of 59.8 Ω, see equations 5, 6. [13]

$$Z_0 = \frac{\eta_0}{2\pi\sqrt{\varepsilon_{reff}}} cosh^{-1}\left(\frac{2h+d}{d}\right) \tag{5}$$

$$\varepsilon_{reff} = \frac{\varepsilon_r + 1}{2} + \frac{\varepsilon_r - 1}{2} \cdot \sqrt{\frac{d}{d + 12h}} \tag{6}$$

The metal surfaces of the deflection model were simulated as PEC and the coaxial

dielectric was modeled using the Teflon dielectric from the default CST library. The

simulation was initially run using 100k mesh cells with perfect magnetic conductor (PMC)

boundary conditions at the ends of the pipe. The frequency range of the simulation was set to

sweep between 100MHz and 3GHz, even though the bandwidth of interest was known to lie

between 500MHz and 2GHz.

The wire was then vertically deflected towards or away from the CSRR measuring at

the wire midpoint, in increments of 1mm. Fig. 37. The wire's response with 0mm of

deflection or straight is given as 0 bend in the legend, deflection towards the CSRR is labeled

as (-) deflection and away from as (+) deflection.

The results in Fig. 37 show that the SQS $|S_{21}|$ response using a TEM wire is

definitively impacted by wire deflection. A deflection of several millimeters is a large

amount. The simulation was rerun with finer mesh cells and a smaller deflection step size.

The mesh cell count was increased to 424,270 overall by enforcing a maximum mesh cell

height of 0.6mm near the CSRR as seen in Fig. 38. This enforced a mesh condition such
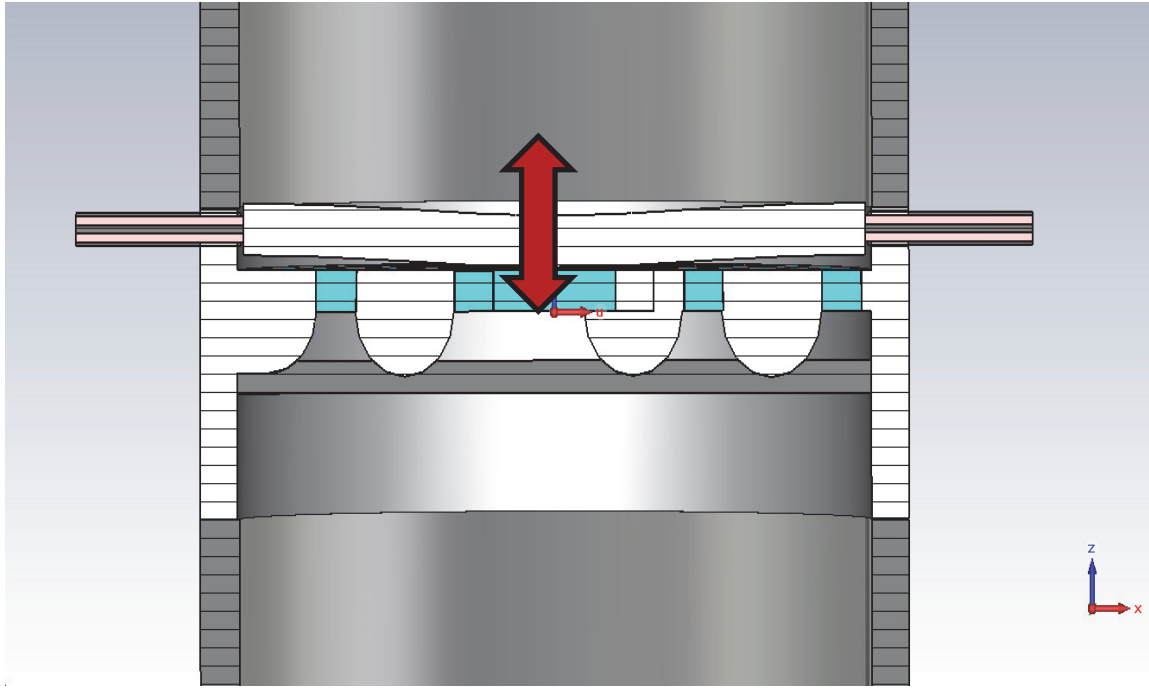
Fig. 36: Simulation of Wire Deflection
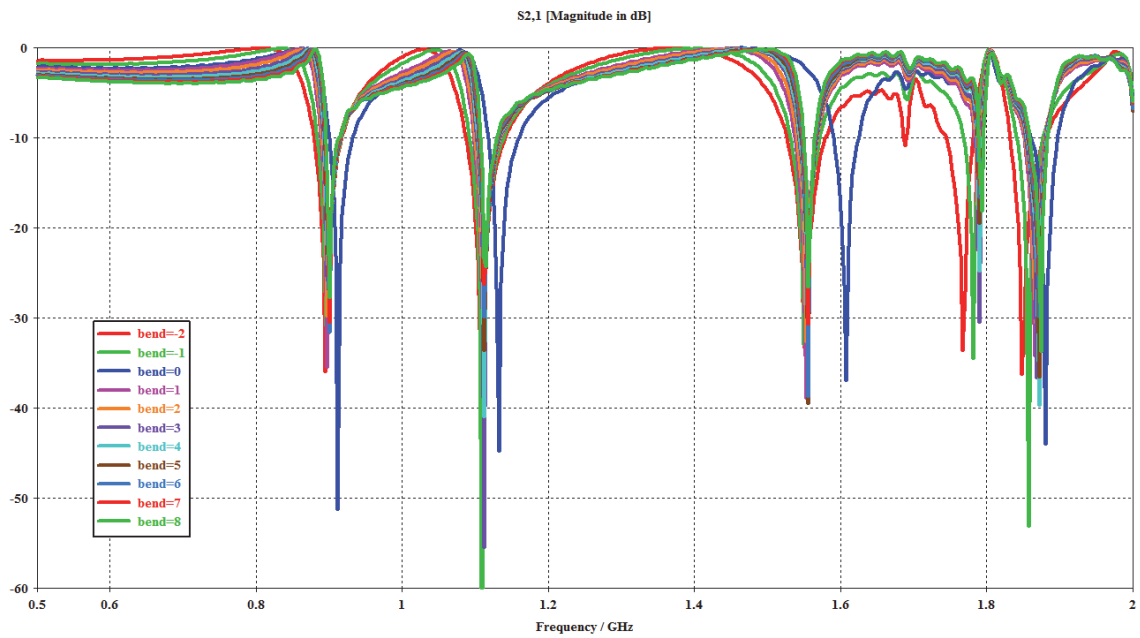
Fig. 37: $|S_{21}|$ Defection Simulation, 1mm Deflection Steps in Bandwidth of Interest

that there were at least 3 mesh cells between model features in the z dimension. The material was also changed so that only the pipe walls and the coaxial inner conductor were PEC; the remaining metal structures were modeled as mild steel, grade AISI-1010. The model was then re-simulated reducing the deflection steps to 0.5mm increments with a maximum deflection of +/- 1.5mm from the original straight position.
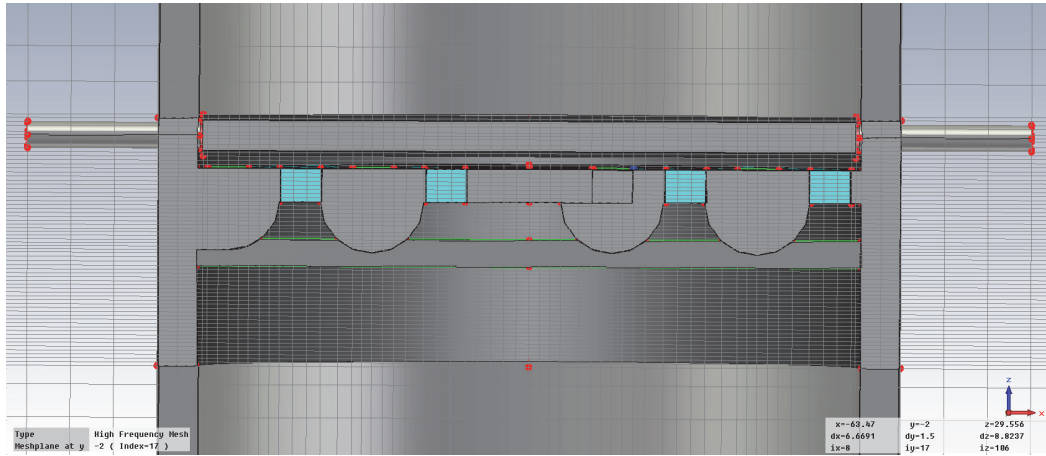
Fig. 38: Wire Deflection Model with 424k Mesh Cells

The simulation results can be explained by looking at the volume of the steam between the wire and the CSRR. The deflection of the wire reduced or increased the volume of steam between the wire and the CSRR, which therefore reduced or increased the capacitance between the wire and CSRR. The change in capacitance affects the characteristic impedance of the coupling wire segment increasing the reflections between the rod (coupling wire) and the coaxial lines. This effect can be most readily seen in the pronounced frequency shifts in the $|S_{11}|$ features in Fig. 39. For the $|S_{21}|$, a large decrease in null frequency was measured when the wire was deflected towards the CSRR, while the deflection away from the CSRR by the wire had less impact on the null frequency position. In conclusion a coupling rod in oscillating due to time-varying deflections will have detrimental effects on

the ability of the SQS to accurately measure steam permittivity by precisely determining null positions.
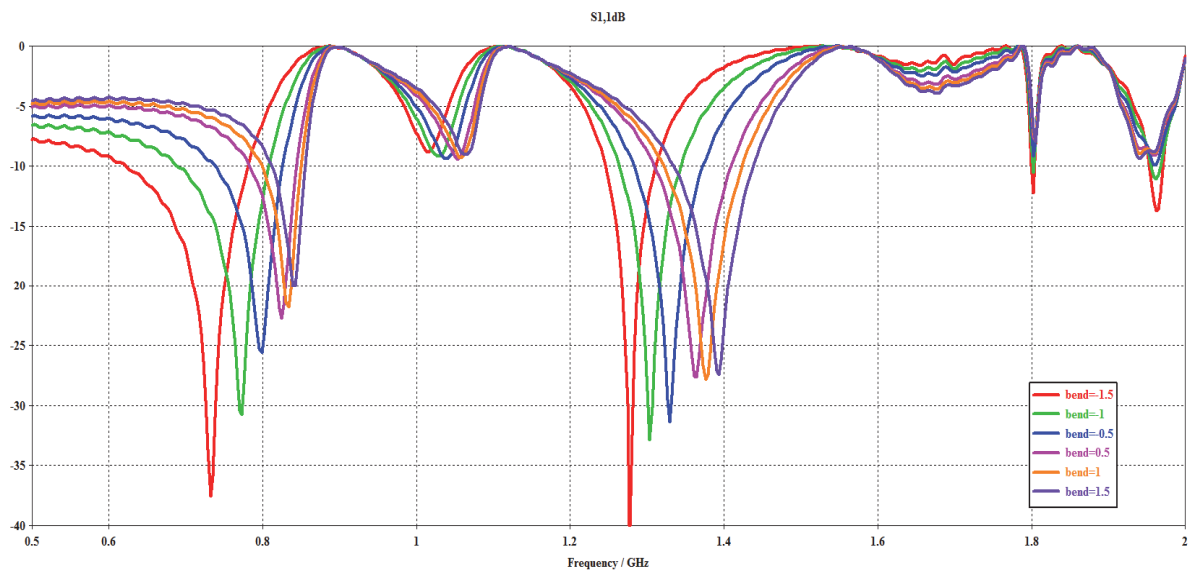
Fig. 39: |S11| Wire Deflection 0.5mm Sweep Simulation
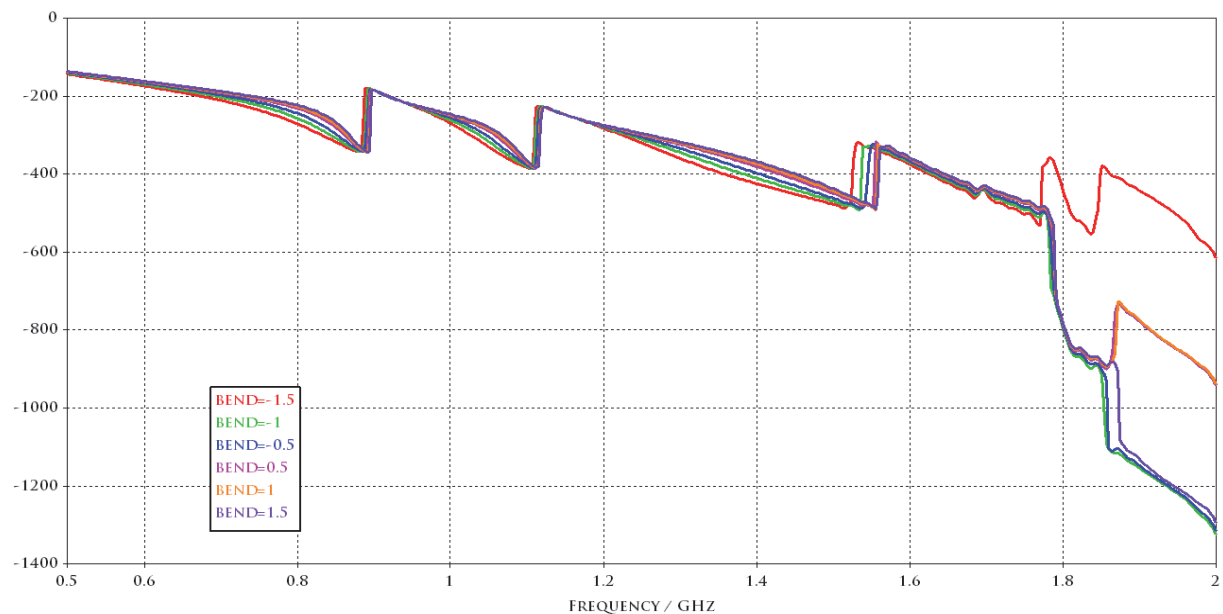
Fig. 40: Phase S21 Wire Deflection 0.5mm Sweep
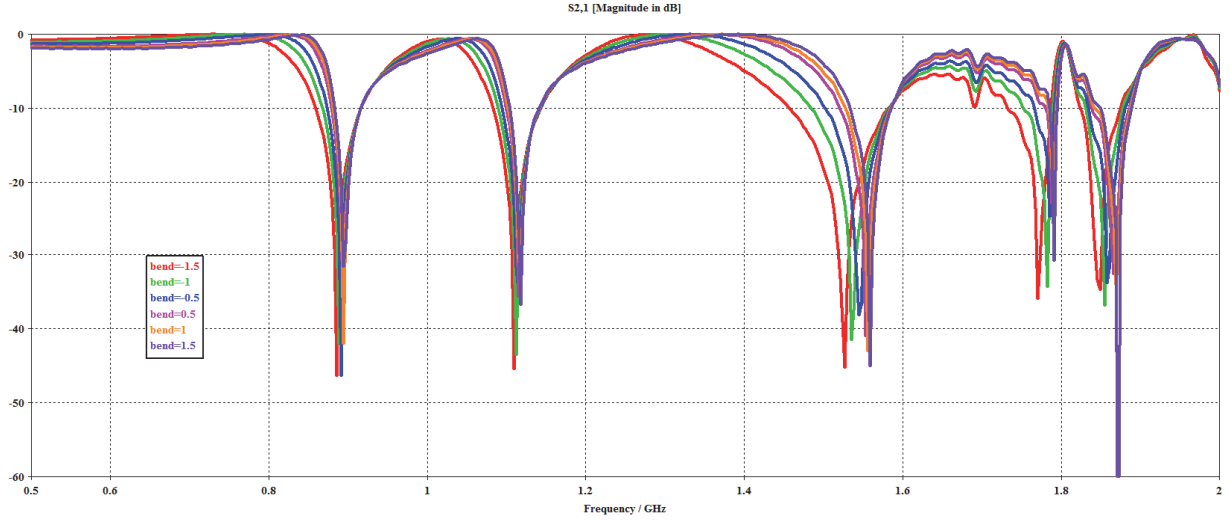
Fig. 41: |S21| Wire Deflection 0.5mm Sweep Simulation

3.5 Coaxial Impedance Matching Section Model

A major design challenge for high pressure and temperature sensor environments is the inability of polymer dielectrics to operate above $250\,^0C$. An alternative material for a high temperature dielectric for the coaxial transmission line segments was a ceramic oxide like oxidized aluminum, zirconia or yttrium. Ceramic oxides possess a very high compressive strength allowing the structure able to support the TEM rod in high pressure flow could be designed. Some ceramics are also weld-able affording adequate sealing to prevent steam leakage around the dielectric possible. Aluminum oxide, commonly referred to as alumina, retains its high strength at high temperatures at a more reasonable cost compared to other of oxides. Compared to silicon and nitrogen based ceramics, alumina ceramics have a very low loss tangent, ($\delta < 0.0009$) making them more ideal for use in transmission lines. More importantly, alumina has a very high permittivity (> 7.2) that can be increased with higher purity alumina [15]. Alumina is laser weldable to metal and is impermeable to water. These

46

properties allow for water-tight alumina dielectric supports to be designed for the TEM method of CSRR excitation to be constructed.

The high permittivity of alumina did, however, pose an interesting dilemma. The high permittivity of alumina meant that a coaxial transmission line would have to have either a very small center conductor or very large dielectric radius to achieve a Z_0 close to 50 Ω. To minimize the reflection coefficients caused by the mismatched characteristic impedances of the various transmission line sections and the PDNA an impedance matching solution was required. The characteristic impedance of the PDNA is fixed at 50Ω, thus the coaxial lines connecting to the PDNA should also be as close to 50 Ω as possible. Coaxial transmission lines have a characteristic impedance governed by (7) where d1 is the diameter of the center conductor and d2 is the diameter of the dielectric. The TEM coupling wire section has a characteristic impedance calculated using equation (5) [13].

$$Z_0 = \frac{60}{\sqrt{\epsilon_r}} ln(d2/d1) \tag{7}$$

3.5.1 Wire Deflection Due to Fluid Velocity

The coupling section rod diameter could not be too thin as it would deflect and change the impedance of the coupling section and any non-homogeneous steam flow would cause time-varying forces that could encourage the rod to oscillate. A simple calculation was performed to give a rough understanding of the magnitude of the force due to steam flow on the rod. The deflection of the solid rod was modelled as a 0.102m (4") long ATSM-A36 steel cylinder fixed by two simple supports at the ends. In practice, the rod will be held in rigid supports at both ends, so the actually deflection will be less than the calculated values here. The drag coefficient of the cylindrical rod was chosen to be 0.47 and with Young's modulus

of 200 GPa for steel at 25^0C. The fluid was liquid steam at 175 ^{0}C and 1.03Mpa with a density of 885 kg/m^3. The velocity of the steam was the greatest unknown variable, but a low velocity of 30m/s and a high of 60m/s which correspond to a steam mass flow rate of 214kg/s and 427 kg/s respectively were used. The radius of the rod was varied between from 6.35mm (¼") to 1.59mm (1/16").The moments of inertia of the circular and semi-circular rod are given in (8). The drag force on the rod is given by (9) where C_D is the drag coefficient of the rod and the area is given as the rod length multiplied by its diameter .The deflection of the rod is given in (10) using the midpoint of the rod where the deflection is at the maximum [16, pp. 1083-1087].

$$I_{circle} = \frac{1}{4} \pi r^4 = 2 \cdot I_{half\ circle} \tag{8}$$

$$F_{drag} = C_D * \rho_{steam} * L * D * velocity^2 \tag{9}$$

$$\delta_{max,L/2} = \frac{F_{drag} \cdot 0.5L}{24E \cdot I} \left(L^3 - 2L \left(\frac{L}{2}\right)^2 + \left(\frac{L}{2}\right)^3 \right) \tag{10}$$

Table 8: Estimated Max. Deflection at Steam Velocities for TEM Rods by Diameters

Type	Steam Velocity	Rod Diameter 12.7mm	Rod Diameter 6.35mm	Rod Diameter 3.175mm	Rod Diameter 1.59mm
Circular Cross Section Rod	30m/s	0.0026 mm	0.0210 mm	0.1679 mm	1.3435 mm
	60 m/s	0.0105 mm	0.0840 mm	0.6718 mm	5.3742 mm
Half-Circle Cross Section Rod	30 m/s	0.0047 mm	0.0375 mm	0.3002 mm	2.4012 mm
	60 m/s	0.0188 mm	0.1501 mm	1.2006 mm	9.6049 mm

Table 8 shows that thin rods allow for too much deflection even at the low estimate of fluid velocity to be reliably used in the SQS. The rod deflection is expected to increase with temperature as the elastic modulus of steel decreases with temperature. A minimum diameter greater than   3.175mm for the rod is most nearly necessary to avoid harmful coupling rod deflections.

 The use of a large diameter rod comes at the expense of a small coaxial cross section as a 6.35mm (¼") inner conductor using the lowest purity alumina (85%) still requires a dielectric diameter of 68.6mm to achieve a 50 Ω characteristic impedance. Here in lies the problem. To achieve a 50 Ω impedance in the coaxial line segment would require the 6.35mm rod to be placed at least 34.3mm away from the CSRR giving the coupling line section a Z_0 of 190 Ω yielding a distance of 34.3mm using a 68.6mm coaxial line cuts the orifice plate, rendering it no longer a simple shape. A non-round CSRR orifice plate would add additional manufacturing and testing costs to be considered a practical solution.

The remaining options were to either use non-matching characteristic impedance lines or to have a different coaxial center conductor dimensions than the coupling rod. The solution involved the design of both; coaxial transmission lines sections with small center conductors would have varying dielectric radiuses to achieve different impedances. The proper selection of the lengths of these lines could allow them to act as quarter-wave transformers to successively step-up the line impedance better matching the PDNA to the higher impedance coupling section. A design was modeled using a 6.16mm diameter steel coupling rod as the TEM coupling conductor with 3 stages of coaxial transmission line that varied in dielectric diameter with each segment as shown in Fig. 42. A close up of the coaxial section shows the 3 stage impedance network. The matching network was broken down into

3 sections, S1, S2, S3 each having an independent inner conductor diameter, dielectric diameter, and length.

The S3 section was designed to be as electrically short as possible, yet long enough to not to cause the alumina to fail due to pressure exerted by the rod exceeding the compressive or tensile strength of the alumina-rod interface . When the length of transmission line is very small compared to the wavelength of the signal, transmission line effects play a reduced role in wave propagation. Ulaby provides a generalized rule of thumb that when a line's length is less than 1/100 of the wavelength it can generally be ignored [17, p. 63]. In a 96% pure alumina dielectric, the wavelength at 2GHz is 50mm, thus a line length of 0.5mm or less is preferred to mitigate the effects of the low characteristic impedance.

Section S2 was designed to be a gradual transition from the lower impedance coaxial line segment, S1, to the higher impedance coupling line segment. The dielectric diameter of this section transitioned from the dielectric diameter of S1, DE1 to the dielectric diameter of the 3rd section DE3 as shown in Fig. 43 .
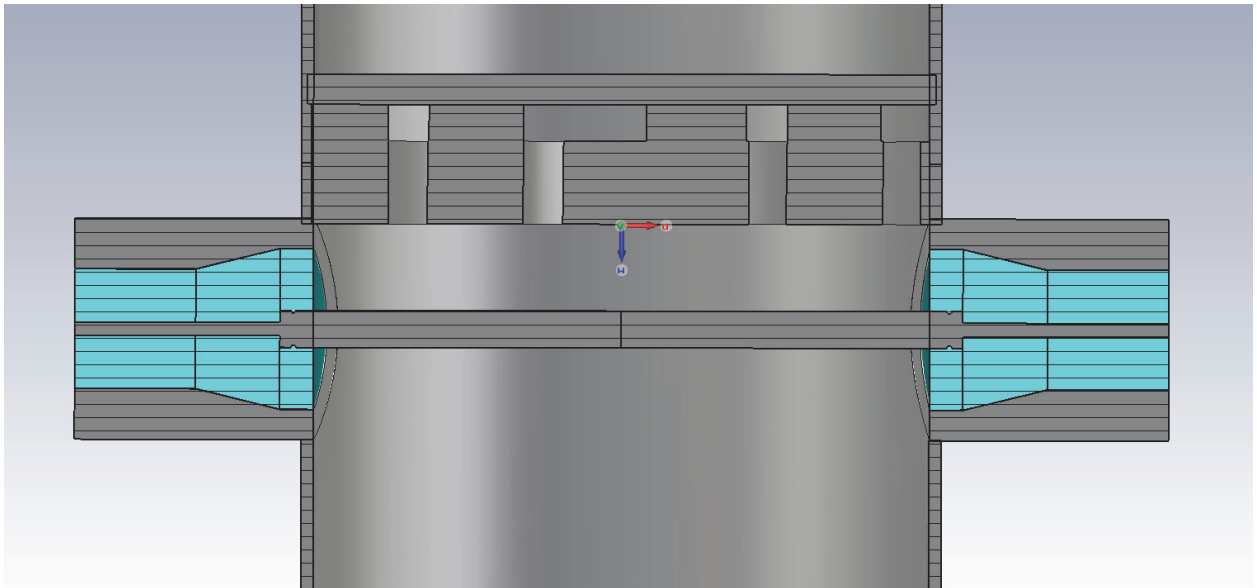
Fig. 42: Multi-stage Coaxial Matching Network Design Model
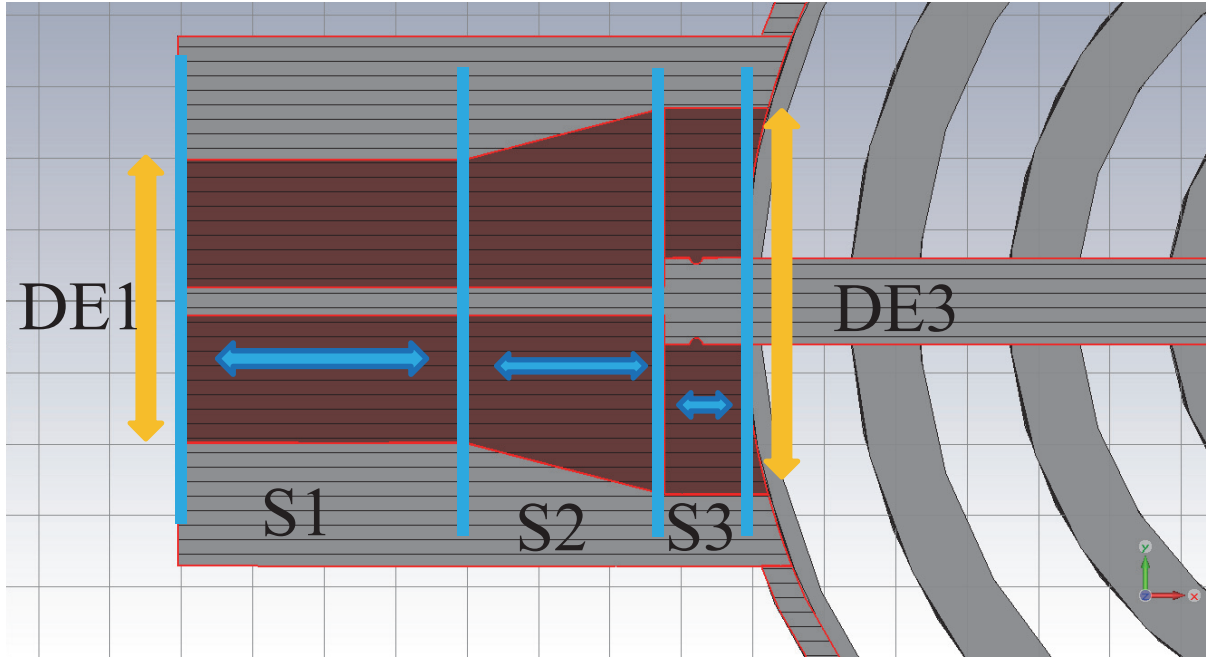
Fig. 43: Multi-Stage Coaxial Design Coaxial Transmission Line Parameters

The problem with using a quarter-wave transformer approach to the matching problem was bandwidth; a single stage quarter-wave transformer has limited bandwidth dependent upon the proximity of the load impedance to the Z_0 of the line [8, p. 242]. The lower the impedance mismatch between the characteristic impedance of the coaxial line and the coupling line, the greater the bandwidth of the match. A multi-section quarter-wave transformer network increases bandwidth without requiring the load impedance to change, but requires more space and a known load impedance to match to. Here the load is seen as the coupling line characteristic impedance, Z_{CL}. Z_{CL} depends on the height above the CSRR and the diameter of the coupling rod. The impedance of section 3 has to be considered as well as a length of 0.5mm is deemed too short to properly affix the rod ends. Thus, DE3 too plays a role in to total impedance match of the sections.

The CST structural optimizer tool was employed to help achieve a minimized S_{11} and S_{22} and maximum S_{21} over the non-resonant bands. The first parameters optimized were the support bar to CSRR distance, the distance between the coupling rod and the CSRR, and the thickness of the CSRR. The initial algorithm chosen was the classic Powell algorithm with a domain accuracy of 0.01. If a parameter neared its predefined 10% limit then the simulation was rerun with a slightly lower or higher bound for that particular parameter. The first few simulations of the optimizer evaluated 23 different combinations before settling on values only slightly varied from the initial.

A second optimization was performed using the trusted region framework algorithm with a domain accuracy of 0.0001. The gaps between the rings, the 3 coaxial dielectric thickness, length of the 3 coaxial sections, and the conductor thickness were added as parameters which the optimizer could use. The parameters were again allowed to move within 10% of their initial value.

Table 9: Resultant Parameter Values from 2nd Optimization

Parameter	Initial Value	Optimized Value
Length of Section 1	20 mm	20.0 mm
Length of Section 2	10 mm	13.89 mm
Length of Section 3	8 mm	8.9 mm
Rod Diameter	13.5 mm	13.2 mm
Rod distance from CSRR	20 mm	17.3 mm
CSRR plate thickness	12.45 mm	13.7 mm
CSRR Ring 1 Gap Width	6.35 mm	6.52 mm
CSRR Ring 2 Gap Width	6.35 mm	6.33 mm
CSRR Ring 3 Gap Width	6.35 mm	6.37 mm
CSRR Ring 4 Gap Width	6.35 mm	6.32 mm

The results of the optimization were used as base parameters in another simulation. In the new simulation, engineering judgment was used in selecting some of the parameter values instead of the software values. The length of the 3rd coaxial section S3 was reduced to be less than 5mm as well as reducing the diameter of the center conductor of the 1st and 2nd coaxial segments to 0.5mm. The impedance of S1 was set at 50Ω which results in a 6mm value for DE1. The CSRR thickness was also varied between 6.35mm and 13.5mm to see the response. The coupling rod diameter was set at 6.35mm. The distance between the support bar and the CSRR was fixed at 6mm. The volumetric mixing equation using the densities and dielectric constants for 175^{0}C/1.03Mpa steam was used in the calculation of the effective dielectric constant of the saturated steam mixture at different qualities. The metal structures were also replaced with the CST material model of steel-1010 to account for actual conductor losses. The steam also had a small amount of conductivity loss included at 10μS/m. Alumina was used as the dielectric in the coaxial segments with a permittivity of 9.
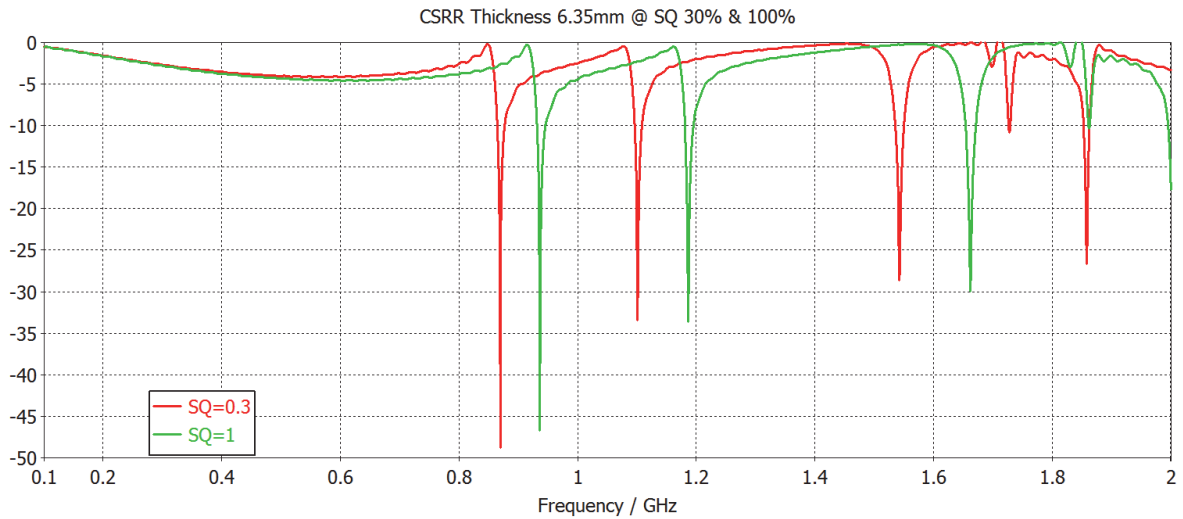
Fig. 44: |S21| SQ Sweep for 6.35mm CSRR
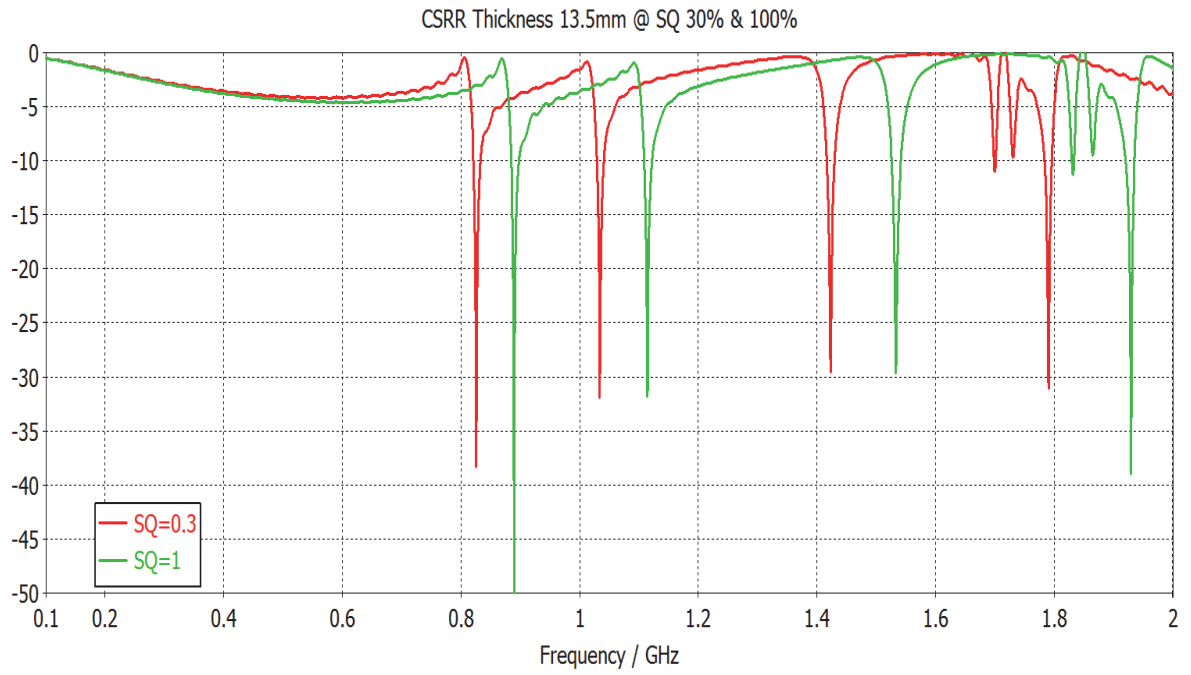
Fig. 45: |S21| SQ Sweep for 13.5mm CSRR
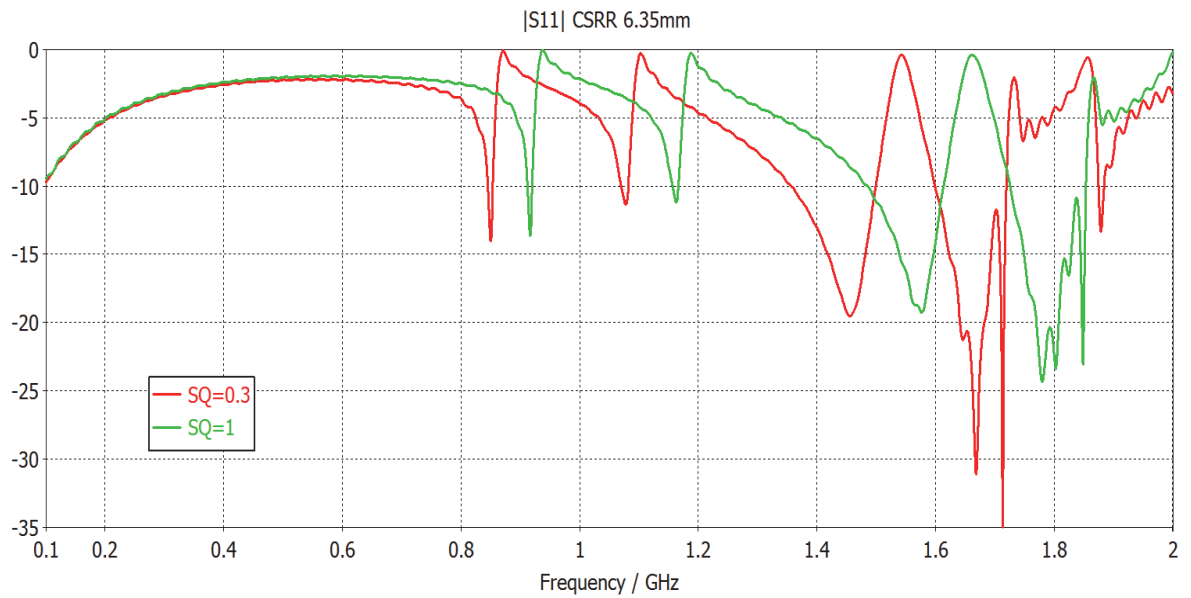
Fig. 46: |S11| 30% and 100% SQ @ CSRR Thickness of 6.35mm

54
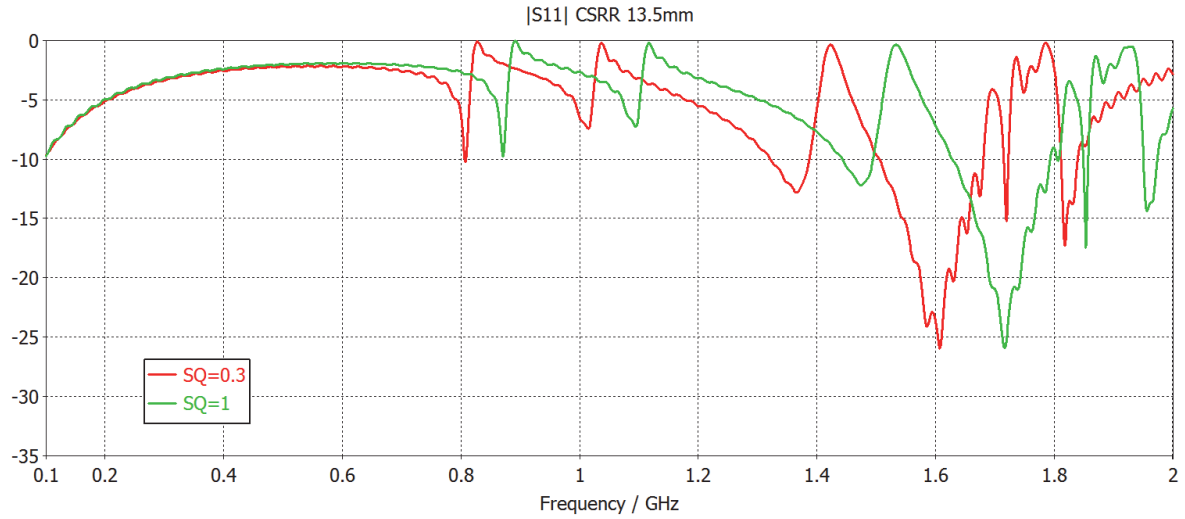
Fig. 47:|S11| 30% and 100% SQ @ CSRR Thickness of 13.5mm

While the revised simulation's |S11| results are slightly worse than the previous, the model did perform acceptably well in terms of the |S21| null quality. An interesting observation to be made about the |S21| response is best seen in Table 10, where the thicker CSRR significantly increased the capacitance of each ring, lowering the null frequencies. The model was again optimized using the trusted region algorithm; however, the resultant changes to the S11 and S21 were so miniscule that they were ignored. A matching network design warrants further investigation in the future if TEM rods are considered to be used as coupling structures. The majority of the work lies with realizing the coaxial structures with purchasable or machinable parts as well as an adapter for the system to use SMA cabling.

Table 10:S21 Null Frequencies vs CSRR Thickness using Coaxial Network TEM Rod

SQ=30% CSRR_T = 6.35mm	SQ=100% CSRR_T = 6.35mm	SQ=30% CSRR_T = 13.5mm	SQ=100% CSRR_T = 13.5mm
0.870 GHz	0.937 GHz	0.826 GHz	0.890 GHz
1.101 GHz	1.187 GHz	1.034 GHz	1.114 GHz
1.543 GHz	1.662 GHz	1.423 GHz	1.533 GHz

3.7 TEM Design Conclusions

A connector solution that was able to satisfy the requirements of stabilizing an across flow rod, maintaining a good RF contact, have a low reflection, a closely matched impedance, and capable of surviving the environment of a steam system was not achieved. A suitable commercial off the shelf part or industrial device that fit this description and could be used could not be obtained, primarily because polymer dielectrics service the majority of RF connectors. The use of alumina requires special manufacturing considerations if small complicated shapes are formed. This would greatly increase the project cost. If a suitable RF connector could be found to firmly hold a large diameter rod, then a TEM excitation structure could provide a very effective permittivity measure of saturated steam. A TEM excitation of the CSRR provides good steam quality measurements in a low flow system where wire vibration is not prevalent.

A potential disadvantage with the TEM structure design is the majority of the measurable resonant shifts in permittivity are due to the material between the conductor and the CSRR, and not material between the rings. A profile radial steam quality is difficult to measure as the resonant frequencies shifts are weakly dependent on ring steam quality using a TEM structure, yet an aggregate pipe steam quality is easily attainable.

CHAPTER FOUR

Nested Waveguide Design

Since a simple, practical, and constructible design was unable to be developed for a TEM excitation structure alternatives of wirelessly exciting the CSRR were researched. Dr. Jean proposed a possible solution; nest a parallel plate waveguide (PPWG) inside the pipe upstream the CSRR, exciting the PPWG with a TE_{10} wave. This would cause the electric field to be perpendicular to the plates of the PPWG and parallel to the surface of the CSRR. The energy from the fields would then couple to the PPWG and contain the fields that had components at the resonant frequencies. This would prevent the transmitted signal from traveling between the two ports at the resonant frequencies of the CSRR as the signal energy at the resonant frequencies would be stored in the rings instead of transmitted.

It is noted in the literature, however, that parallel E-field excitation is unable to properly excite a CSRR, although a parallel magnetic field is capable [14]. Excitation by perpendicular E-fields provides more sensitivity to the permittivity of material in and near a CSRR [18]. The design to obtain perpendicular electric fields coupled to the CSRR was based upon the use of the fringing effects at the ends of a finite width PPWG. The use of the fringing fields produced at the ends of the parallel plates became the primary method of coupling perpendicular electric fields with the CSRR.

4.1 Parallel Plate in a Circular Waveguide

A model was created to verify the theoretical understanding of how a parallel plate waveguide would behave in a larger cylindrical waveguide. An ideal model was developed that incorporated a PPWG inside a 4" pipe feed via a dielectrically loaded rectangular waveguide (RWG) which was excited at the ends using waveguide ports in CST, see Fig. 48. The equations for the cutoff frequency of the TE_1 mode for parallel plate waveguides and the TE_{10} mode for rectangular waveguides for a dimension, a, are the same and are given below in (11). The wave impedance for the TE_{10} mode for RWG or TE_1 mode for PPWG is found using (12) [8, pp. 98-115]. The PPWG was excited with an electric field perpendicular to the PPWG plates thus was not governed by a cutoff frequency for the TE_1 mode using this field orientation. Below the cutoff frequency of the RWG, there is no traveling wave propagation down the RWG into the pipe cavity, only evanescent waves which decay very rapidly. A TE mode does not form or forms weakly in the PPWG as the propagation constant of the RWG becomes an imaginary number under the RWG cutoff frequency.

$$f_{c,PPWG} = f_{c,RWG} = \frac{1}{2a\sqrt{\mu\epsilon}} \tag{11}$$

$$Z_{TE1,PPWG} = Z_{TE10,RWG} = \frac{k\eta}{\beta} = \frac{\omega\mu}{\sqrt{\omega^2\mu\epsilon - \frac{\pi^2}{a^2}}} \tag{12}$$

When a waveguide is dielectrically loaded, the cutoff frequency decreases as a function of the square root of the permittivity. Thus a relatively small waveguide that would have a very high cutoff frequency in air will have a much lower cutoff frequency when filled with a ceramic dielectric. The dielectric chosen was 94% pure alumina with a relative permittivity of 9.0. The rectangular waveguide dimensions were 50mm by 50mm. The

58

parallel plates of the PPWG were chosen to be 50mm and have a width of 50mm. The cutoff

frequency of the waveguides was slightly less than 1GHz for the RWG TE_{10} mode. The

boundary conditions for the simulation were PMCs at the pipe ends, PEC on the top and

bottom, and open with added space behind the waveguide ports, as shown in Fig. 49.
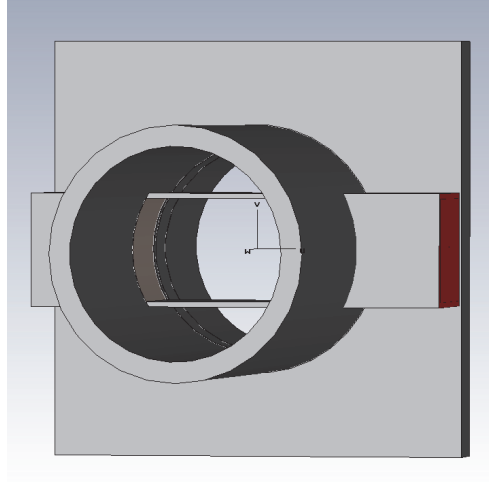
Fig. 48: PPWG in Pipe
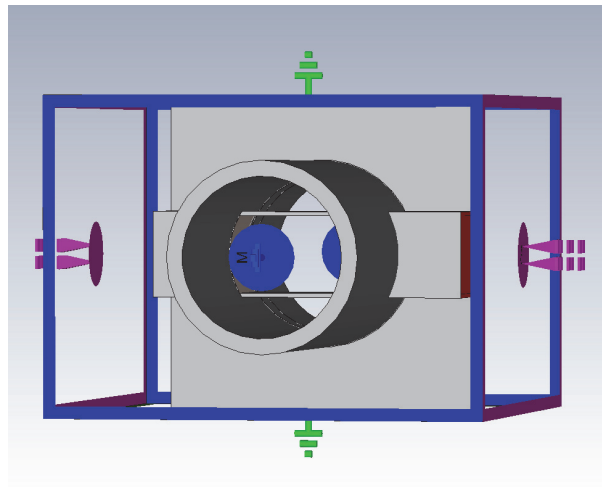
Fig. 49: Boundary Conditions PPWG in Pipe

The simulation shows the rectangular waveguide begin to propagate around 1GHz with the wave travelling across the pipe via the PPWG. At approximately 1.7GHz the wave begins to travel down the pipe and the |S21| begins to fall as Fig. 50 shows.
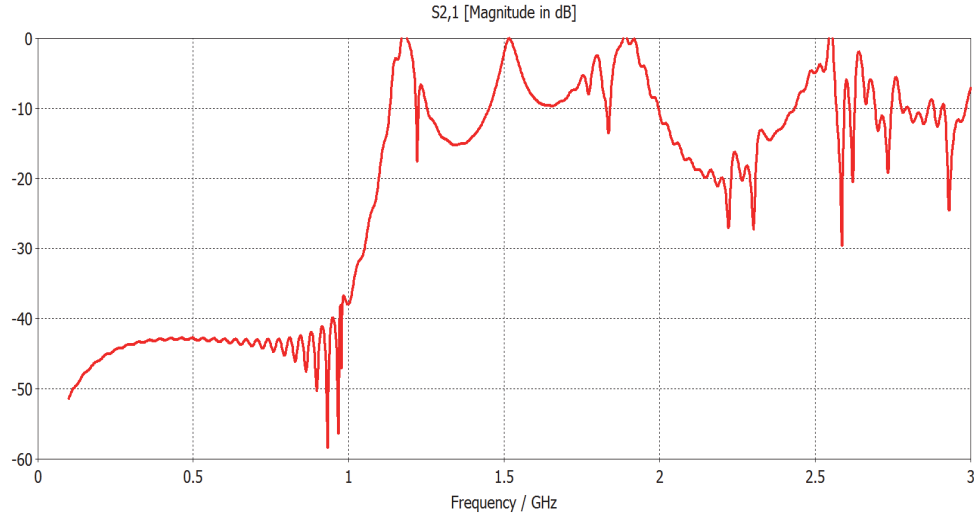
Fig. 50:|S21| of PPWG in 4" Pipe

4.2 Waveguide Port Excited PPWG with CSRR

4.2.1 CSRR Response with Waveguide Port Excitation from PPWG

The 6.35mm ring radius 13.5mm thick CSRR OP used in chapter 3 was again inserted into the model developed for the PPWG in section 4.1. The CSRR was oriented as is shown in Fig. 51 with a support bar placed 6mm behind the CSRR on rectangular braces instead of the previously used rounded braces. Both the support bar and the braces were 4.775mm wide. All metal components were modeled using the steel-1010 material model in the built in CST library.
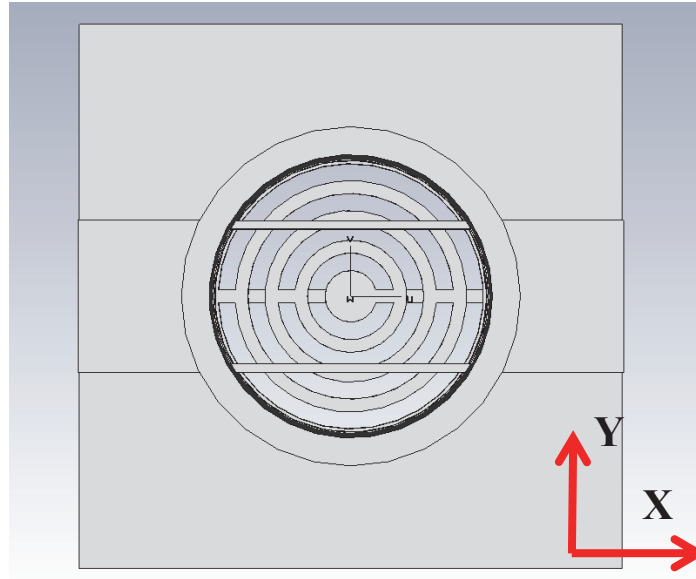
Fig. 51: Top View of CSRR using PPWG Model
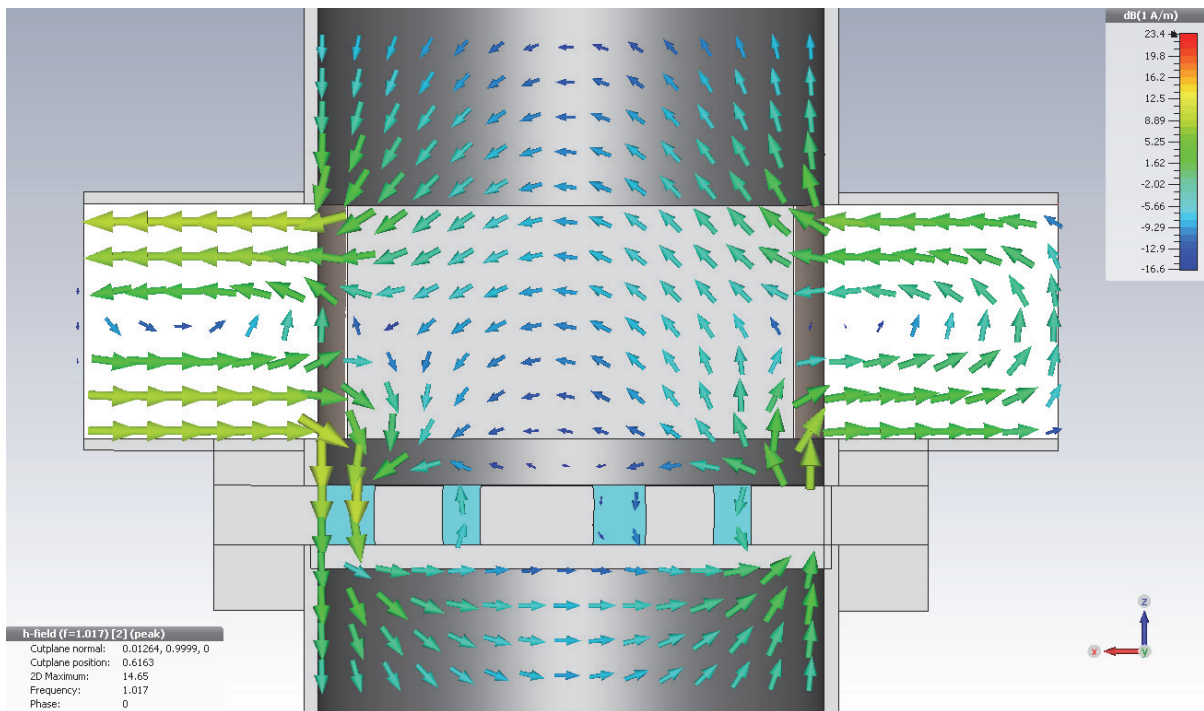
Fig. 52: H-field, Waveguide Excited PPWG @ 1GHz
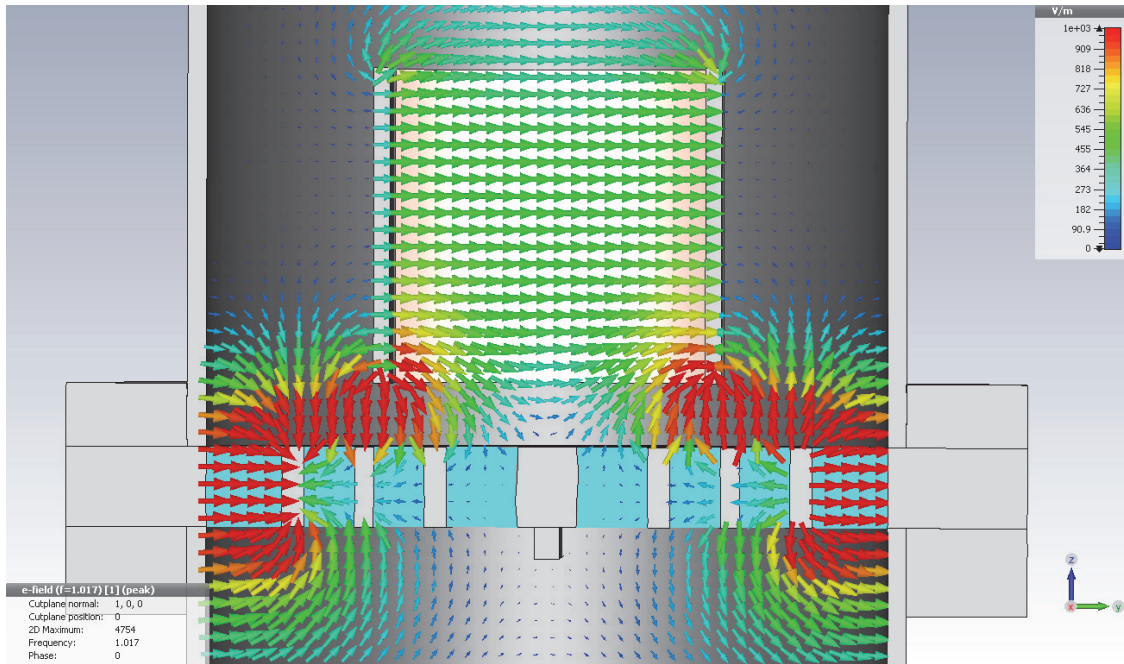
Fig. 53: E-field, Waveguide Excited PPWG @ 1GHz
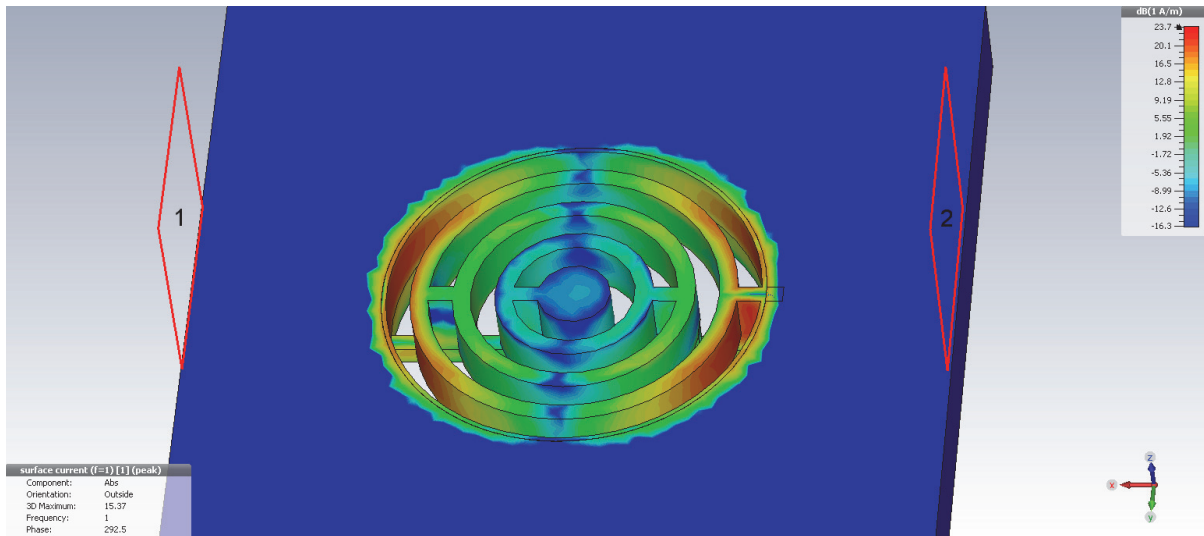
Fig. 54: Surface Current on 6.25mm Radius CSRR Rings @ 1GHz

The magnetic field for the model at 1 GHz is shown in Fig. 52; the magnetic field for

a TE_{10} is evident in the RWG. The CSRR disturbs the magnetic fields as they enter the pipe

forcing them to loop around the CSRR structure. Fig. 52 shows the strong fringing electric

fields from the PPWG plates to the CSRR. Fig. 53 shows the magnitude of the surface current induced by the magnetic field looping around the CSRR rings. These fields are all shown for the 1.00785 steam permittivity at 1GHz. The waveguide ports excite the rectangular waveguide as expected with electric fields in the y direction. The S-parameters for the model are shown in Fig. 55 and Fig. 56.
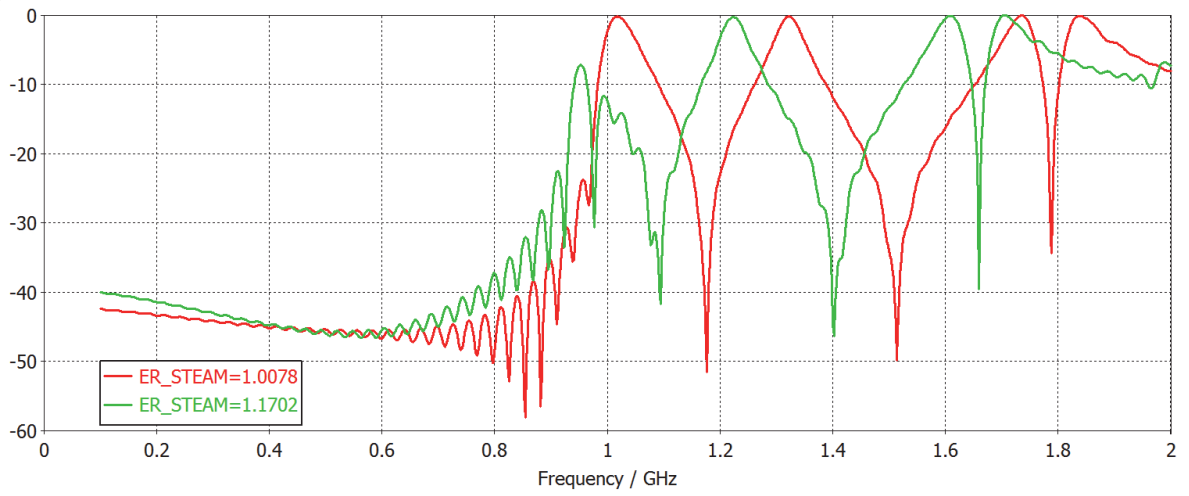
Fig. 55: |S21| PPWG with CSRR
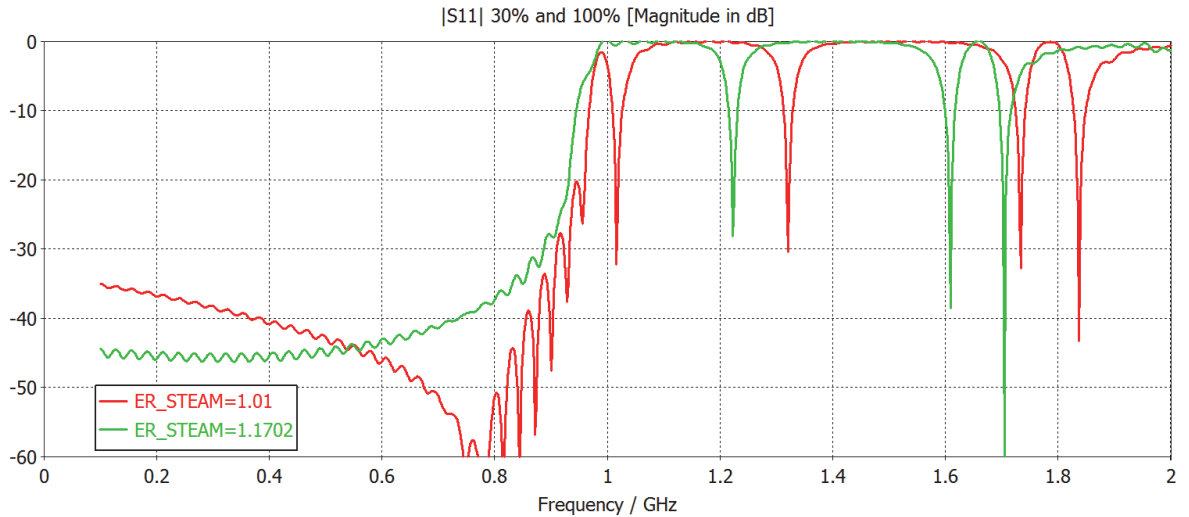
Fig. 56:|S11| PPWG with 6.25mm Ring Radius CSRR

63

The inclusion of the CSRR to the PPWG behaved like a notched stop band filter. The fields behaved as anticipated with heavy fringing electric fields strongly coupling to the CSRR top surface inducing electric fields within the CSRR gaps.

4.2.2 CSRR Orientation Response

The CSRR excited ideally excited using a PPWG was again re-simulated to verify that the current orientation of the CSRR with respect to the PPWG was indeed the correct orientation. A CSRR's orientation to the excitation field whether magnetic or electric is crucial. Though typically CSRRs are excited using perpendicular electric fields, it has been done using magnetic fields in the plane parallel with the CSRR [14]. According to the authors, in our orientation a magnetic field in the y-direction would be able to excite the CSRR. The CSRR in the model was rotated counterclockwise in two increments of 45^0 until it reached 90^0 as shown in Fig. 57 at a steam quality of 100%.
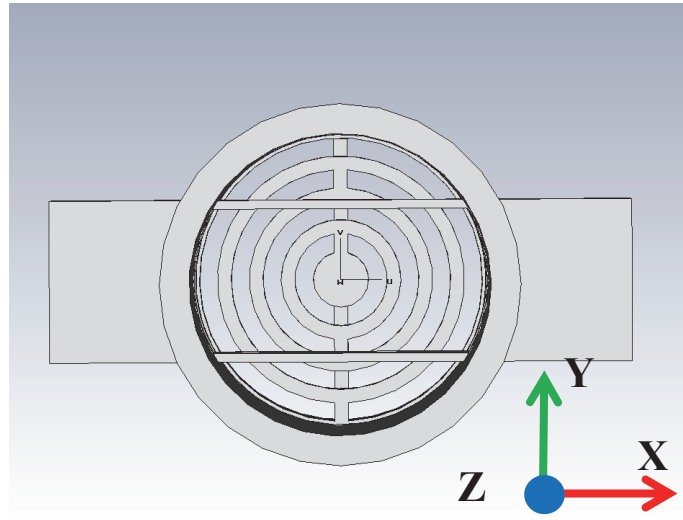
Fig. 57: CSRR excited via PPWG rotated 90^0 counterclockwise
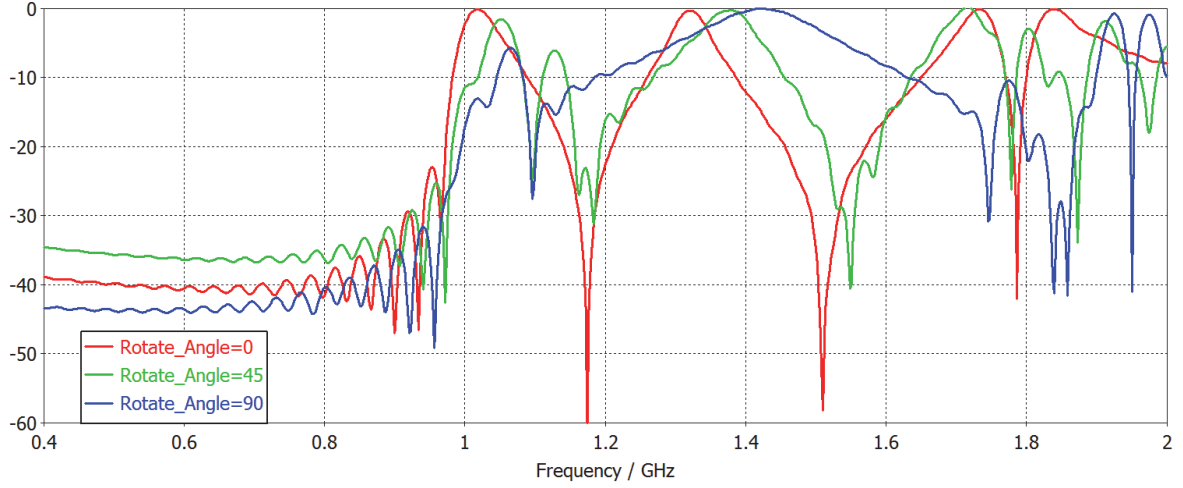
Fig. 58: |S21| CSRR Orientation using PPWG

The visible effects of wave polarization and CSRR orientation are evident in the decay of the first pass band and first null destruction. As the CSRR is rotated further out of proper excitation with the PPWG the less the structure is excited and its peak and null response shifted and distorted. The original 0^0 rotation is clearly ideal.

4.2.3 CSRR Beta Improvement

The beta of the previously used orifice plates for the PPWG simulations was 0.752, not including the support bar. It was felt Observations from the previous simulations showed that the permittivity in the first ring of the CSRR did not significantly affect the pass and stop bands of the S21 response as its resonance was well above the measured bandwidth of 2GHz. Thus, increasing the gap distance between ring 1 and ring 2 would raise the beta without losing permittivity extraction capability. The gap distances in rings 2 and 3 were also increased by 1.5mm to improve beta, but not greatly increase the resonant frequencies of the rings. A CSRR with a higher beta was designed using the gap the thicknesses or distances between metal rings shown in Table 11. The beta of the new CSRR was calculated to be

65

around 0.889 is the 4mm wide support bar facing upstream is not included and 0.787 if the support bar is accounted for.
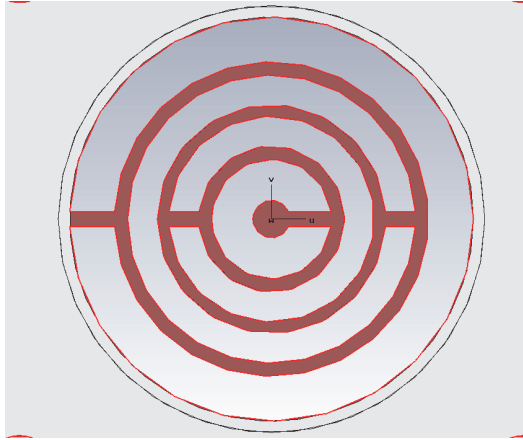
Fig. 59: High Beta CSRR, shown without support bar

Table 11: High Beta CSRR Dimensions

Ring Number	CSRR Dielectric Gap Radius Inside	CSRR Dielectric Gap Radius Outside	Effective Gap Spacing
1 (Innermost)	9.0 mm	16.0 mm	11.0 mm
2	19.5 mm	27.5 mm	8.0 mm
3	30.5 mm	38.5 mm	8.0 mm
4 (Outermost)	42 mm	54 mm (pipe radius)	12.0 mm

The model was re-simulated with the larger beta CSRR OP. The |S21| is plotted against a modeled steam quality from 30% to 100% in Fig. 60. The response between the lower and higher beta CSRRs looks very similar, and their response for 1.00785 permittivity or 100% quality steam is comparable in Table 12.
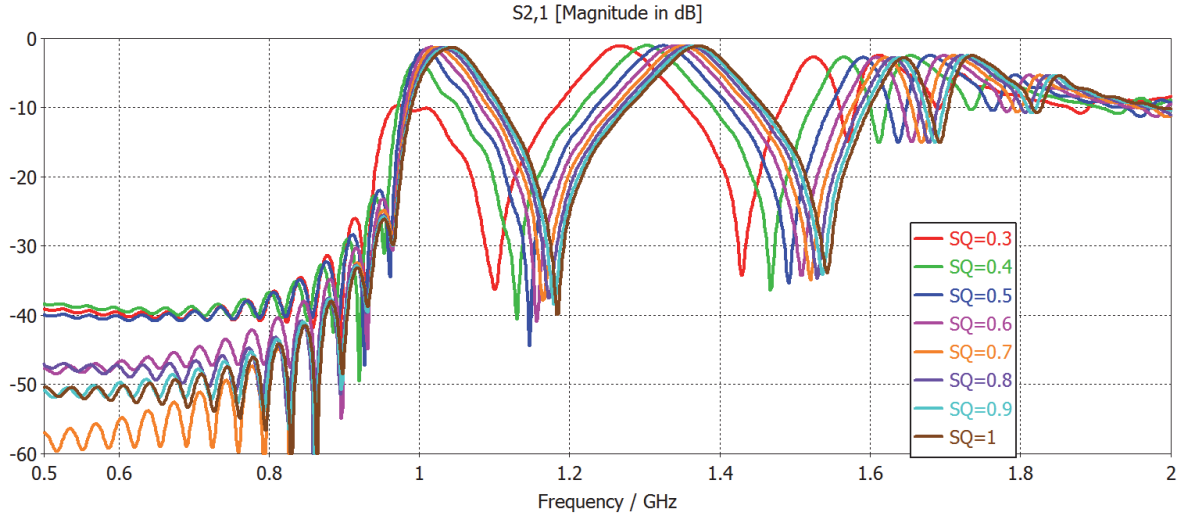
Fig. 60: |S21| Steam Quality Sweep with High Beta CSRR

Table 12: Low and High Beta CSRR Feature Frequencies

Low Beta CSRR S21 Peaks	High Beta CSRR S21 Peaks	Low Beta CSRR S21 Nulls	High Beta CSRR S21 Nulls
1.0223 GHz	1.0425 GHz	1.1745 GHz	1.1831 GHz
1.3402 GHz	1.3722 GHz	1.5118 GHz	1.5427 GHz
1.6951 GHz	1.6472 GHz	1.7867 GHz	1.6921 GHz

4.3 Rectangular Waveguide Excitation Structures

The design focus of the SQS now shifted to realizing a RWG excitation structure that could excite a TE_{10} mode with an ideal bandwidth of 900MHz to 1.7 GHz. Two types of structures were researched. The first was a magnetic coupling-loop structure borrowed from the design of the guided microwave spectrometer (GMS) [19]. The other structure is a widely used waveguide probe structure used to transition coax to waveguide [20].

4.3.1 Coupling Loop

The first structure investigated was the coupling loop used in the GMS. If the magnetic field is excited in the proper manner by the coupling loop, a TE_{10} mode is generated allowing for the proper field coupling to the CSRR using the PPWG. The magnetic coupling loop was first modeled with a 75Ω SMA coaxial line. This coaxial line connected to a U-shaped copper wire centered in the middle of the RWG with controllable height and length. The loop re-entered the back-wall of the RWG into another coaxial section connected to a discrete resistance element terminating the coaxial line as shown in Fig. 61. For the first simulation the height of the loop was set at 1mm with a 40mm loop length with a radius of 1.2mm. The RWG dimensions were 50mm by 50mm with the RWG back-wall located 50mm from the opening to the pipe. The coaxial line load resistance was set at 75Ω. The simulation boundary conditions and solver setup were the same as the ideal waveguide port excited model. The distance between the bottoms of the PPWG plates to the top of the CSRR was 10mm.

After simulation, the fields of the model were checked to verify the desired polarization of the electric and magnetic fields. The magnetic field looped in the XZ plane with poor strength and coupled poorly into the outer ring as shown in Fig. 62, and parallel components across the entirety of the CSRR top. The electric field was perpendicular to the PPWG plates and propagating in the TE_{10} in the RWG, as shown in Fig. 63. It lacked however the high strength fringing fields seen using the ideal waveguide excitation structure, even though the fields were extremely strong in the RWG. The inadequate coupling of the perpendicular electric fields helps explain the poor S21 performance of the system as the CSRR was not coupled with strong fields, particularly the magnetic field.

68
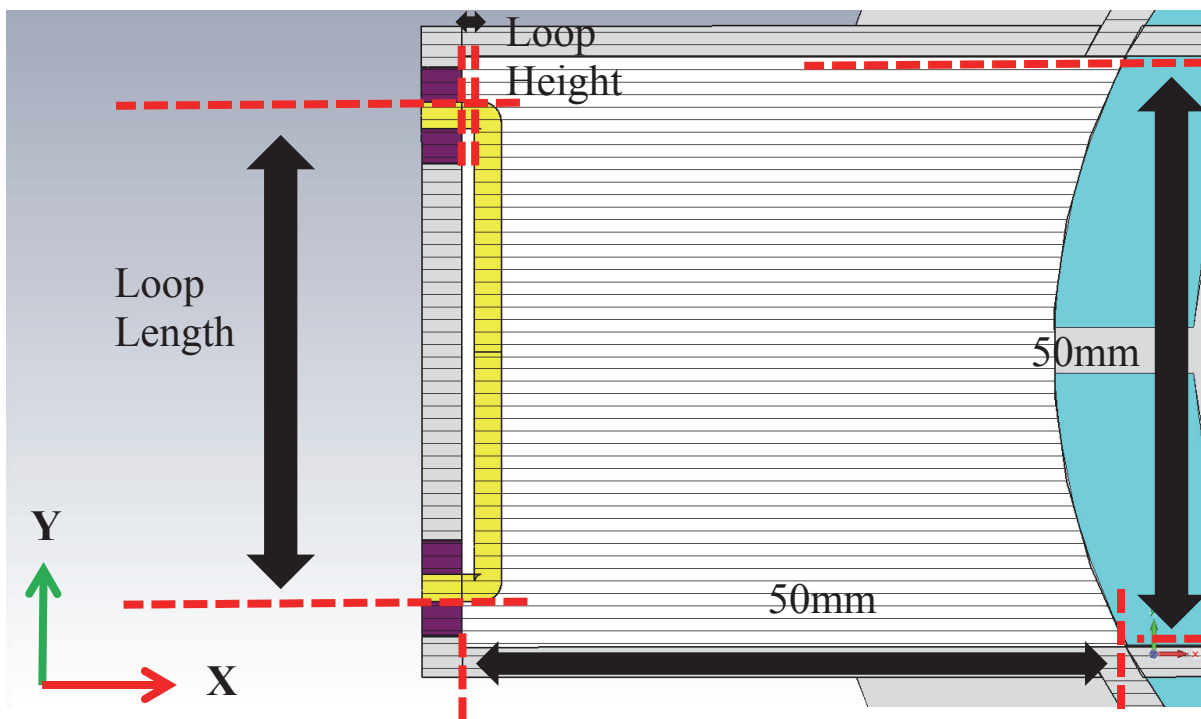
Fig. 61: Coupling Loop Dimension Parameters
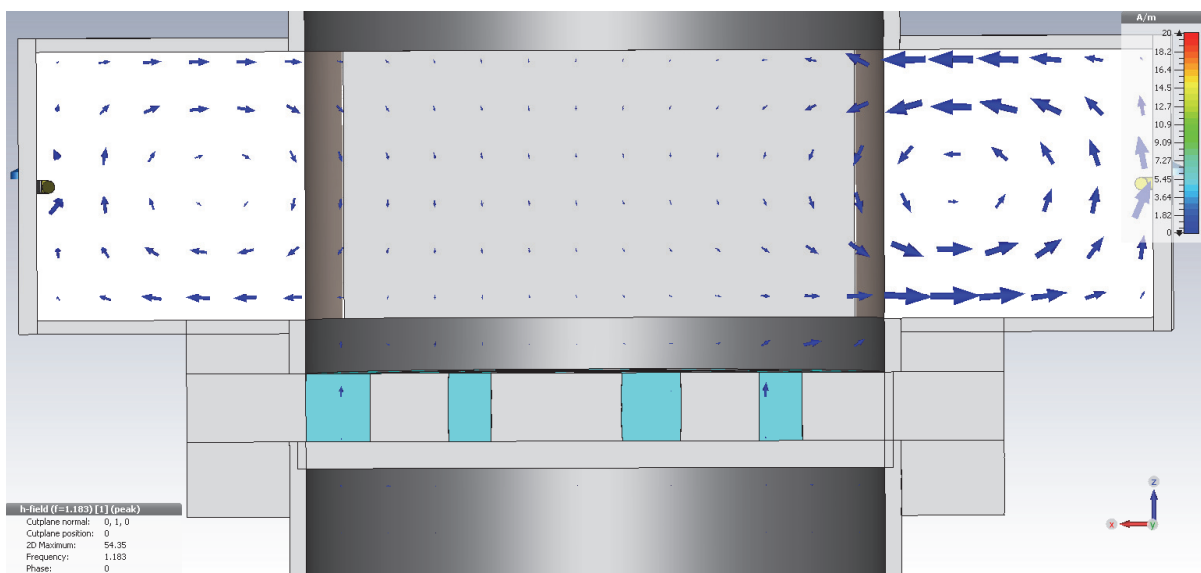
Fig. 62: Coupling Loop, Magnetic Field @ 1.18GHz
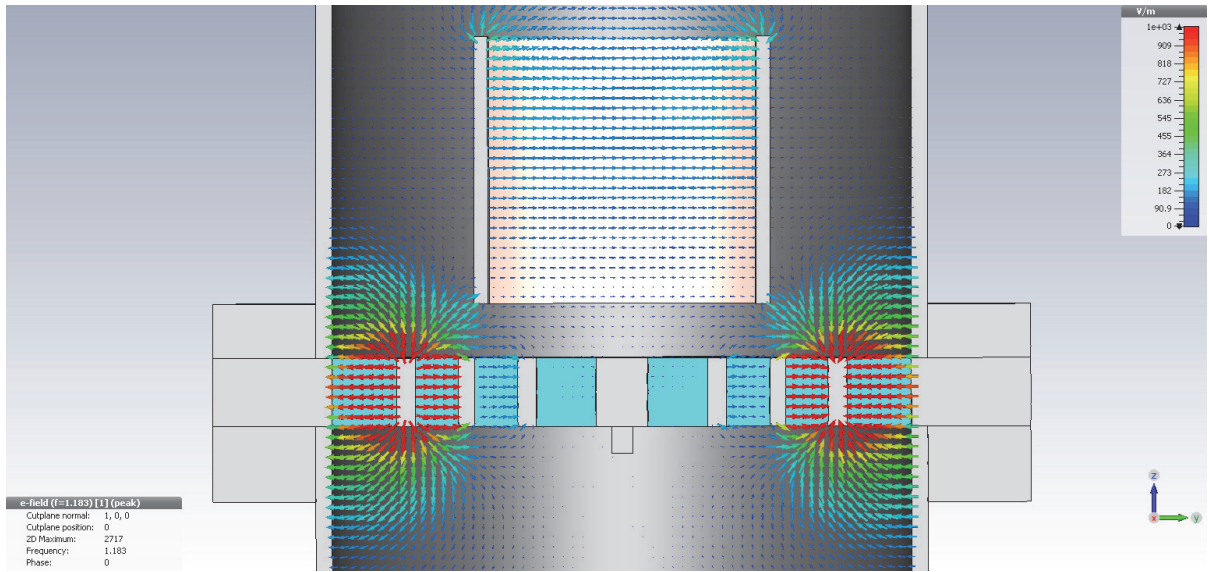
Fig. 63: Coupling Loop, Electric Field @ 1.18GHz
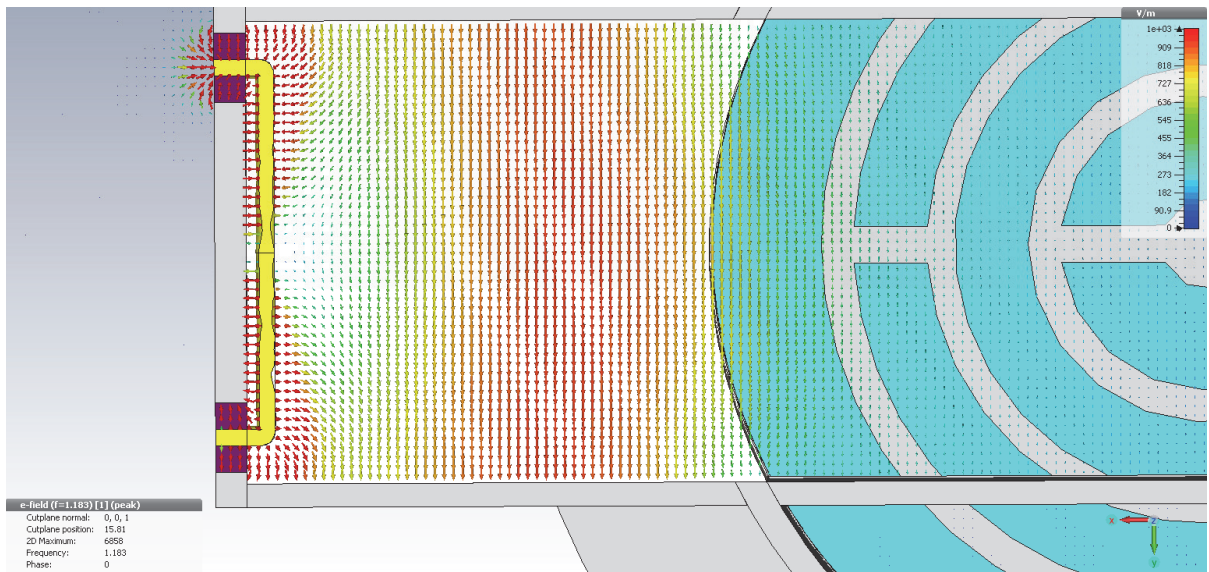
Fig. 64: Coupling Loop, Electric Field Strength in RWG @ 1.18GHz
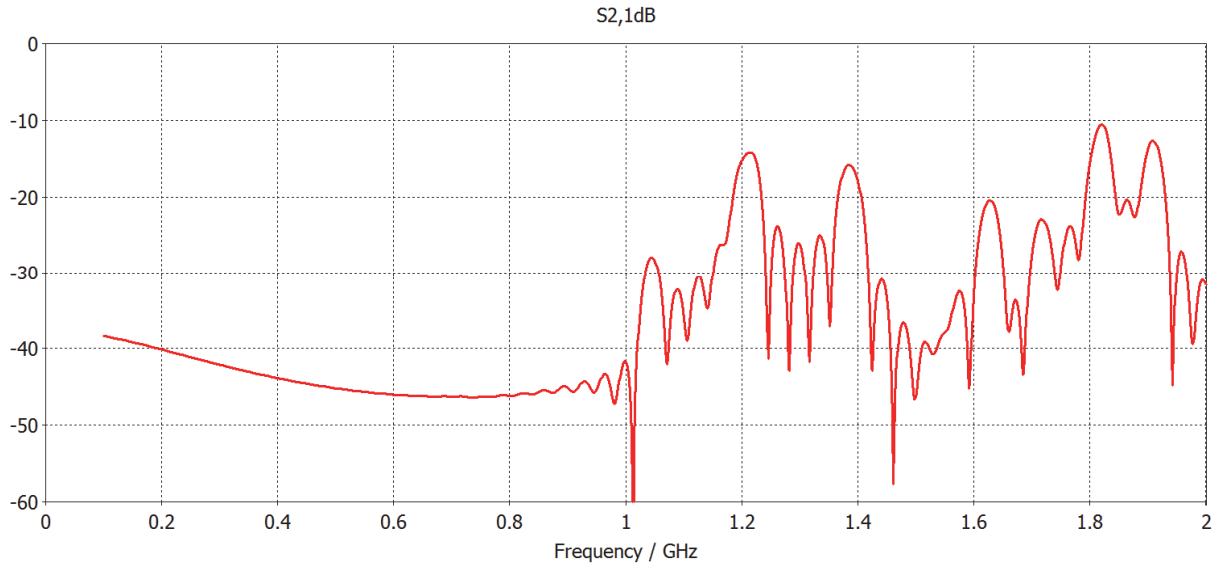
Fig. 65: Coupling Loop |S21| Response, Initial Model @ Steam ε_r =1.00785
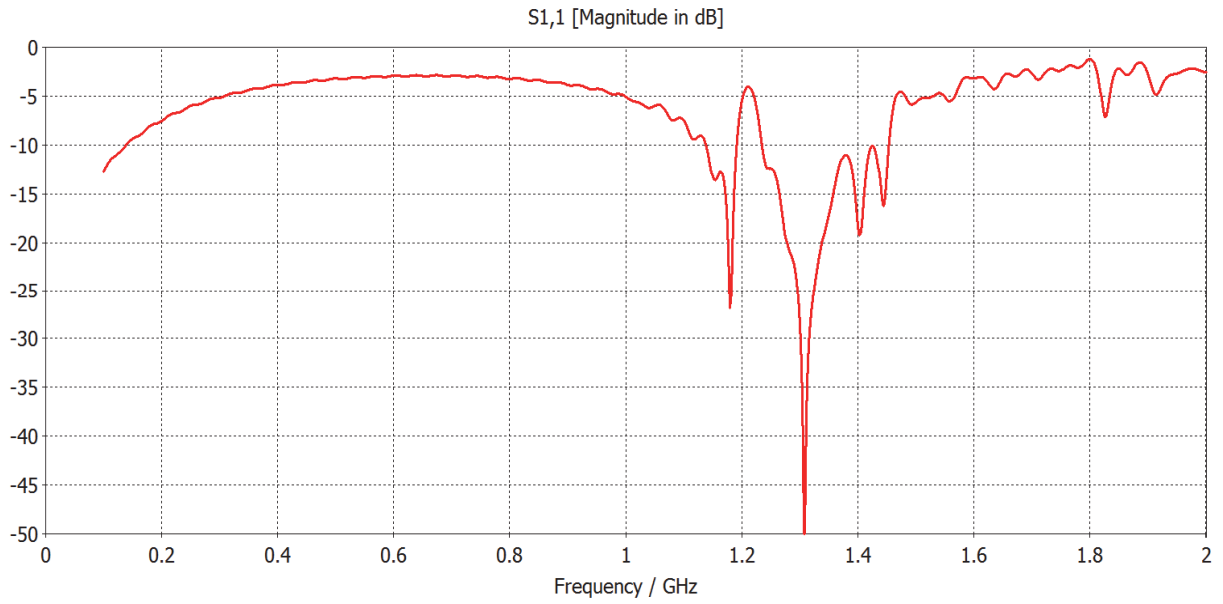
Fig. 66: |S11| Coupling Loop, Initial Model @ Steam ε_r =1.00785

To verify that the design of the coupling loop was causing inadequate excitation

magnetic fields in the RWG and therefore resulting in inferior coupling from the PPWG to

the CSRR, the coupling loops height and length were modified. The characteristic impedance of the coaxial cable was set back to 50 Ω. The loop length was varied in steps of 10mm from 20mm to 40mm. As Fig. 67 shows the length of the line had no impact on increasing coupling to the CSRR. The loop height was swept next from 2mm to 10mm in order to increase the characteristic impedance of the coupling loop. Fig. 68 shows the increase in magnitude of S21 with increasing loop height. Increased loop distance improved the transmission between ports. The increase in S21 can be explained by the position of the coupling loop able to excite the magnetic field of the TE_{10} at a maximum field point. Thus a loop located in the center of the magnetic field of the TE_{10} mode should excite a magnetic field with the highest intensity.
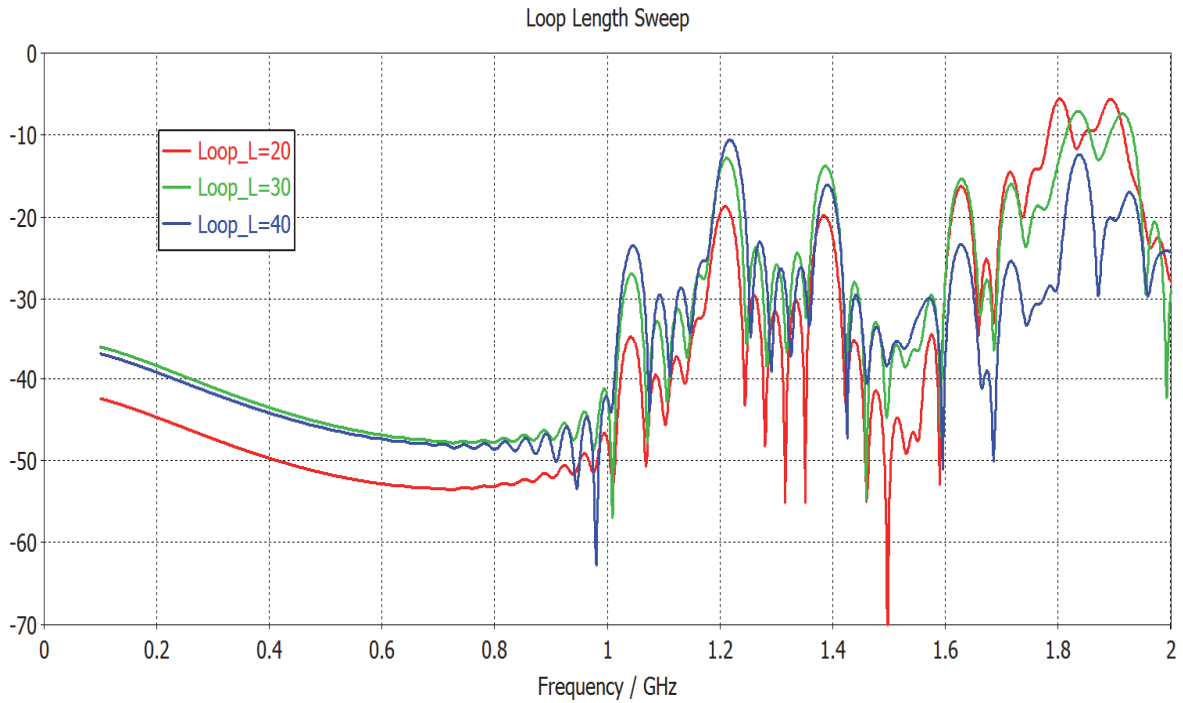
Fig. 67: |S21| Coupling Loop Length Sweep
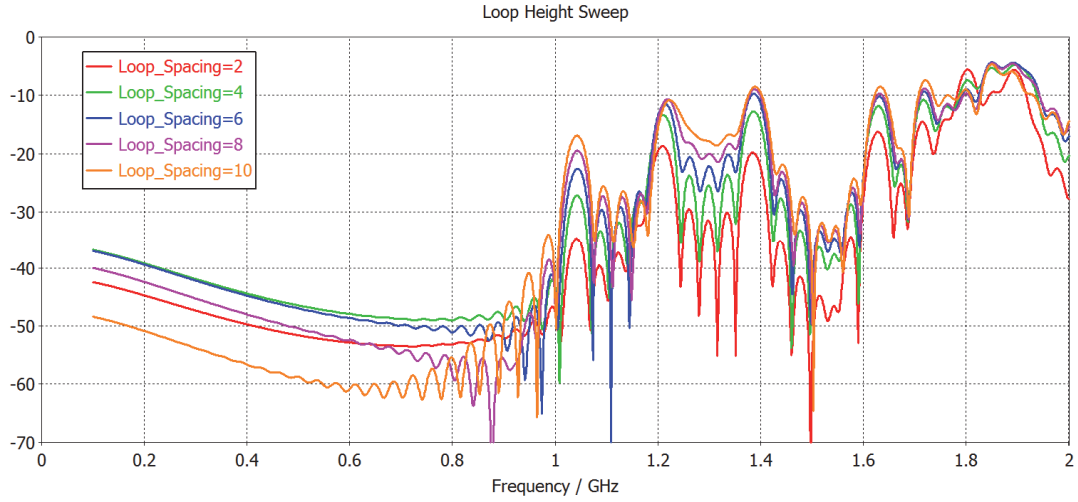
Fig. 68: |S21| Coupling Loop Height Sweep

The simulated CSRR was still not resonating. A final simulation was performed setting the spacing to 15mm which located the coupling loop almost at the center of the RWG. The loop length was also set to 40mm as it too produced a maximal transmission from the line lengths. The 10mm CSRR to PPWG waveguide spacing proves advantageous as the electric fields can achieve a very high intensity between the CSRR and PPWG due to the short distance, though this does not appear to assist in the rings in resonating.
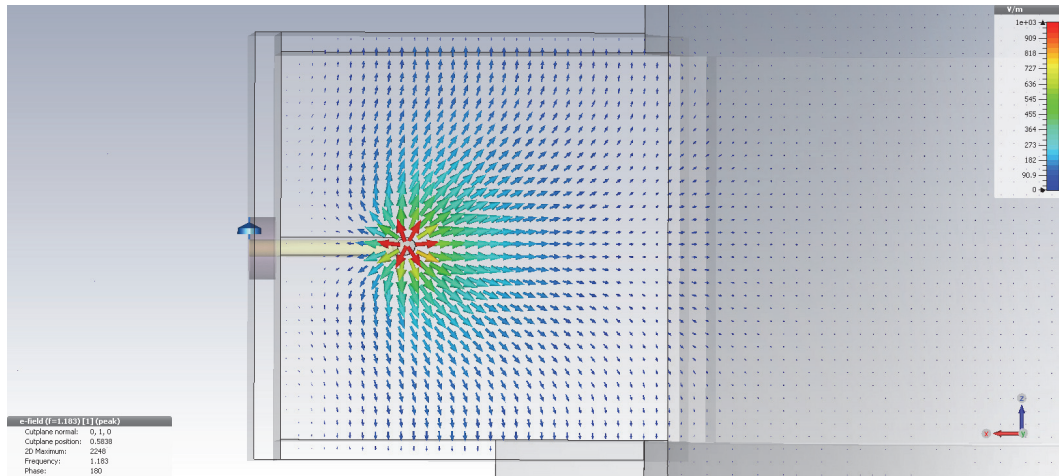
Fig. 69: Electric Field, 15mm Coupling Loop Spacing
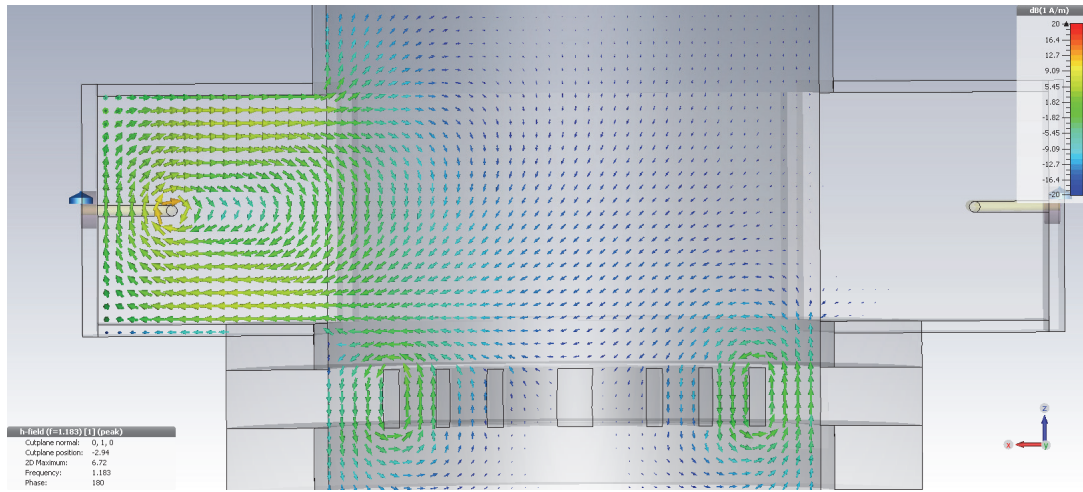
Fig. 70: Magnetic Field, 15mm Coupling Loop Spacing
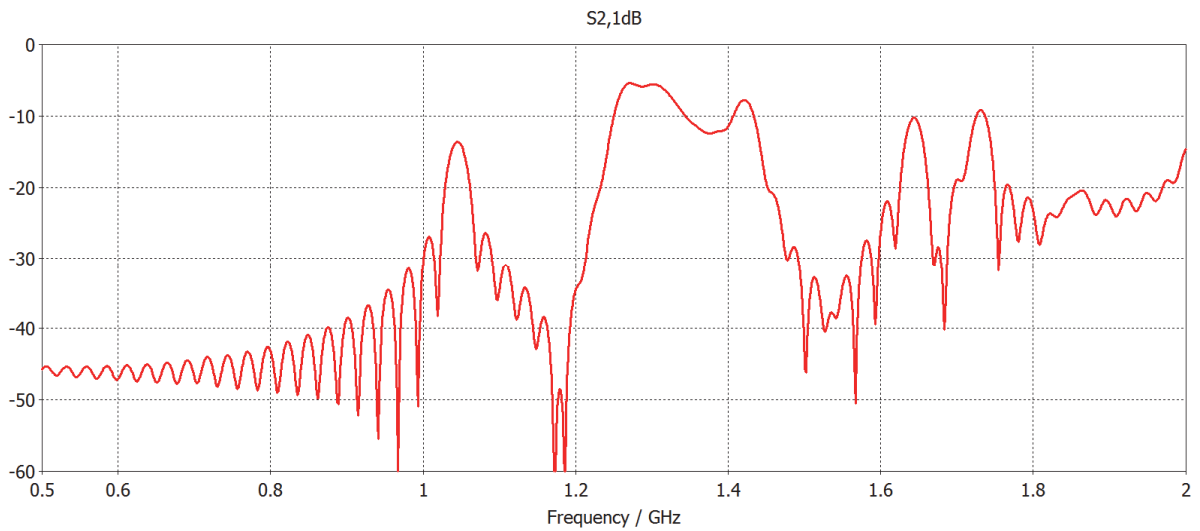
Fig. 71: |S21| 15mm Coupling Loop Spacing

The magnetic field has strong field strength and is correctly oriented for TE_{10} wave

propagation in the RWG, but the electric field is not able to orientate in the y-axis due to the

loop's presence. The coupling loop causes a radial electric field distribution at the center of

the RWG because the electric fields must be perpendicular to the coupling loop surface. The

electric field is therefore unable to properly orient to allow for TE$_{10}$ wave propagation. The electric field attenuates rapidly as the TE$_1$ mode electric field polarizes in the dimension of the PPWG governed by a cutoff frequency at 3GHz. The fields therefore are unable to propagate across the pipe, excite the second coupling loop, or couple to the CSRR. The S21 response of the 15mm spacing is shown in Fig. 71.

4.3.2 Waveguide Probe

A coaxial to waveguide probe was tried as the next RWG excitation structure. The probe is essentially an impedance transformer between the coaxial cable and the waveguide. The probe location in the RWG is important as the distance from the probe to the back wall of the RWG. Locating the probe in the center of the RWG at the point of maximal electric field solves the lateral position problem, however the probe distance to back wall was more complicated.

The characteristic impedance of the waveguide therefore plays an important role in the dimensions and back wall distance of the probe. The first design fixation was the probe itself, available for use in laboratory supplies were extended-dielectric panel mount SMA connectors. The typical flange mountable 50Ω SMA connector with extended dielectric has the dimensions as shown in Fig. 72. This limits the maximum length of the probe to 17.9mm minus the waveguide wall thickness and sets the copper probe diameter at 1.3mm. The Teflon insulation was removed along the length of copper conductor exposed in the waveguide to not lower the cross-sectional effective permittivity and not permit additional wave modes to exist in the RWG.
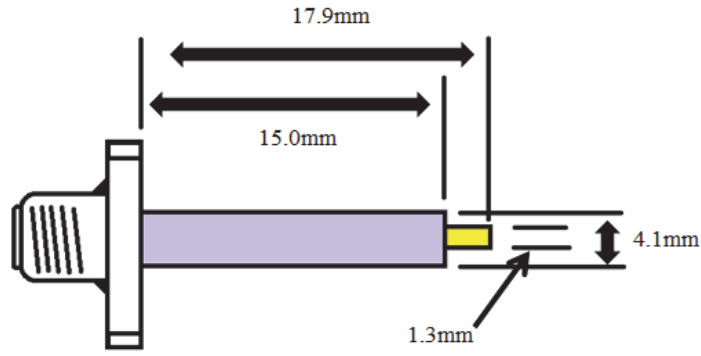
Fig. 72: Typical Extended Insulation Flange Mount SMA Dimensions
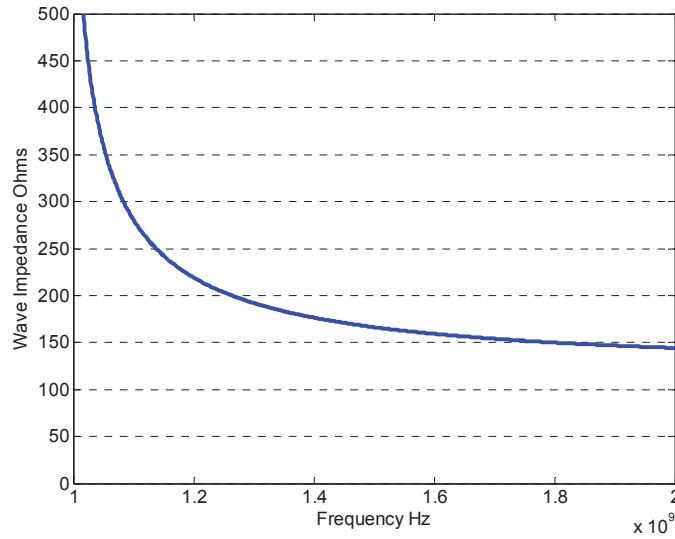
Fig. 73: Wave Impedance of a 1GHz Cutoff RWG Dielectrically Loaded with ε_r =9

The next step was to determine the wave impedance in the RWG. The impedance of a 50mm square wave with a cutoff of 1GHz is shown in Fig. 73. The impedance seen by a waveguide probe will be dependent upon the ratio of the RWG dimensions and probe position as discussed in [21]. Ideally, the cutoff frequency of the RWG should be lowered to allow for a decrease in wave impedance of the RWG when coupling to the CSRR. Thus, the permittivity of the alumina dielectrically loading the RWG was increased to 9.4 resulting in a cutoff of 978MHz.

The distance between the back wall of the RWG and the probe is typically chosen to be a quarter-wave length in order to cancel out reflections caused by the conducting wall at the probe. This happens as a result of the superposition between two signals of the same frequency that are 180^0 out of phase after traveling a quarter-wave length path then reflected. A quarter-wave length separation serves as a good initial point for probe placement with final placement dependent on the parasitic inductance and capacitance of the copper probe. A center frequency of 1.25GHz in 9.4 permittivity alumina places the quarter-wave length at 19.6mm. Typically, tuning screws are employed to tune the impedance of the waveguide seen by the probe. A tuning screw approach for maximizing power transfer is not applicable for use in the SQS, so simulation must be relied upon to find the optimum back short distance and probe length given the waveguide dimensions.

One of the problems with using a dielectrically loaded RWG to PPWG coupling structure is the impedance mismatch seen at the boundary when the RWG transitions to PPWG. The impedance of the RWG is roughly governed by (13) when RWG dimensions are accounted for [22]. Use equally dimensioned RWG eliminates the dimensional ratio and leaves the impedance as a function of only the dielectric and the frequency.

$$Z_{RWG,TE10} = \frac{600}{\sqrt{\varepsilon_r}} \cdot \frac{b}{a} \cdot \frac{1}{\sqrt{1 - \left(\frac{f_c}{f}\right)^2}} \tag{13}$$
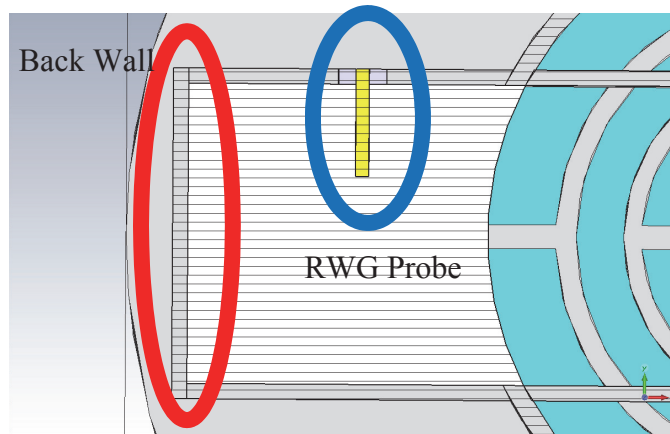
Fig. 74: RWG Probe and Back Wall

A new model was developed using the SMA panel mount connector embedded in the wall of the rectangular waveguide. The model modified slightly from the coupling loop simulation to account for the thickness of an ANSI B16.5 class 150 lb. loose or slip flange. The typical thickness of 4" nominal pipe size B16.5 class 150 is 0.940" [23]. Thus the entire PPWG must also shift away from the CSRR by 0.940" or have a custom flange design, which was not financially practical. Ideally, the downstream edge of the PPWG should be as close to the CSRR as possible to increase the electric field intensity of the fringing electric fields. In practice, the thickness of the flange used will determine the minimum spacing the spacing between the edge of the PPWG and the CSRR thereby determining the intensity of the fringed electric field. The edge PPWG, therefore, will always be placed at the minimum distance which corresponds to flange thickness in the models. Aside from the RWG excitation and the increased PPWG to CSRR distance the simulation remained unchanged from the coupling loop model.

The y-axis oriented RWG probe proved capable of properly exciting the CSRR The reflection coefficient was still quite poor. The use of a quarter-wave length for the probe distance was observed not to be optimal. One of the benefits of the the use of a RWG to

PPWG coupling structure is water along the pipe wall and the alumina helps match the characteristic impedances of the PPWG to the RWG by increasing the impedance of the PPWG. Thus, at 100% SQ the worst possible S11 will be measured for the SQS.

The probe was also to demonstrate in an un-tuned manner, the ability to clearly distinguish steam shifts between 30% and 100% quality. The optimizing of the probe position with respect to the back wall of the RWG was still a model concern. The rest of the parameters would be finalized in the alpha model design before finding tuning the probe location for the lowest possible S11.
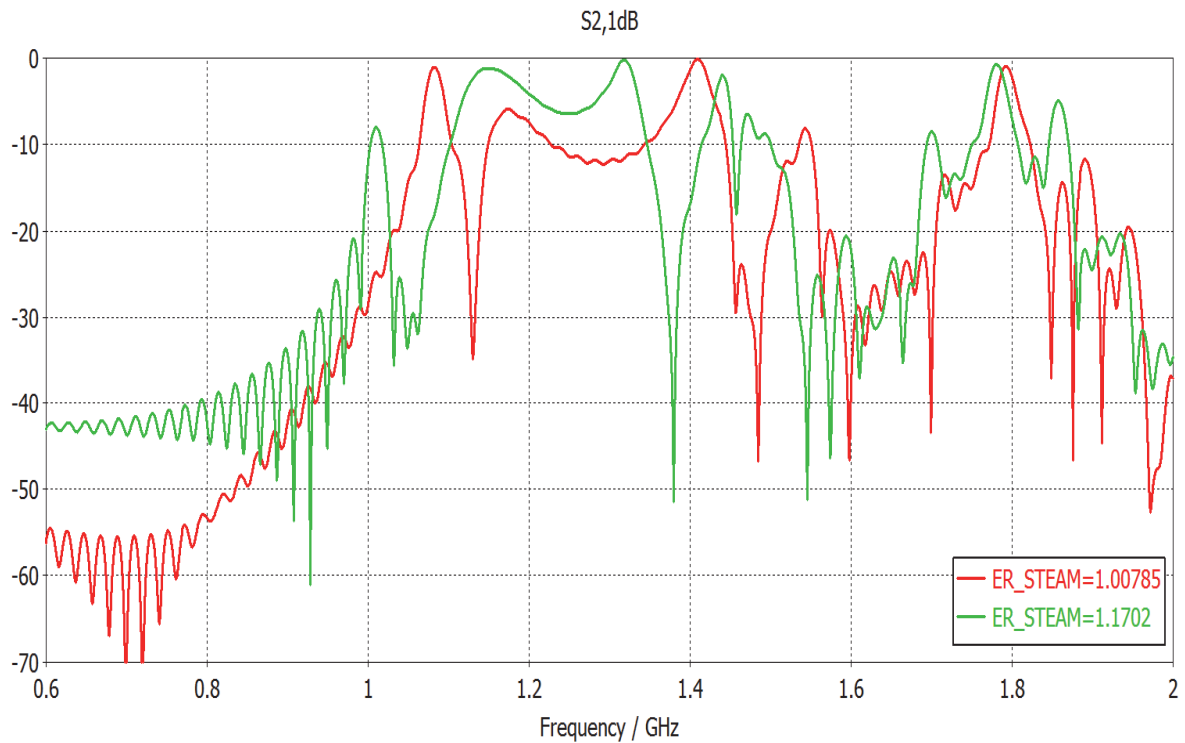
Fig. 75: |S21| RWG Probe Steam Sweep
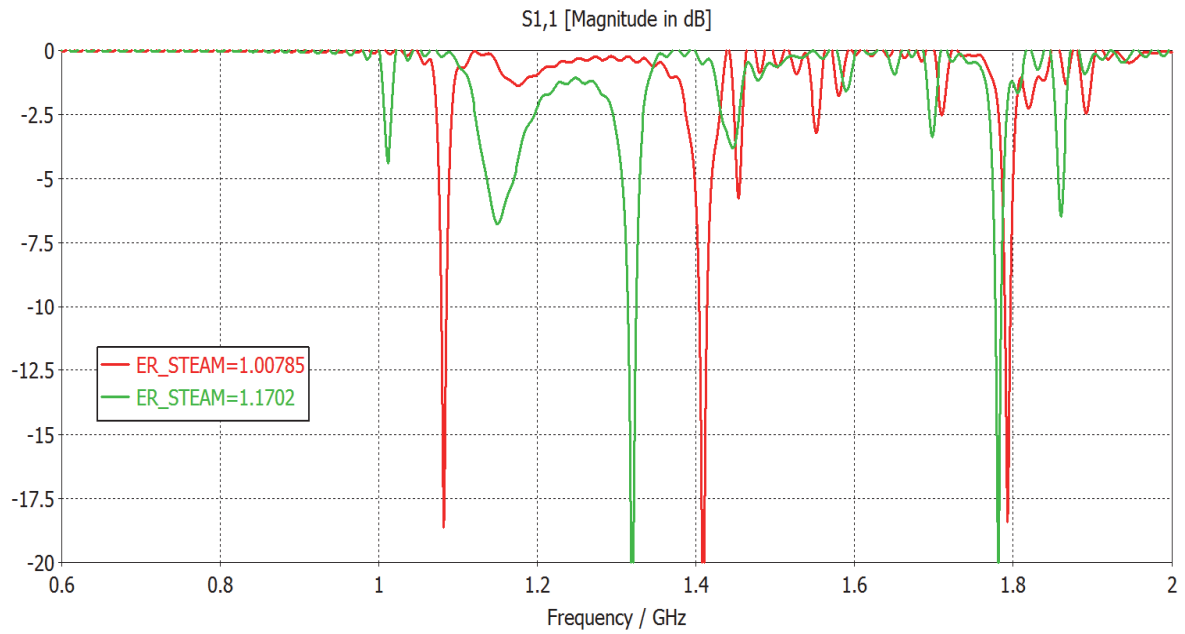
Fig. 76: |S11| RWG Probe at back short distance λ/4 @ 1.2GHz
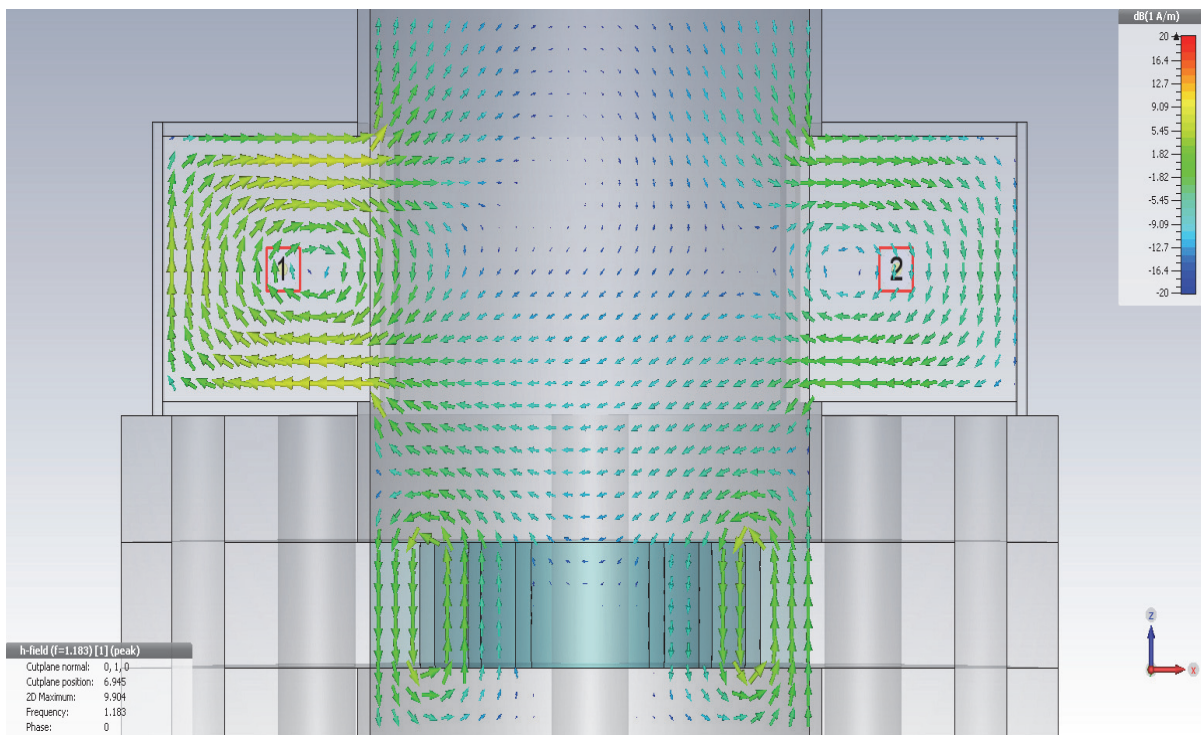
Fig. 77: Coaxial Probe, Magnetic Field @ 1.18GHz
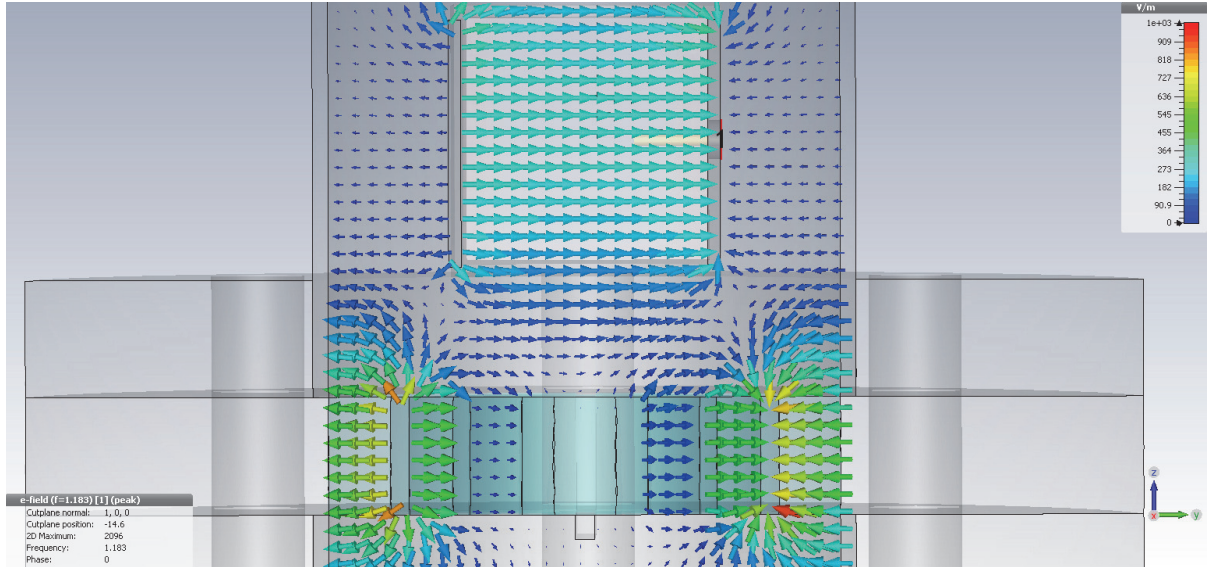
Fig. 78: Coaxial Probe, Magnetic Field @ 1.18GHz

The improved performance of the coaxial probe compared to the coupling loop can be attributed to the manner in which the structures excite the RWG. The coupling loop produces strong magnetic fields caused by current flow through the loop. The coaxial probe behaves most similarly to a monopole antenna exciting the RWG with strong electric fields. The CSRR can be excited using either a parallel magnetic field or a perpendicular electric field. The strength of the fields coupled to the CSRR appears to be the differing factor in coupling loop verses probe excitation. The strength of the fringed electric fields from the PPWG that couple to the CSRR and the parallel magnetic fields looping around the CSRR are stronger when the RWG is excited via a probe.

4.4 Alpha Design Ceramic Stops and RWG Dimension Optimization

The cost associated with having the alumina loading the RWGs laser welded to the inside of the RWGs was outside the budget. A solution was developed in order to secure the

alumina in the waveguide by constricting the RWG opening into the pipe in a non-critical dimension.

The first alumina securing solution developed constricted the RWG opening into the steam pipe, preventing the alumina from falling into the pipe when steam pressure dropped. The ceramic stops were square bar stock edge welded to the inside of the RWG at the transition between the RWG and the PPWG. The ceramic stop placements are shown circled in Fig. 79. The ceramic stops should be as small as possible to minimize the disturbance of the electric field inside the RWG. A 3.2mm (1/8") square bar stock was selected as it is the smallest commercially available bar stock dimension. The use of ceramic tabs reduced the dimension of the rectangular waveguide but not in the dimension that governed that does not the cutoff frequency of the TE_{10} mode. The constriction did however effect the impedance of the RWG of the by adding a field perturbing conductor in the direction of wave propagation which additionally caused wave reflections back to the probe.
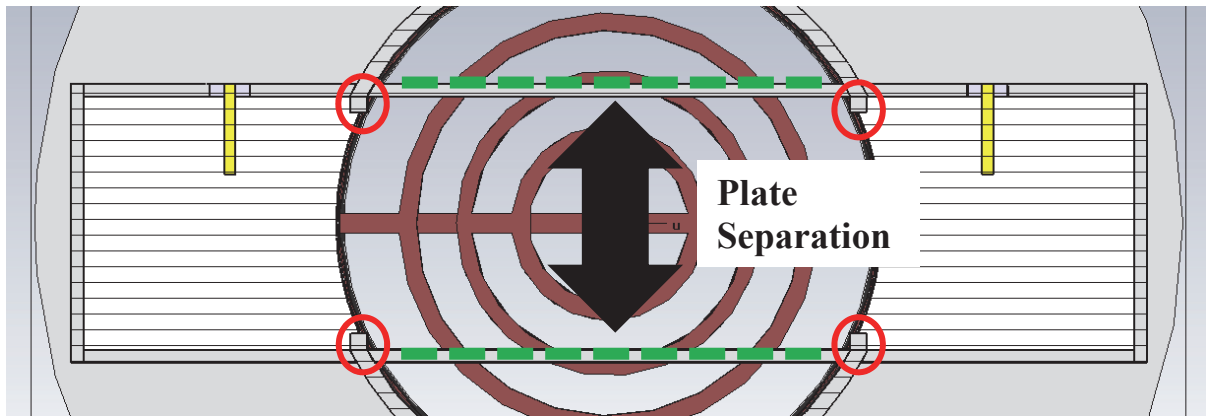
Fig. 79: Ceramic Stoppers and Plate Separation Dimension

A parameter sweep was performed on the steam permittivity and RWG/PPWG dimensions. The PPWG plate width which is equal to the waveguide width was held constant

at 50mm, as it determines the cutoff frequency of the TE_{10} mode in the RWG. The separation between the waveguide plates was varied from 30mm to 50mm in 5mm increments. Each plate separation distance simulation also was re-simulated with three steam permittivity values: 1.00785, 1.08903, and 1.1702, which respectively correspond to 100%, 46%, and 30% steam quality at 175^0C and 1.03Mpa.
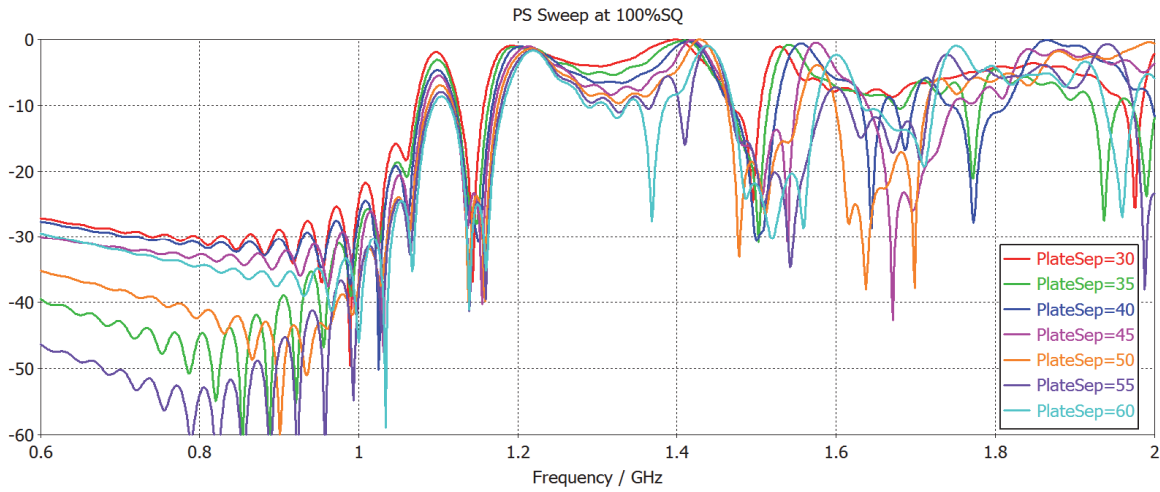
Fig. 80: |S21| Response with Plate Separation @ 100%SQ
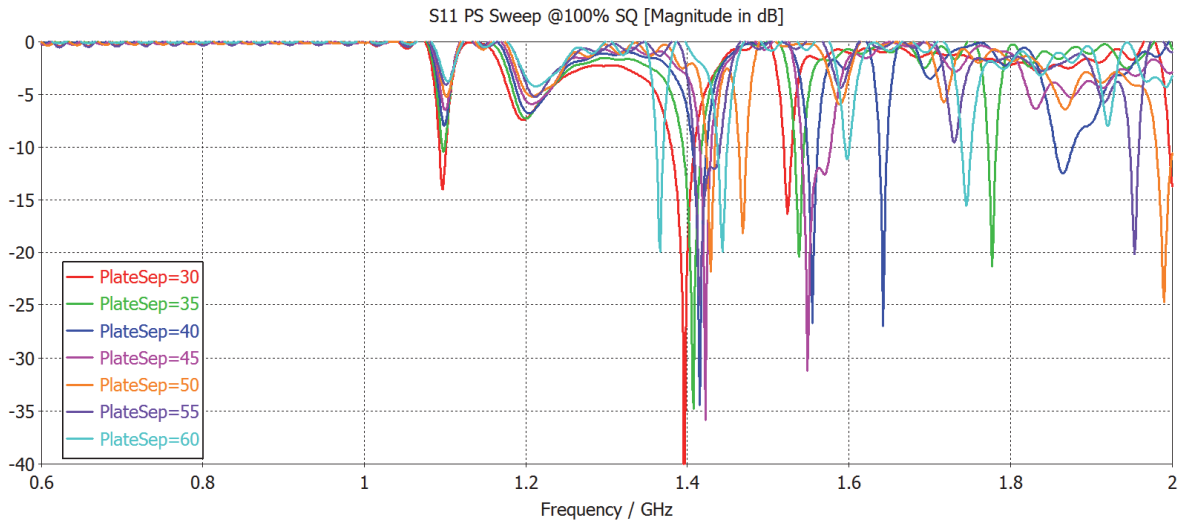
Fig. 81:|S11| Response with Plate Separation @ 100%SQ

The simulation results in figures Fig. 80 and Fig. 81 show the frequency response as a function of the PPWG plate separation. This separation affects the reflection coefficient of the excitation probe by changing the impedance of the RWG and the field coupling between the CSRR and the PPWG by varying the ring area beneath the PPWG plates. The results indicate that the best coupling occurs when the plate separation is between 30 and 40 millimeters. The absolute best plate separation proved to be the 30mm. The 30mm plate separation had the lowest overall S11 at 100% SQ and only improved as steam permittivity increased by reducing the impedance mismatch at the RWG and PPWG transition. The 30mm of separation can also be seen to have the lowest S11 values between 1.2 and 1.4GHz and the highest quality transmission nulls from all the simulated values. A 30mm plate separation also was able to couple energy into the 2nd ring of the CSRR allowing one more resonance to appear, but at above cutoff of the pipe at 1.73GHz when filled with 100% quality steam. The 30mm plate separation appears to position the edges of the PPWG over a maximal amount of ring surface area allowing for strong coupling with the electric field.
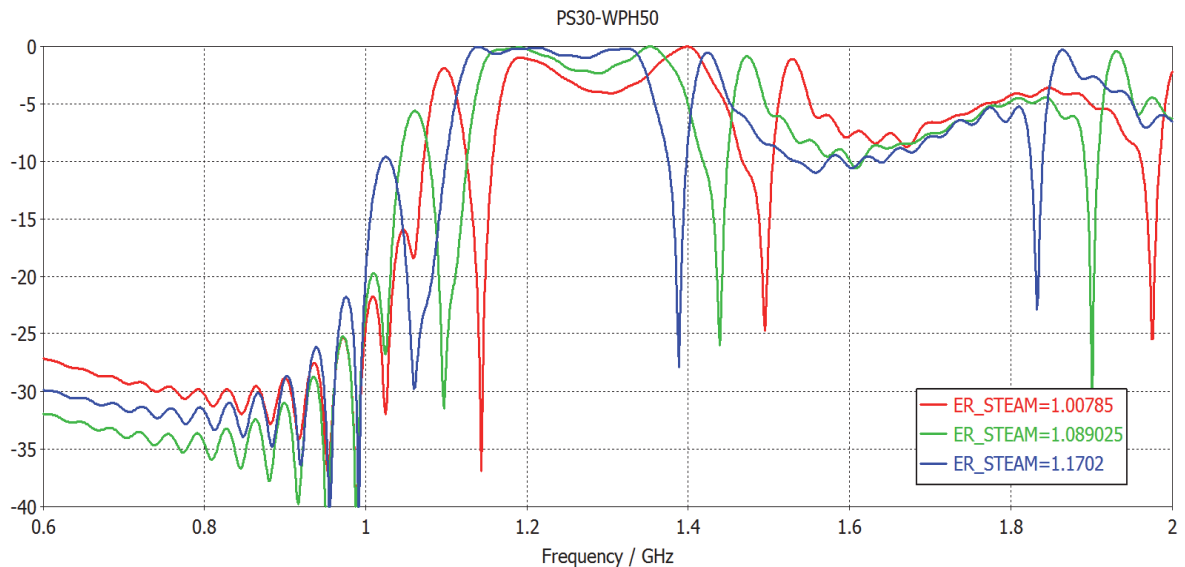
Fig. 82: |S21| PPWG Plate Separation of 30mm
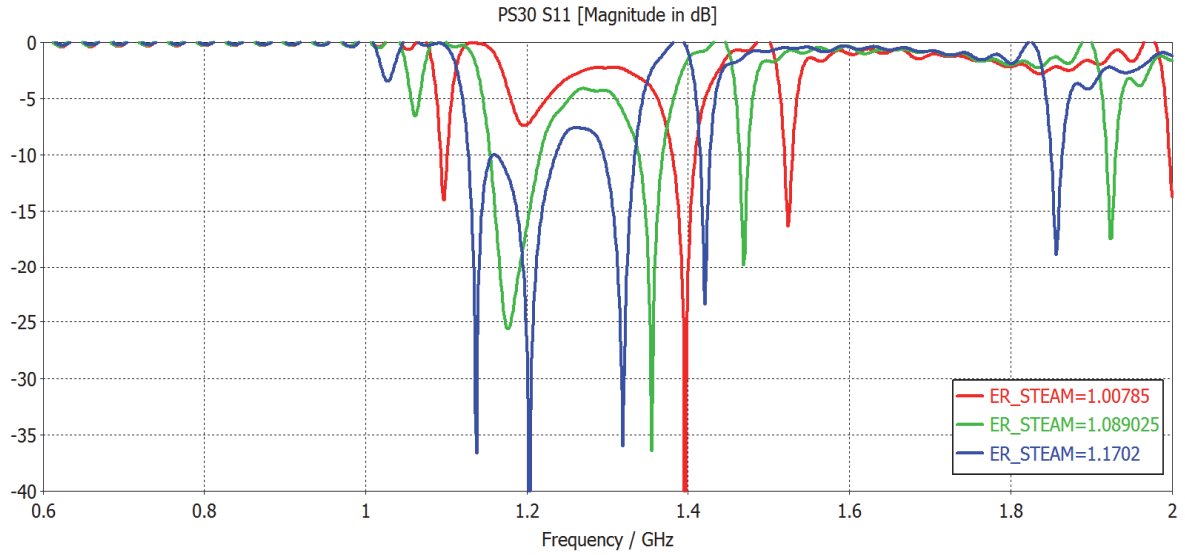
Fig. 83:|S11| PPWG Plate Separation of 30mm

The S21 and S11 results show a well performing design at 30mm plate separation across a range of steam permittivities. The S11 reflection coefficient only decreases as the impedance of the PPWG is lowered with increasing steam permittivity shown in Fig. 83. While the S21 of the 30 plate separation model shows good feature sensitivity to steam permittivity changes as shown in Fig. 82.

4.5 Final Alpha Unit

Work began on producing mechanical drawings for manufacture, but after a consultation with Mr. Orr, the Baylor Engineering Machinist, it was determined that the ceramic stoppers were beyond ordinary construction and welding. Thus while the ceramic stops did work to hold the ceramic with minimal intrusion into the waveguide, their small size prohibited welding. Since the ceramic stops so were unable to be reliably affixed inside the RWG they were removed from the design. The new solution to secure the alumina ceramic was to add tabs to the ceramic near the end of RWG away from the pipe. Notches

85

would be cut into the RWG the smaller length wall and the ceramic would slide into place. The inside of the RWG would be shaved 1mm for 12.7mm to enabling the alumina to slide in. The end cap would then be attached via welding providing a permanent seal.
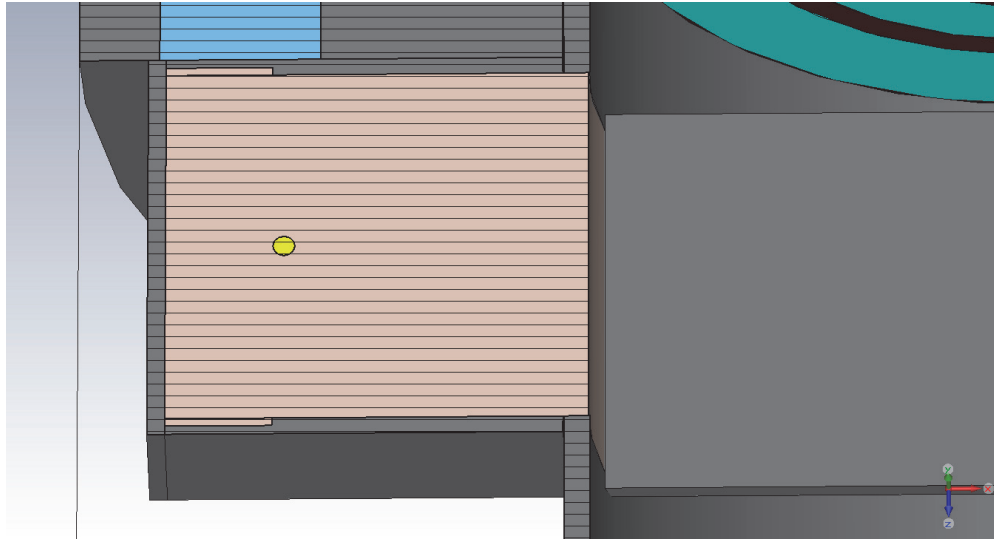
Fig. 84: Tabbed Alumina with RWG slots

The alpha unit's steam piping was 4-inch schedule-10 ASTM sprinkler pipe, donated by Pioneer Steel and Pipe Company located in Waco, Texas. The schedule-10 piping had a nominal OD of 114.3mm and a nominal wall thickness of 3.048mm with 1mm measured tolerances. This gave an effective minimum ID of 108.2mm for the piping. While not listed on the pipe, it is a mild grade carbon steel alloy, the most probably alloy is ASTM A53 steel.

Another design change made for manufacturability was the purchase of structural steel tubing to construct the RWG and PPWG instead of welding four individual plates together. Commercial mechanical/structural tubing is sold using outer dimensions at a specified wall thickness. The closest metric tubing size for a 30mm by 50mm inter dimension RWG is rectangular tubing in 60mm by 40mm with a wall thickness of 4mm. The design of the waveguides is such that over dimensioning a part is acceptable while under dimensioning

would be harmful to performance as cutoff frequencies for the RWG would shift up. Unfortunately, no US based suppliers carry 60-40-4mm tubing and acquiring the tubing from Europe was cost prohibitive. The imperial size tubing with the closest dimensions to the 60mm by 40mm metric tubing is 2-inch by 1.25-inch structural tubing with 14-gauge wall thickness. The 2-inch by 1.25-inch tubing would roughly have inner dimensions of 46.8mm by 28.5mm with a wall thickness 2mm with a 0.2mm tolerance. The 2-inch by 1.25-inch, 14-gauge tubing was made from ASME-1020 steel and purchased from discountsteel.com.

The smaller dimensional tubing required a higher permittivity than 9.4 using 96% pure alumina. The dielectric loading the RWG was then changed to toAD-995, a 99.5% pure alumina from Coorstek which had a permittivity of 9.7 [15]. The change brought the cutoff frequency of the smaller 2"-by-1.25" RWG up to 1.02GHz up from 960MHz.

The orifice plate containing the CSRR was modeled as AL-6061 at 23.8125mm thick. The CSRR had the standard bolt size and hole arrangement for a class 125/150 ASME pipe flange as per the B16.5 standard [24]. The orifice plate should be constructed from SS-316 or SS-304, but material and machine costs were above the budget.

The alpha SQS unit was modelled in CST using the above component changes. The ceramic stops were removed and the ceramic tabs added. The model dimensions were change to match the dimensions of the schedule-10 piping, 2-inch by 1.25-inch rectangular tubing, and 23.8mm thick orifice plate. The alumina was updated to the AD-995 material with permittivity 9.7.

The coaxial probe's distance from the back wall, or end cap, still required tuning thus the simulation was first run as a parameter sweep varying the back wall distance by controlling the x-coordinate of the probe center. The back wall of the ceramic was set at the

104mm mark the probe position was swept from the 70mm mark to the 90mm mark on the x-axis. This gave an effective back short distance from the probe to the end cap of 34mm to 14mm. Having the back short distance as close to a quarter-wave length at the design frequency allows for the reflected wave to cancel with itself at the probe preventing wave propagation back up the coaxial cable that appears as a higher S11.Using (14) these distances correspond the quarter-wave lengths from 700MHz to 1.72GHz of waves traveling in a 28.5mm wide RWG with a dielectric permittivity of 9.7 [25].

$$\lambda_{guide} = \frac{u_p}{f} \cdot \frac{1}{\sqrt{1 - \left(\frac{u_p}{2 \cdot RWG_{Width} \cdot f}\right)}} = \frac{9.632 \cdot 10^7}{f \cdot \sqrt{1 - \left(\frac{9.632 \cdot 10^7}{57 \cdot 10^{-3} \cdot f}\right)}} \tag{14}$$

The early designs of the coaxial probe location were performed under the assumption that the only wave reflection that occurs in the RWG was due to the RWG back wall. This is not entirely true, while the magnitude of the reflection will be the largest at the back wall, there is another important reflection that occurs at the boundary between the RWG and the PPWG and should be considered for optimal probe positioning. The boundary reflection between the RWG and the PPWG is due to the impedance mismatch of the two waveguides. The RWG has a very Z_0 compared to the Z_0 of the PPWG immediately above the cutoff frequency of the RWG, but decreases to a Z_{RWG} roughly a third of the Z_{PPWG}. By precisely choosing the lengths between the probe to back wall and probe to PPWG to be slightly different a wider bandwidth S11 match can be achieved for the coaxial probe can be achieved. The matching for broad bandwidth with this method does raise the minimum achievable S11 value for the SQS system.
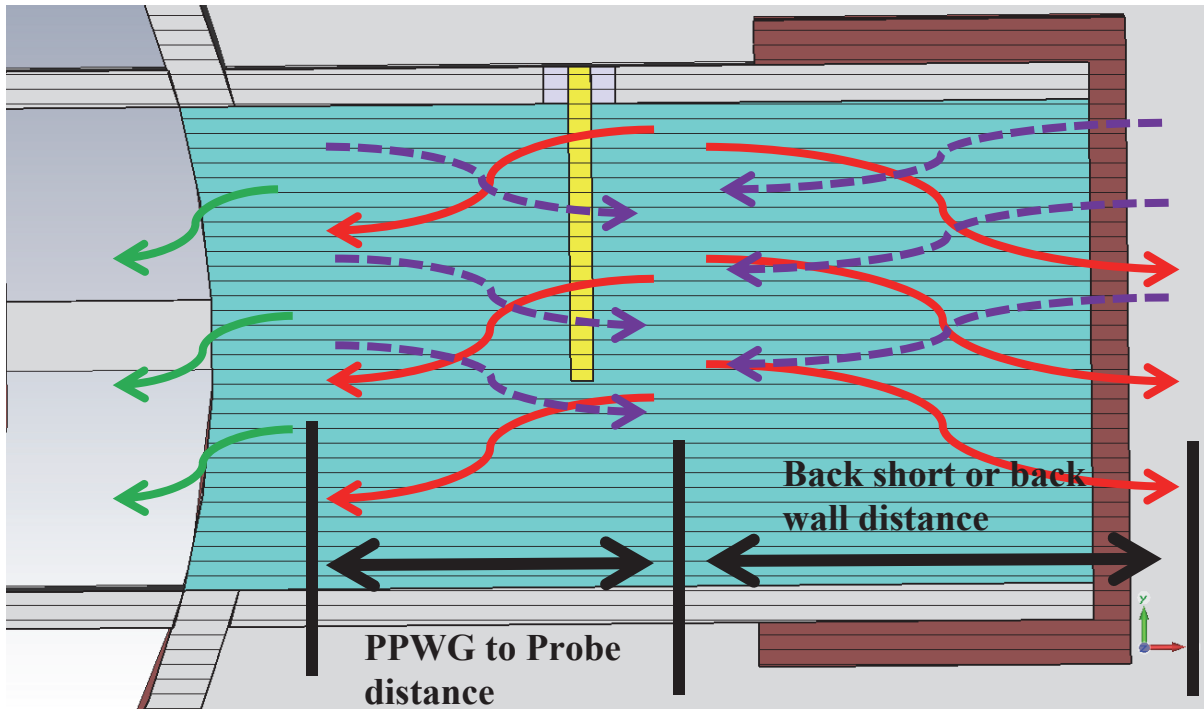
Fig. 85: RWG Principle Reflections Diagram

The results from the sweep show in that the shorter back short distances (< 20mm) tend to perform better in the band between 1.1GHz and 1.4GHz but have shallower nulls than the longer distances. A compromise of 29mm gap length was chosen as the design distance. Figures Fig. 86 and Fig. 87 have the 29mm back short distance response highlighted compared to the other simulated distances. The back wall is located at 104 mm, for reference. This also the cause of the decreasing S11 magnitude with increasing permittivity seen in Fig. 83.The higher liquid steam content decreases the characteristic impedance of the PPWG reducing the magnitude of the PPWG and RWG boundary reflection. Fig. 85 shows the reflections in the RWG. The red traces signify waves incident at the boundaries, purple the signal reflected and the green represents signal transmitted from the RWG to the PPWG.

The distance between the probe and the RWG to PPWG boundary is not uniform. It varies by +- 2mm across the opening of the RWG. This distance variation will increase the

range of frequencies which see the PPWG to probe distance as a quarter-wave length. The
increased frequency range translates to an overall reduced reflection coefficient caused by the
quarter-wave length frequency match of PPWG to probe distance.
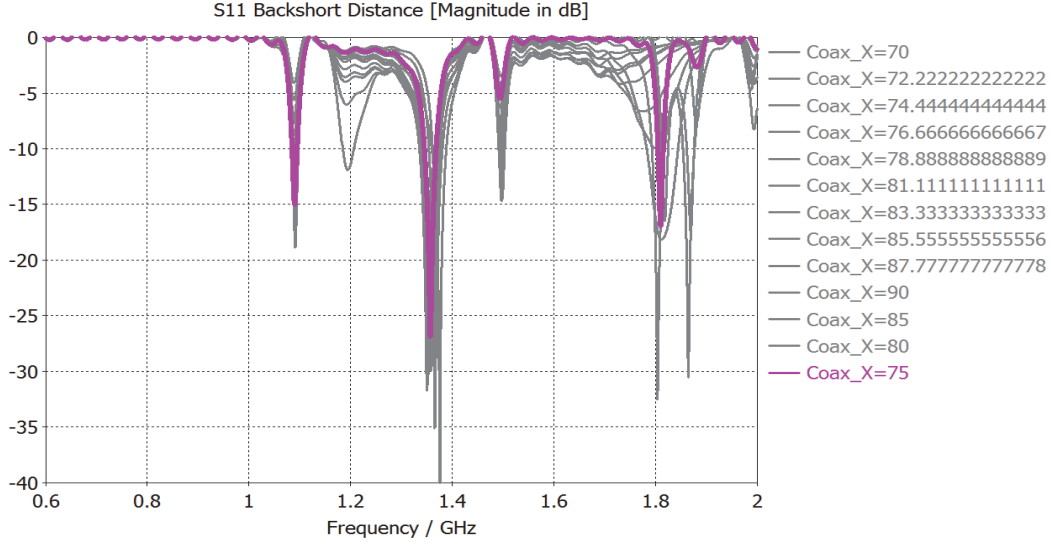
Fig. 86: |S11| Back short distance response for ε_r=1.00785, 29mm Back short highlighted
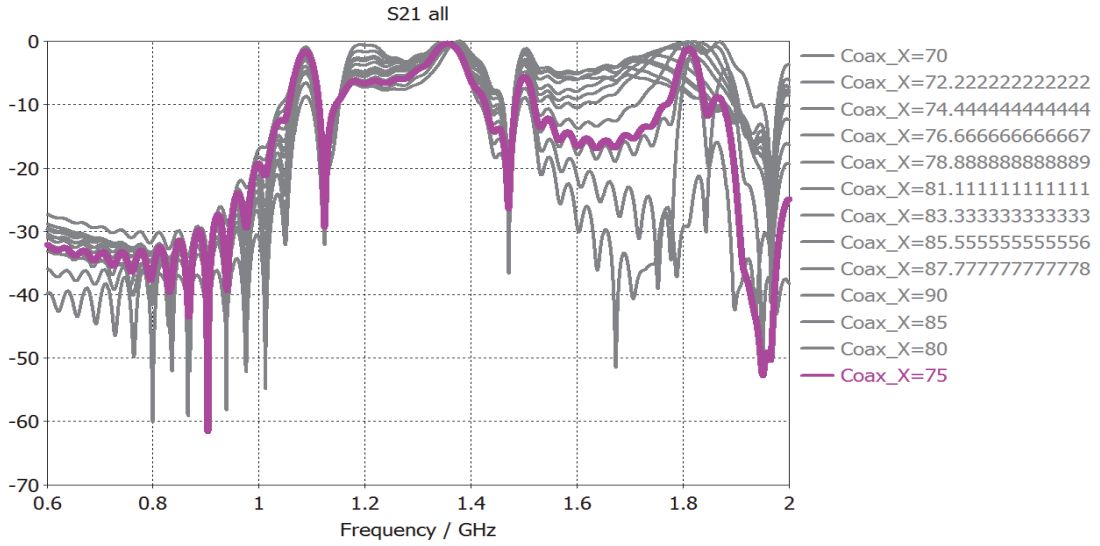
Fig. 87: |S21| Back short distance response for ε_r=1.00785, 29mm Back-Short highlighted

90

During the procurement of materials for construction, difficulties were had with acquiring alumina. The difficulties arose from the extremely high cost of single unit prototyping pieces of custom formed alumina. The project had to move away from alumina at this time and find a less expensive alternative that could be molded and formed in-house. A two-part dielectric cement made by Emerson and Cuming Microwave Products Inc. was determined to be the best option [26]. The dielectric cement mixture is marketed under the name Hi-K cement and is available in dielectric constants ranging from 3 to 15. The principle material in Hi-K cement is titanium dioxide which possesses a very low loss tangent and high bond strength. The dielectric constant for the Hi-K cement was chosen to be 10 and a 2.2kg kit was ordered to replace the alumina parts.

The final CST model with the RWG dielectric as material Hi-K cement with a permittivity of 10 was simulated. The probe back wall distance was kept at 29mm which now corresponded to a quarter-wave length at 820MHz that also resulted in PPWG to probe distance of a minimum of 21mm, which corresponds to a quarter-wave length at 1.13GHz.

4.5.2 Fabrication

The CSRR orifice plate was manufactured using a water jet cutting process by Cen-Tex Sheet Metal Fabricators. The maximum machinable CSRR thickness for the cutting process was 12.7mm. The CSRR material was chosen to be AL6061-T6 for budgetary purposes as steel their manufacturing capabilities limited the maximum cut-able thickness for steel at 9.53mm at over double the cost. Additional bolt holes were added for the capability to test different CSRR orientations allowing for rotational increments of 22.5^0.

The rest of the metal fabrication of the SQS was done in the by Orr [27]. The SQS RWG and PPWG structure constituted what was referred to in the appendix mechanical

drawings as the excitation structure. The excitation structure was base was an 8" long section of the 4-inch schedule-10 piping. A 6.35mm thick class 150 bolt hole compatible flange substitute was milled and welded to the end of the pipe. The 2-inch by 1.25-inch rectangular tubing was turned into the PPWG by removing the 1.25-inch sides from the center of the RWG. The 1mm ceramic tab slots in the RWG were too small to be reliably manufactured at 0.1mm tolerance. The location where the RWG ceramic tab slots would have been was instead removed completely. The excitation assembly consisting of the PPWG and RWG was then welded to the pipe. The heat from the welding on the 2mm wall thickness was intensive enough to bow the PPWG plates slightly inward during manufacturing. The bowed plates were manually corrected by hand to the best degree possible.

The RWG end cap was fabricated as a slip cover which would also cover the ceramic tab openings cut into the RWG. The end cap was made from AL-6061 and held firmly in place via six 6-32 hex-head set screws. The bottom flange/pipe assembly was made from ¼-inch steel-1020. The flange was welded to a 102mm long 4-inch schedule-10 sprinkler pipe. The whole bottom flange/pipe assembly was spray pained to prevent corrosion with a black epoxy-resin based paint.
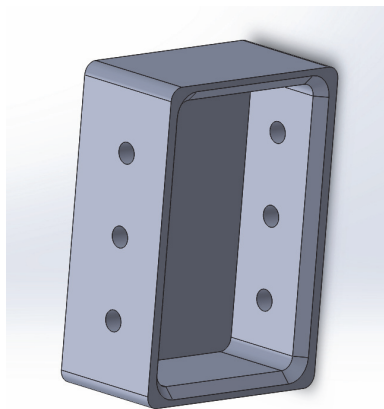
Fig. 88: RWG End Cap with Set Screw Holes

92

The coaxial probes were built from female SMA square flange panel mount connectors with extended insulation. The extended Teflon dielectric was removed from the center conductor except for a 2.1mm strip closest to the flange which would fit inside the RWG wall. The probes were then mounted into a 4.1mm hole drilled 28.9mm from the outside end of the RWG. The probes were secured using M3 machine screws affixing the panel mount connector firmly to the RWG.

Once the RWG probes were attached to the RWG the Hi-K cement was hand-mixed and the waveguide prepared to be filled. The RWG tubing had an internal weld seam which was ground and polished down to a smooth surface. The entire inside of the excitation cavity was polished such that the structure's wall roughness was as low as possible especially in the waveguide cavities. The entire structure was then cleaned and, with the exception of the waveguide cavities, painted with the same thin coat of epoxy-resin spray paint as the bottom flange/pipe assembly. The RWG cavity was then sealed at the pipe entrance and the Hi-K cement poured into from the outer end. The act mixing and pouring the Hi-K cement trapped pockets of air in the highly viscous cement mixture. These air pockets were tamped out by hand to the best degree possible. The filling and drying of the RWG cavities was performed one at a time. Each RWG cavity filled with Hi-K cement was allowed to dry for 24 hours in the Tenney environmental test chamber at 38^0C following the provide guidelines [28].

The coupling and excitation assembly, CSRR orifice plate, and bottom flange assembly were bolted together using 50mm long ½-inch machine bolts, washers, and nuts. The complete mechanical drawing sets can be found in Appendix A for the alpha steam quality sensor.

4.5.4 Modeled Alpha Unit Simulation

The changes in dimensions and material of the fabricated alpha model were incorporated into a finalized model. The model CSRR was changed to 12.7mm aluminum without a support bar. The end caps were added and modeled using aluminum from the default CST material library. The Hi-K cement was added with a dielectric constant and complex loss tangent of 0.02 with a constant fit tangent model. Two types of simulations were run. The first simulation presented below is to describe the behavior of the alpha unit should it encounter a uniform distribution of steam with qualities ranging from 0.1 to 1. The second model should mimic the behavior observed when a uniform air and water mixture of mass ratios between 0.3 and 1 are flowing through the pipes. The model is designed to handle a radially stratified steam quality distribution discretized to 4 layers. The two models differ in the material contained in the model pipe and rings, but both models presented assume a homogenous and uniform distribution of material permittivity.
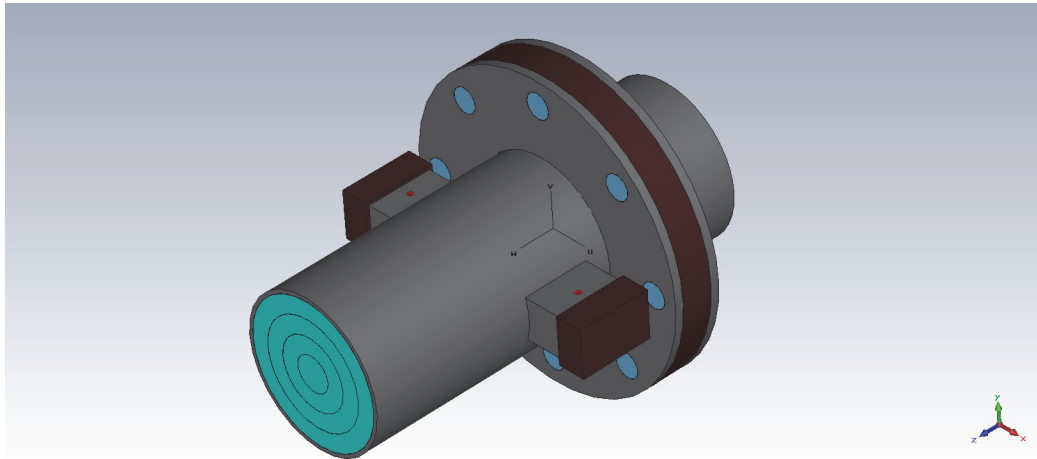
Fig. 89: Alpha with Support Bar Model Geometry
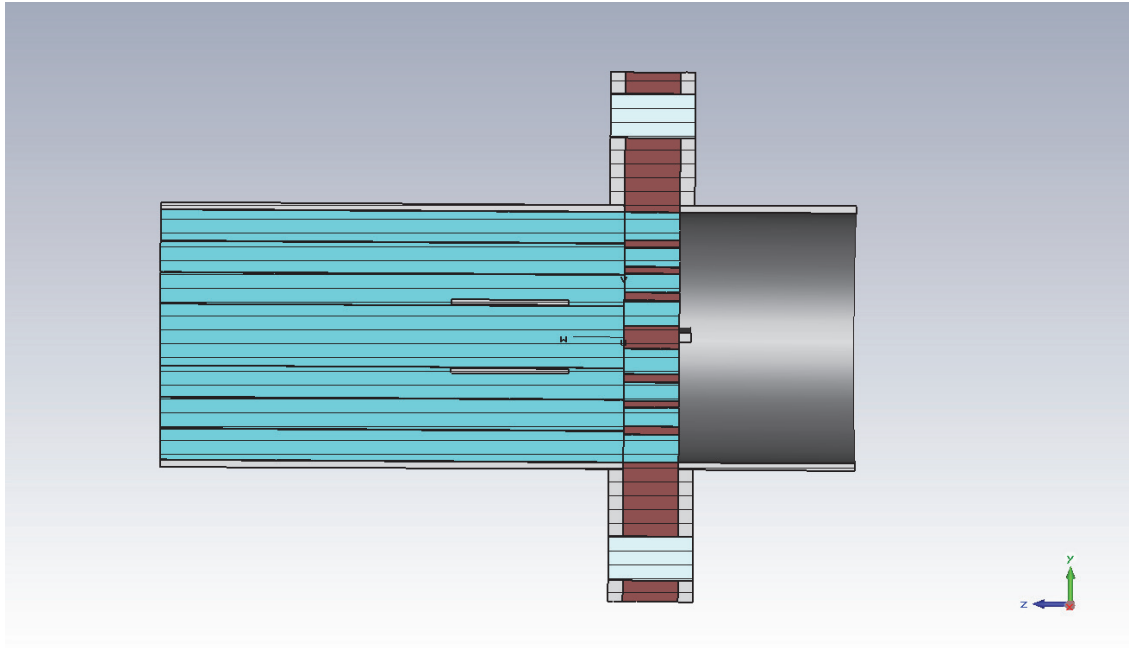
Fig. 90: Alpha - SQS Longitudinal Side View
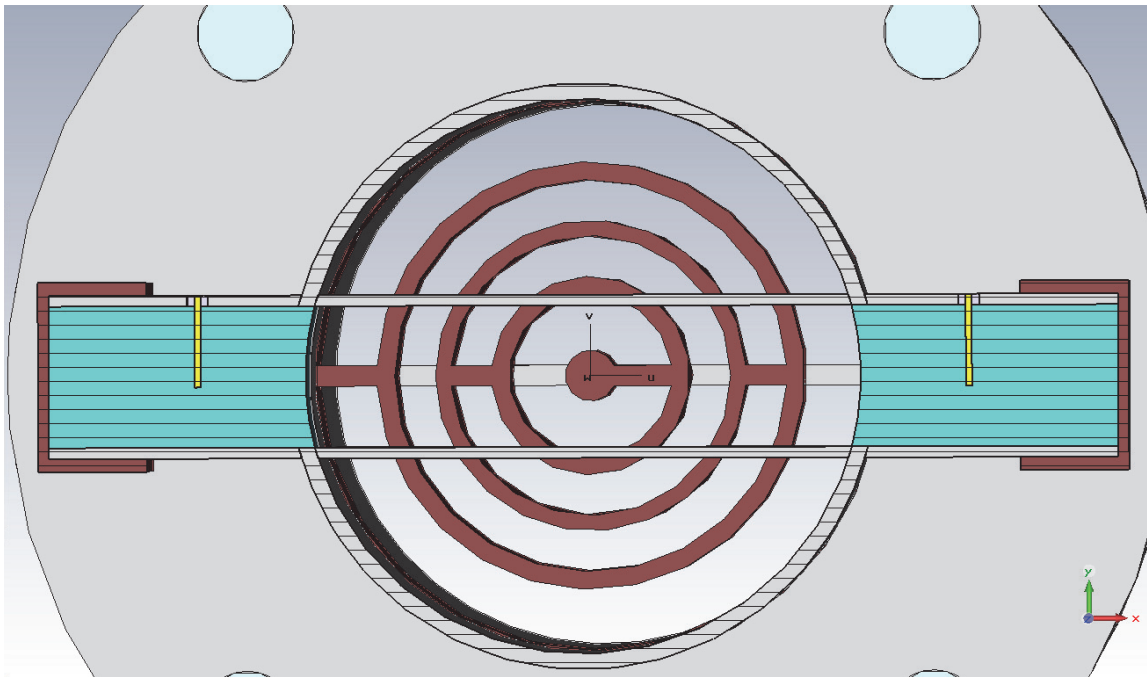
Fig. 91: Alpha - SQS Top View
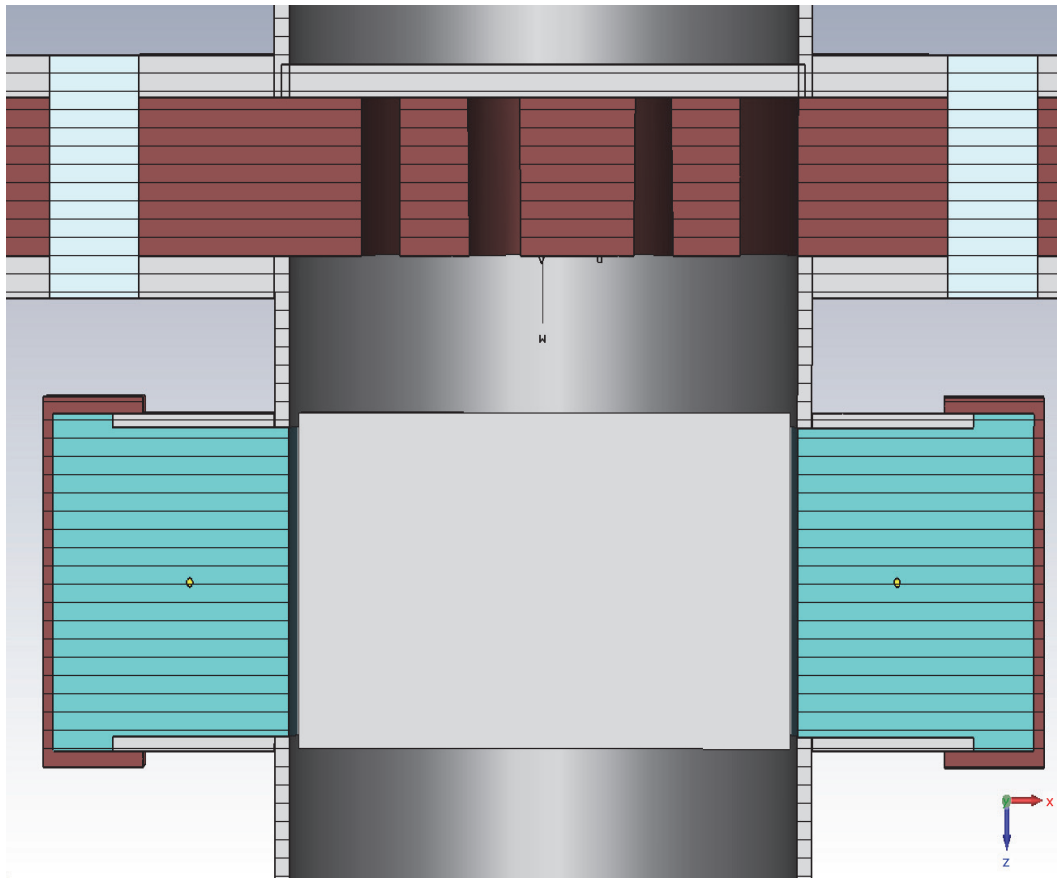
Fig. 92: Alpha - SQS Top Side View
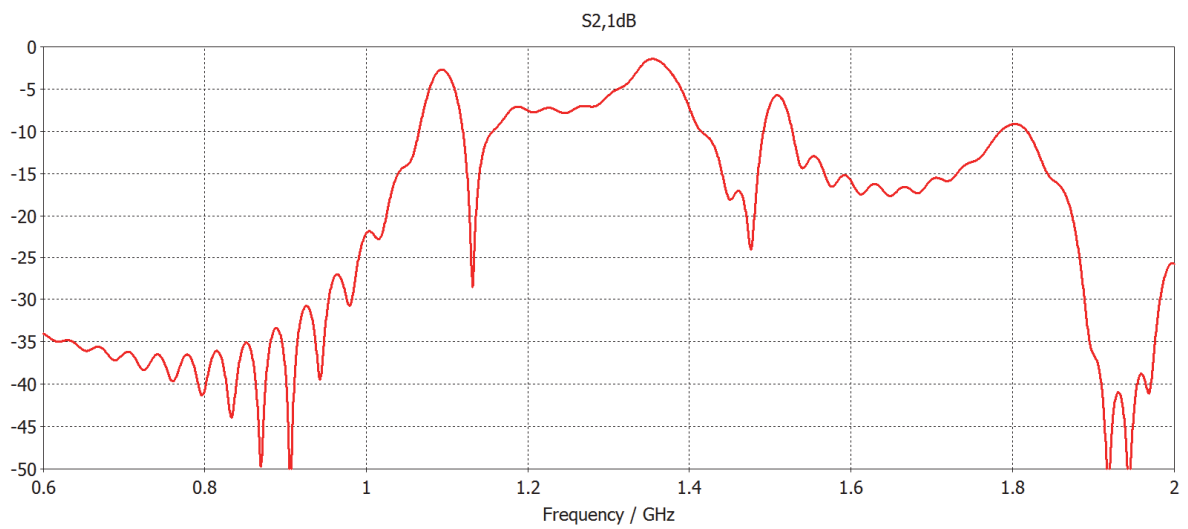
Fig. 93: Simulated |S21| Alpha Unit in Air ½-Inch AL6061 CSRR
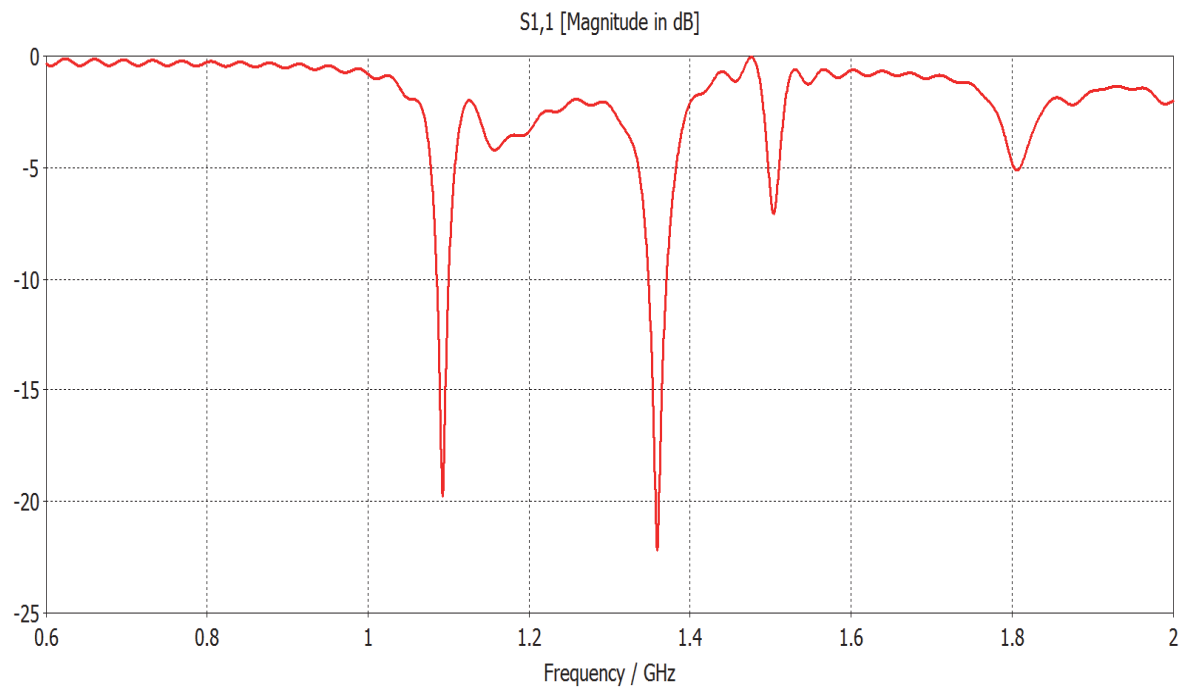
Fig. 94: Simulated |S11| Alpha Unit, In Air ½-Inch AL6061 CSRR
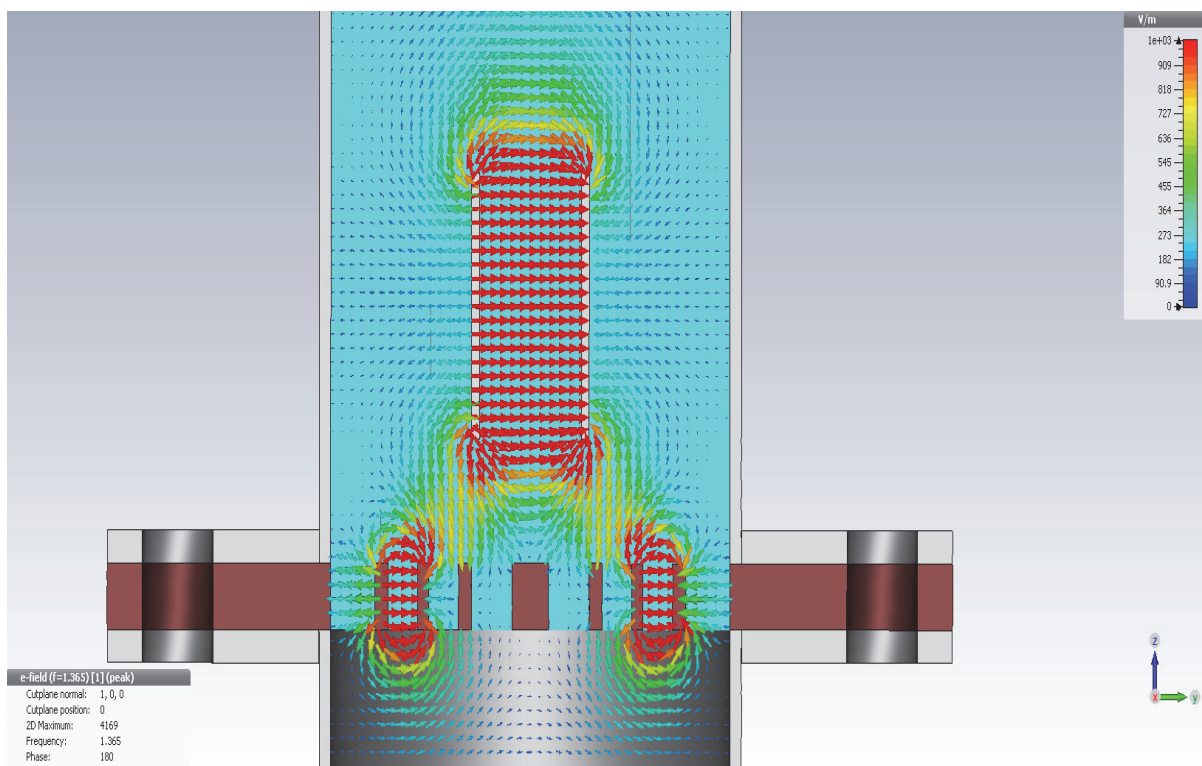
Fig. 95: E-Field @ 2nd Null (1.365GHz), Alpha in Air ½-Inch CSRR

97
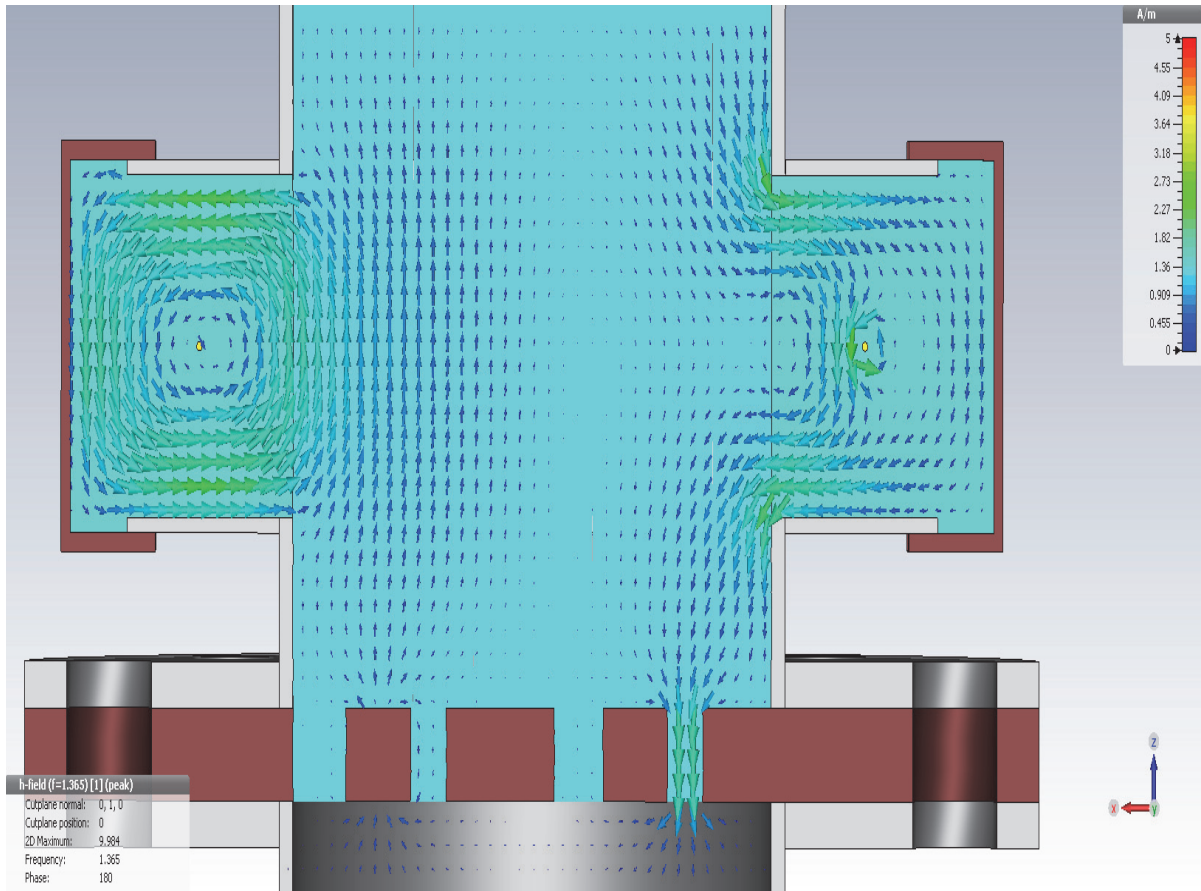
Fig. 96: H-Field @ 2nd Null (1.365GHz), Alpha in Air ½-Inch CSRR

The air only simulations were promising with the CSRR coupling nicely to the PPWG was resonances and an acceptable reflection coefficient. A simulation varying steam quality was performed next. The permittivity of the process steam was determined using the (4) given the density of liquid phase steam was 885kg/m^3 with a permittivity of 38.2. The vapor phase steam had a density of 5.31kg/m^3 and a permittivity of 1.00785. These values correspond to saturated steam at 175^0C and 1.03MPa. The modeled steam was swept in quality from 10% to 100% in increments of 10%.
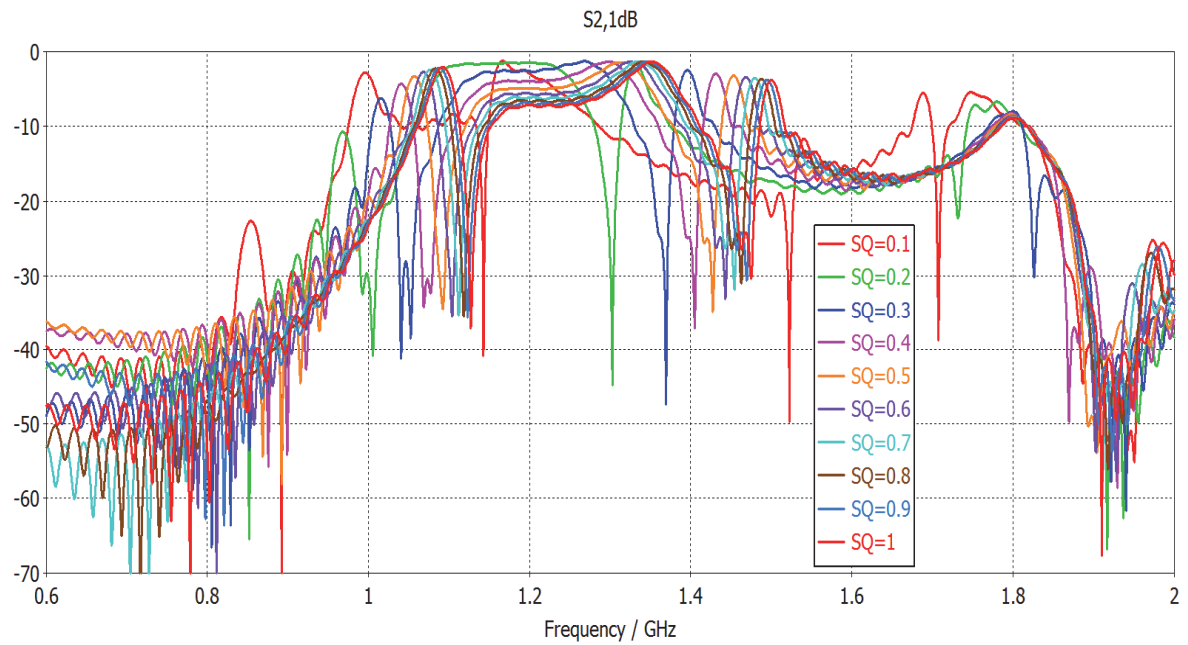
Fig. 97: Simulated |S21| Alpha SQS Steam Quality Sweep 10% to 100%
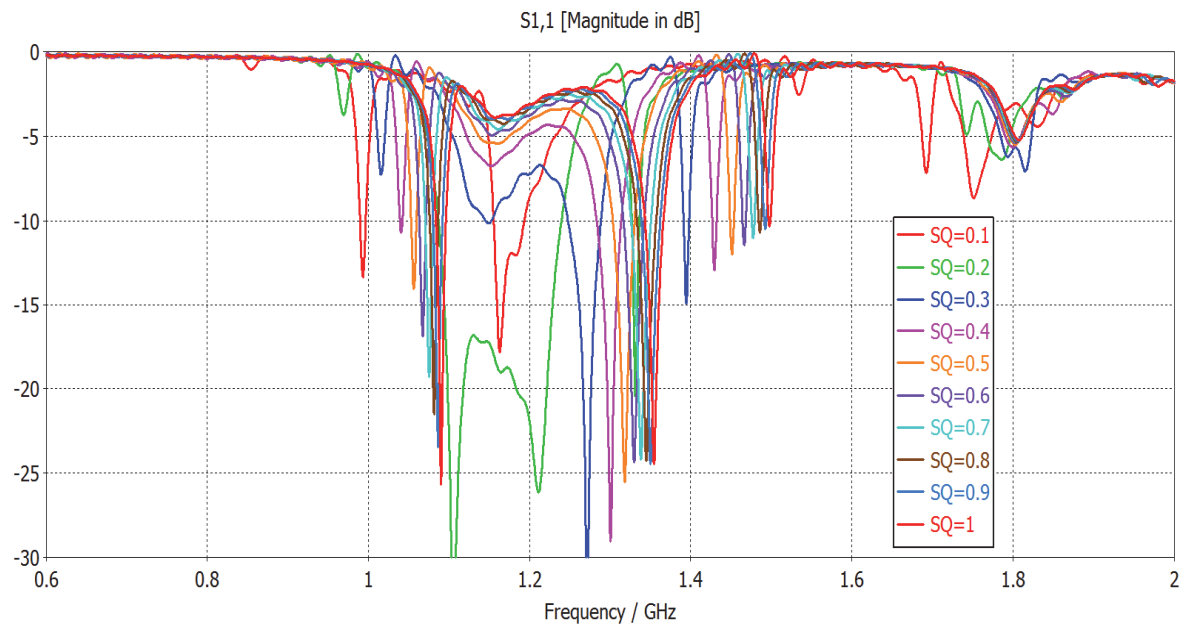
Fig. 98: Simulated |S11| Alpha SQS Steam Quality Sweep 10% to 100%

99
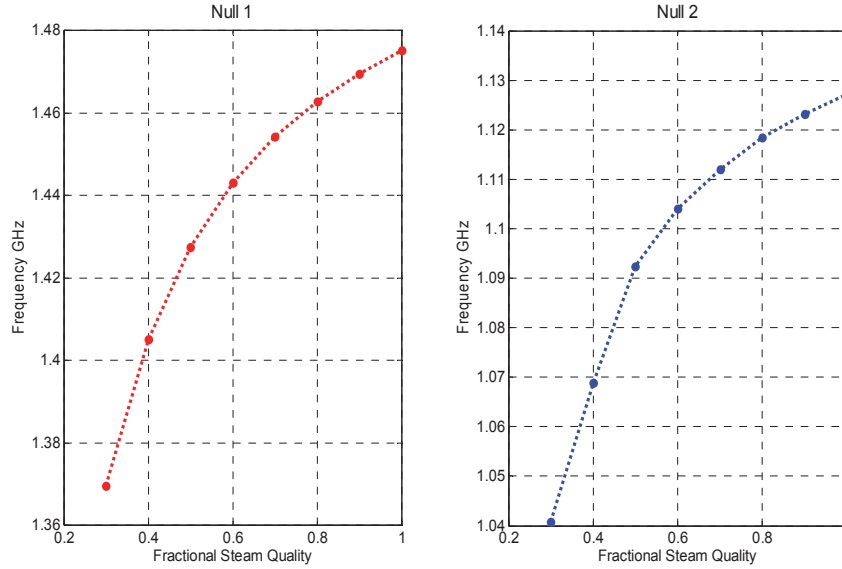
Fig. 99: SQ |S21| Frequency Tracking on 1st and 2nd Nulls using Steam

Another simulation was run changing the component densities and permitivitties to provide a basis of comparison for the CST model verses the measured results that used air and water mixed according to (4). The density of water used was 995kg/m^3 with a static real permittivity of 74.4 at 35^{0}C assuming an atmospheric pressure of 101kPa. The air was modeled as dry air with density 1.19kg/m^3 with real static permittivity of 1.0006 at 20^{0}C and 101kPa. The simulated results for the S11 and S21 of the alpha SQS using air and water are shown in Fig. 100 and Fig. 101, respectively. The mass ratio between the air and water-air mixture was varied between 30% and 100%.

Simulation results can be compared directly using Fig. 103 to observe the difference in permittivity between air-water and steam at the same vapor or steam quality. The smaller permittivity and lower density of air compared to steam in the vapor state at 1.03MPa/175C results in a much lower permittivity at the same quality. Thus the air-water method of testing produces smaller mixture permittivities which are more indicative of higher quality steam than originally expected. If well dispersed and homogenous air-water mixtures can be

produced, the air-water test is a good method for permittivity modeling of saturated steam at high qualities.
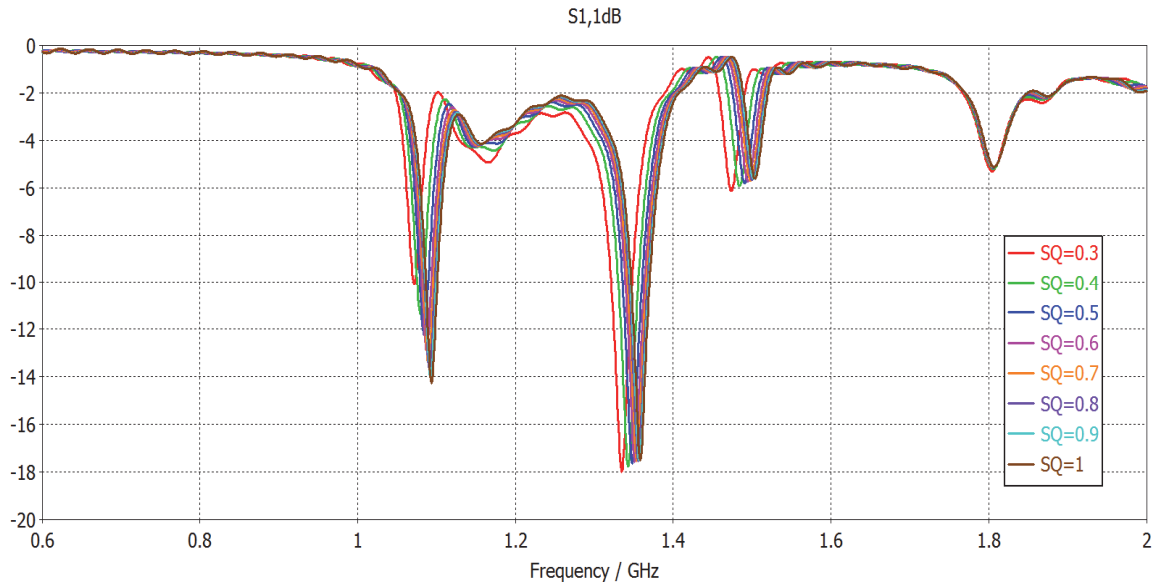
Fig. 100: Simulated |S11|Alpha SQS, VME using Water and Air
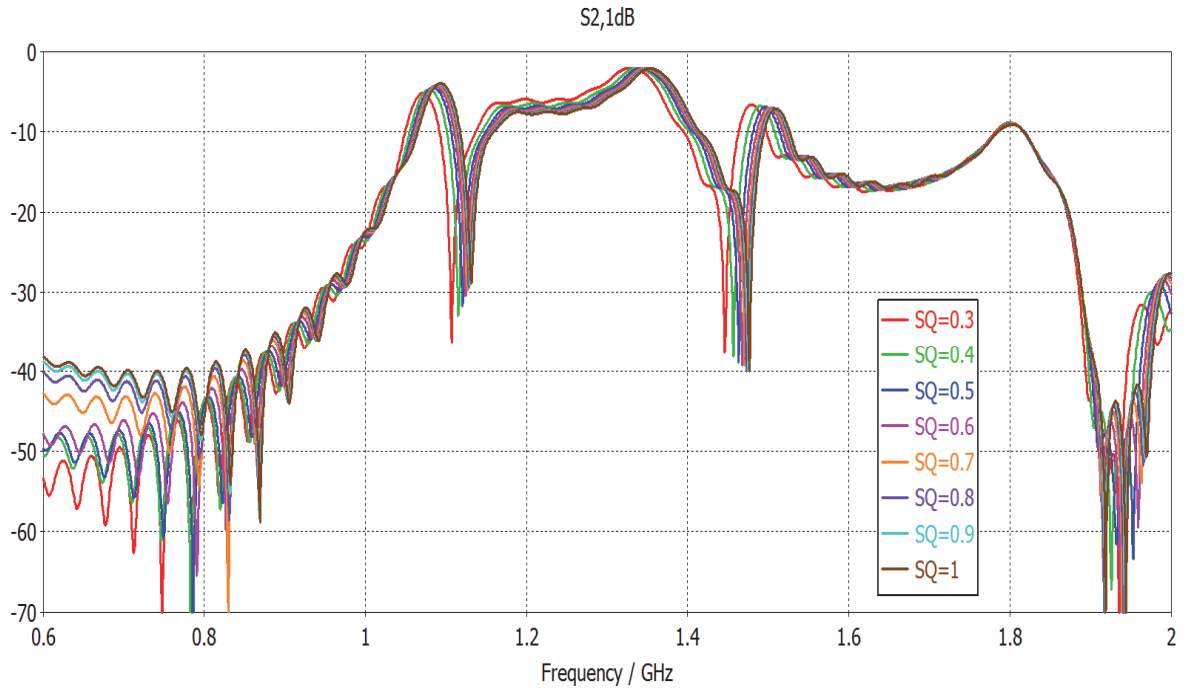
Fig. 101: Simulated |S21|Alpha SQS, VME using Water and Air
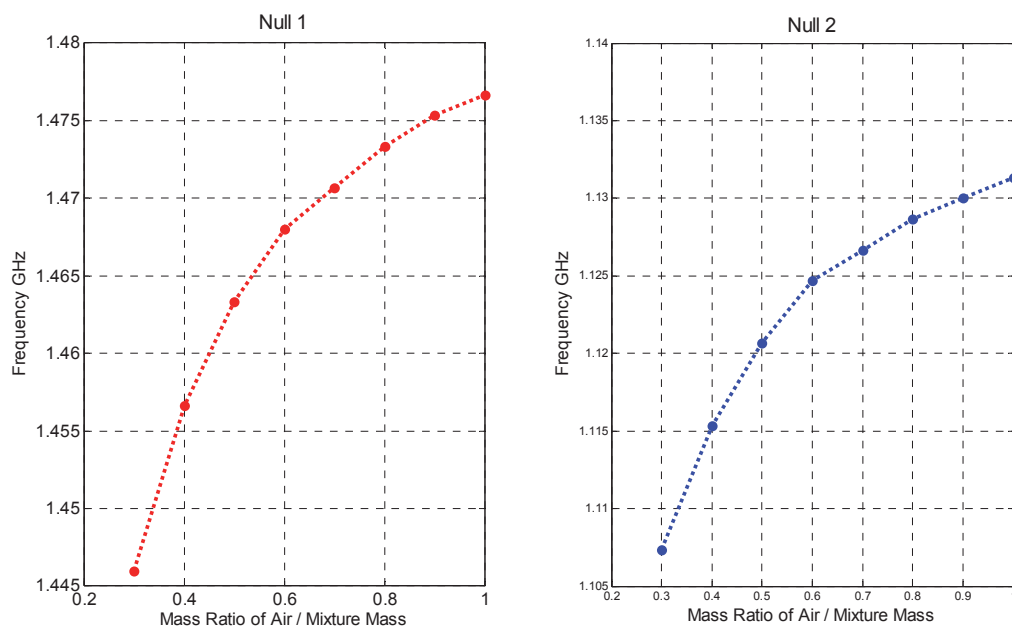
Fig. 102: Air-water quality S21 Null Tracking on 1st and 2nd Nulls using Air/Water
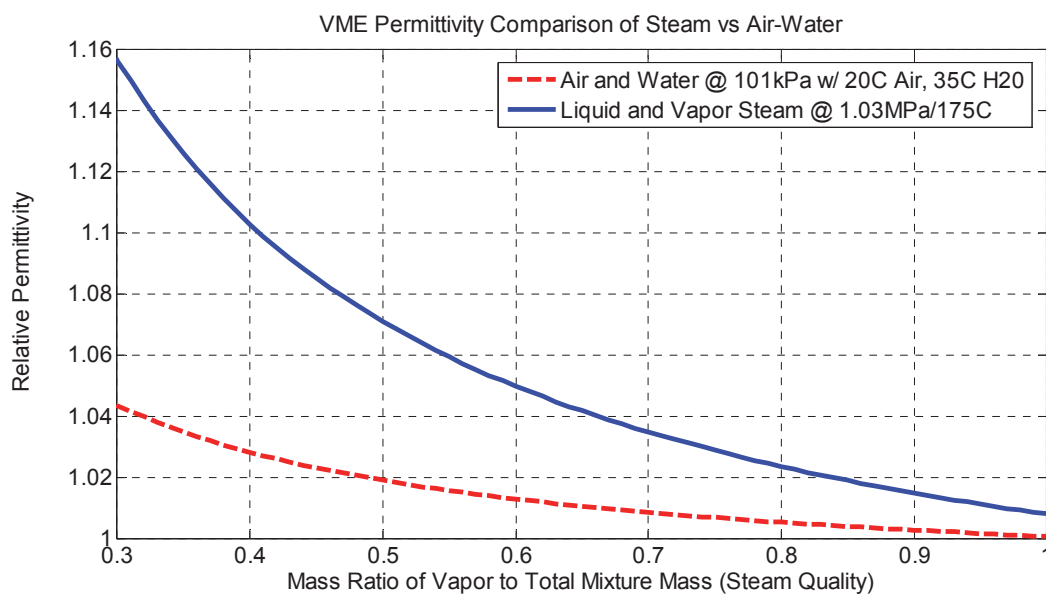
Fig. 103: Resultant Permittivity of Air-Water and Steam Mixtures using the VME

4.6 Alpha Unit Measurement

Testing for the alpha model SQS was done on the same air-water apparatus as the proof of concept measurements. The water flow monitoring did receive a much needed upgrade as a FGM82 low flow magnetic flow meter made by Omega was purchased and installed. The magnetic flow meter allowed a water flow accuracy of 1% full scale or a 0.03 GPM lower limit greatly reducing the flow rate uncertainty of the experiment.

Prior to measurement with the air-water test apparatus, the SQS was measured in air. The measurement showed poorer null quality than expected. It was possible that the poor null depth could be caused by fields normally contained within the CSRR fringing to the outside of the pipe because of the short bottom pipe length. The SQS was moved to add additional pipe length below the bottom flange's pipe section as shown in Fig. 104. The SQS's larger size did require some movement of apparatus's vertical PVC piping in order to fit a coupler to add the additional piping correctly. The vertical distance from the CSRR to the point of water injection was reduced from 81.3cm to 61cm as a result of the extended bottom pipe. The original 100mm length pipe on the bottom flange had not been long enough to attenuate the fringing or radiating fields from coupling into the material near the pipe end. The magnitude response of the CSRR resonances greatly improved upon extending the pipe length downstream of the CSRR as shown in Fig. 105.

Fig. 104: SQS with Bottom Pipe Extension
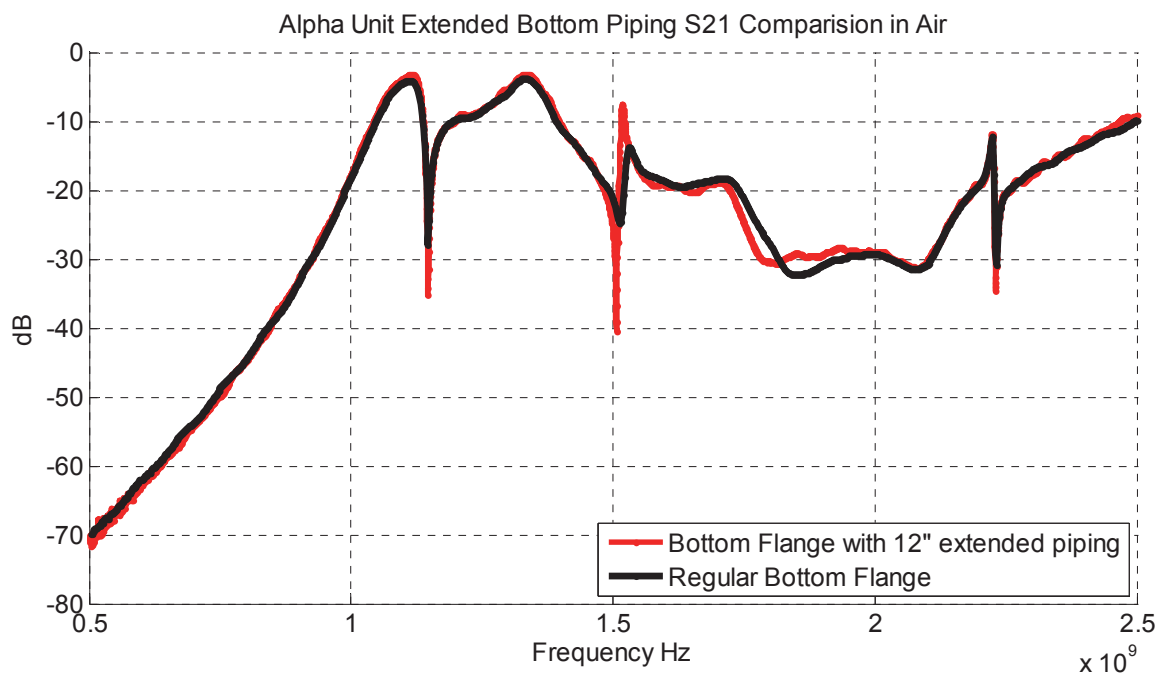
Fig. 105: Measured Alpha S21 in Air, Bottom Pipe Length Comparison
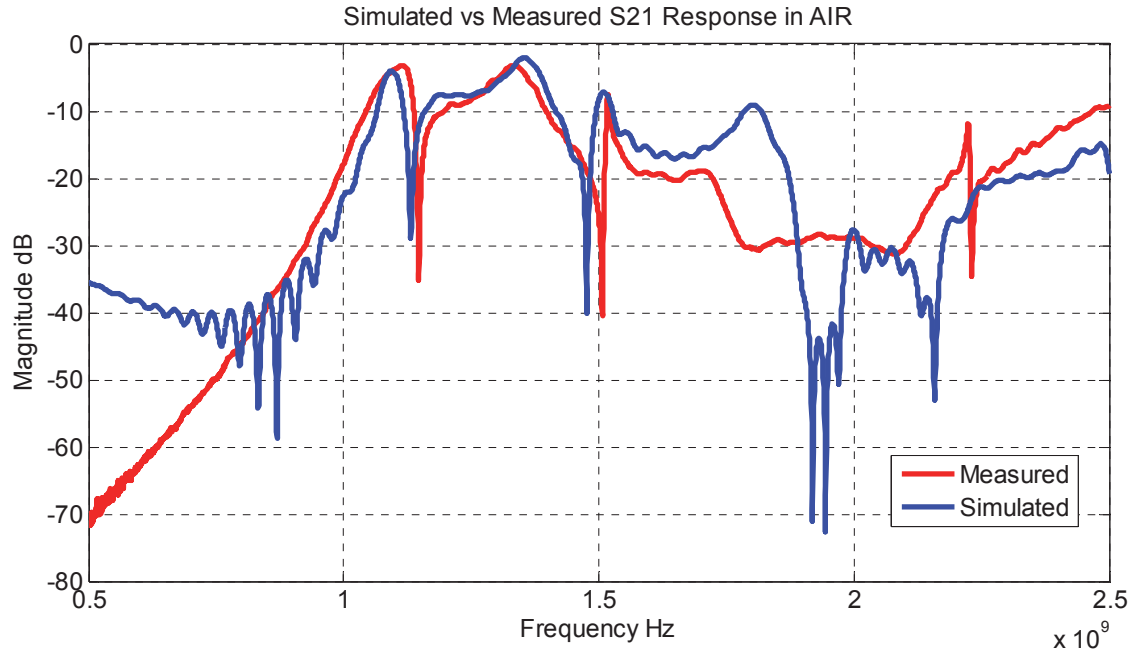
Fig. 106:|S21| of Measurement vs Simulation SQS in Air

Table 13: Simulated Verses Measured 1st and 2nd Null Frequencies

Simulated Null Frequency	Measured Null Frequency
1.131GHz	1.149 GHz
1.477 GHz	1.507 GHz

The comparison of the CST model simulated in air and the SQS with the extended

piping in air is shown in Fig. 106. The simulation compares very well with measured

response. The main cause of the model differences less than 1.72GHz or pipe cutoff

frequency is due to dimensional tolerances of the alpha SQS. Above 1.72GHz the response of

the SQS is difficult to predict as energy is allowed to enter and leave the SQS and is

impacted by objects near the SQS pipe ends. Note, a third CSRR resonance is visible in the

measured response that is not immediately observable in the simulated response.

To try to better uniformly distribute the water during testing, a new nozzle was created. The nozzle was designed to spray water perpendicular to the flow of the air in a uniform circular distribution. It was thought that this would be optimal method to produce an even distribution of the water across the CSRR. The VNA was set to take 4001 frequency points across a 500MHz to 2.5GHz bandwidth. The IF Bandwidth of the VNA was set at 5 kHz and the number of averages to 16.A reflection and transmission calibration was performed on the VNA before the SQS was connected. It took the VNA just under one second to perform a frequency sweep.

Fig. 107: Radial Spray Water Nozzle
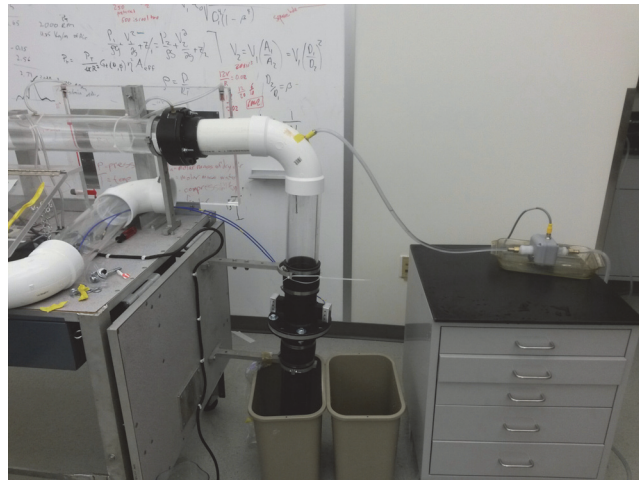
Fig. 108: Modified Air-Water Apparatus with Magnetic Flow Meter

The first round of test results show the new nozzle was not able to disperse water at the lower air flow rate as effectively as the straight tube injection method did at the higher air flow rates. The first data set also showed that high averaging was needed to reduce the process noise caused by the non-homogeneity of the water in the flowing air being channeled through the different rings at more random intervals. Process noise for the air-water test apparatus is given as the random distribution of the water flow through each ring of the CSRR during a measurement a specific water flow rate. A reduction of the samples the VNA averages is also at fault for the poor results as the previous POC measurements were averaged over 1 min as compared to this measurement set's averaging of 15 seconds. The test was unable to average the water flow enough to approximate steam permittivity with the air-water mixture.
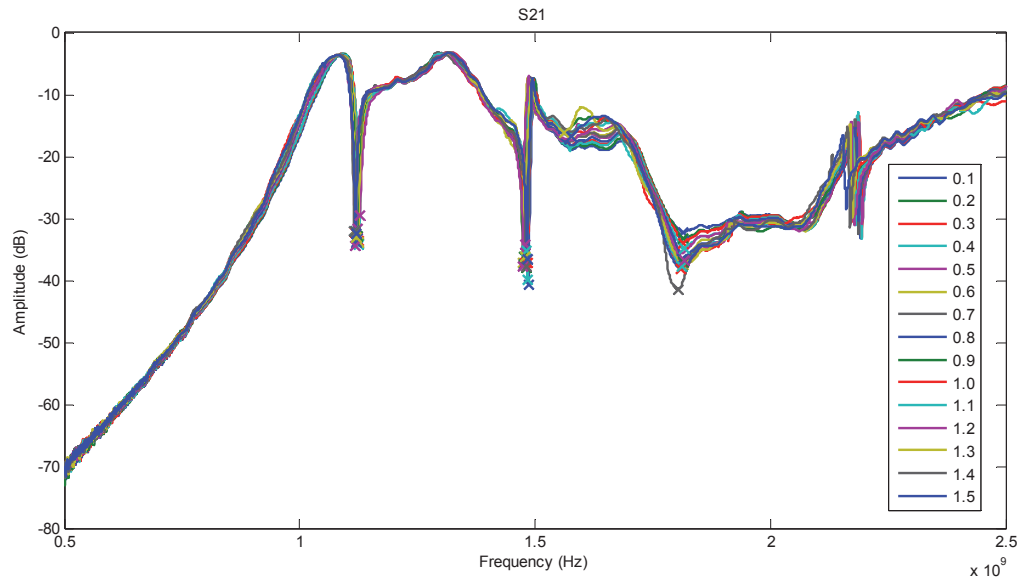
Fig. 109: Measured |S21| of Different Water Flow Rates of 1st Round Measurements
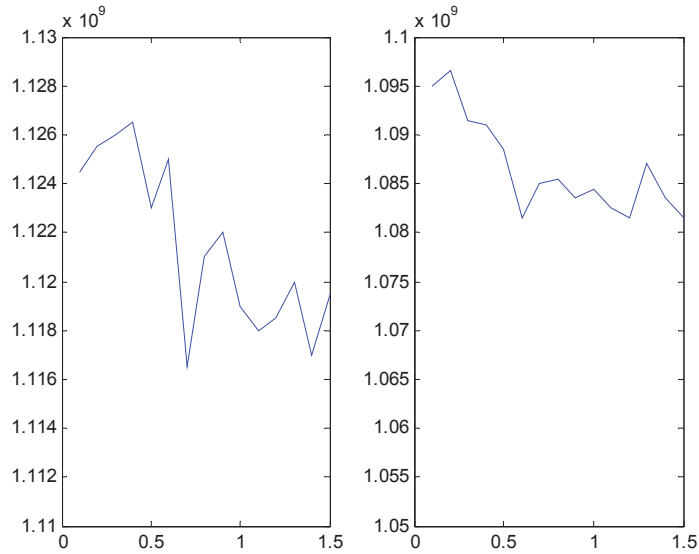
Fig. 110: High Process Noise looking at the 1st null and peak of the data

A second set of data was acquired adjusting the VNA settings to increase the number

of samples averaged to reduce the effects of process noise. By increasing the IFBW on the

VNA to the maximum of 100 kHz, performing only a through calibration, and increasing the

averaging to 200 samples the measurement was better able to reduce the process noise. The

fan speed of ~3290RPM was used to increase air velocity and improve water dispersion

during the measurements which resulted in an approximate air mass flow rate of 0.15kg/s.

The test was run again taking SQS spectrum measurements every 0.1GPM from 0.1GPM to

1.5GPM. The frequency response of the SQS was checked during the experiment and some

of the water flow rates repeated to reduce the number of data outliers from the normal linear

progression of frequency shift.

During the test, the volumetric air flow rate varied between 7.589m^3/min and 7.787

m^3/min depending upon the height of the water in the water collecting bin beneath the SQS.

The water in the bin was continuously emptied by hand, but at water flow rates exceeding

1.0GPM the water level would rise rapidly which dropped the air flow rate to the minimum

7.589m^3/min. The ambient air temperature was 22^{0}C causing the air density to be

approximately 1.19kg/m^3. Thus, the approximate mass air flow rate varied between

0.1505kg/s to 0.1544kg/s. The 4.1g/s air mass flow variation is a small amount which only

induces a maximum 0.6% mass ratio variation for a constant water flow rate. The water used

was cold tap water from the laboratory faucet with an approximate temperature of 20^{0}C. Fig.

111 shows the measured S21 of the second set of data where the flow rate of the water is

given in GPM.

Fig. 111: |S21| SQS - 0.1GPM to 1.5GPM Data Set #2
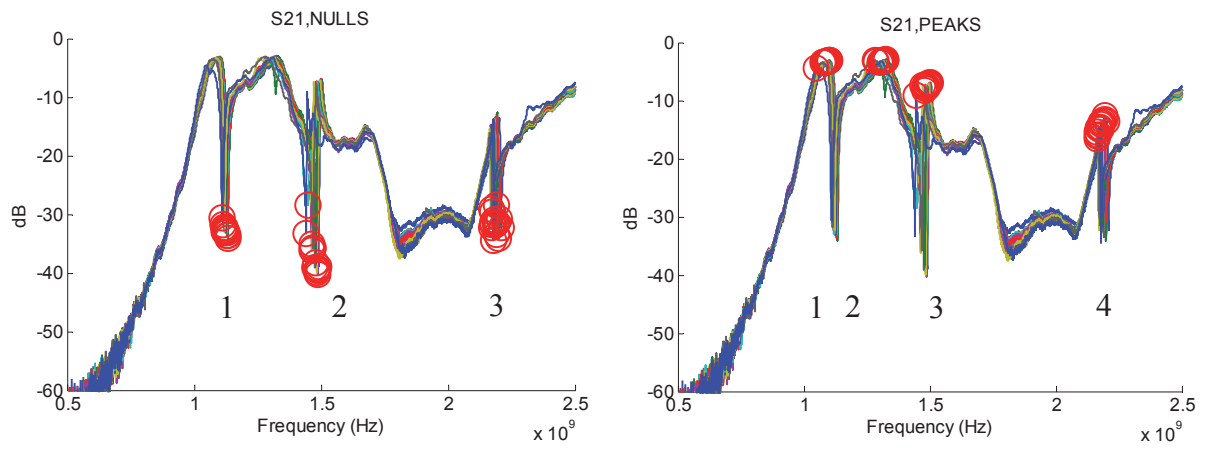
Fig. 112: Null and Peak Tracking on Data Set #2
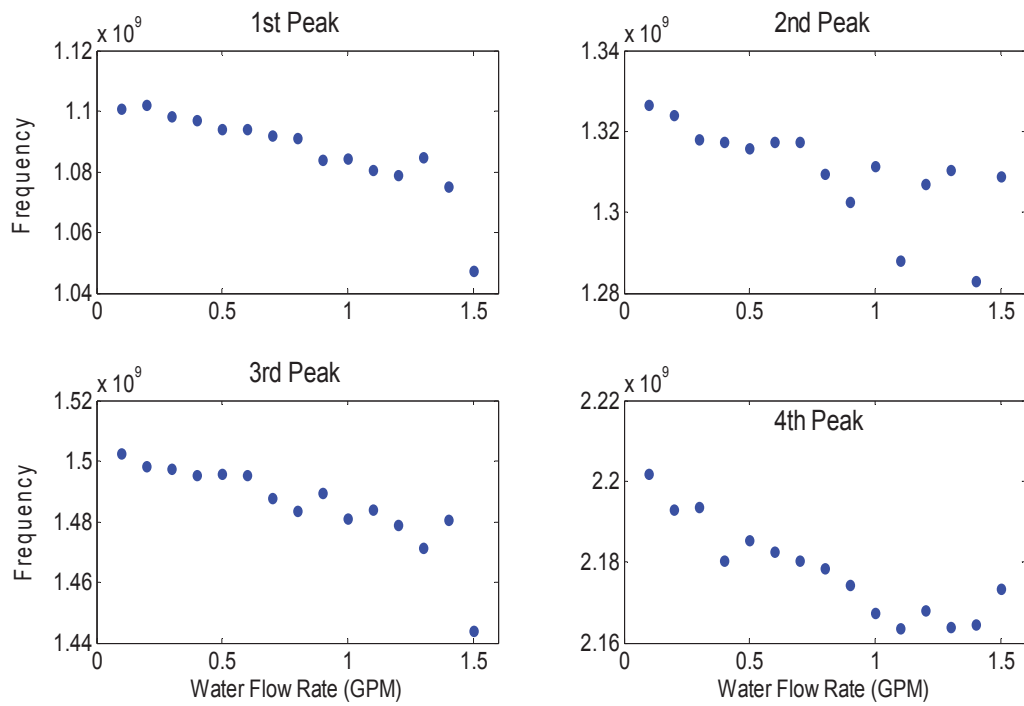
Fig. 113: SQS Measurement Peak Tracking

110
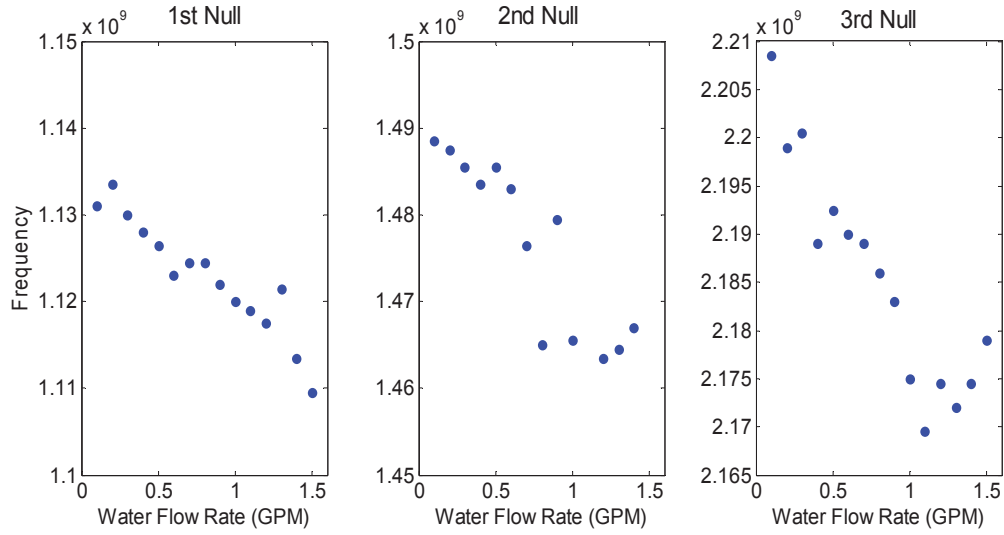
Fig. 114: SQS Measurement Null Tracking

The S21 frequency response had features that shifted lower in frequency with the increasing water flow rate. These features are classified as nulls or local minimums in the transmission or peaks local maximums. Fig. 112 shows the locations of the nulls and peaks which are caused by CSRR ring resonances. The frequency position of the nulls and peaks were then plotted against the water flow rate at the time of measurement. The four peak frequencies are tracked against water flow rate in Fig. 113, while the tracking of the three null frequencies is shown in Fig. 114. The linear relationship of the water flow rate is more apparent in of the peak and null position than others. The linear nature of the feature shifts is expected to be linear with small changes in permittivity, behaving in a more polynomial fashion with larger permittivity changes. To gauge the extent the null or peak frequency response was related in a linearly to water flow rate the coefficient of correlation or R^2 value was calculated for each feature. The values are shown in Table 14.

Table 14: SQS Measurement Data Set #2 R^2 Values

S21 Null/Peak	R^2 value
Peak 1	0.7560
Peak 2	0.5581
Peak 3	0.7335
Peak 4	0.8072
Null 1	0.8950
Null 2	0.7351
Null 3	0.8187

The R^2 values for the most part show good correlation though process noise is still an issue with peak 2 and null 2. The 1st and 3rd nulls show very strong correlation to water flow. It is postulated that the inconsistent and inhomogeneity of the water flow is at fault. The variation in water flow passing through CSRR gaps is too variable with current water dispersion methods used in the air-water apparatus.

Another set of data was collected over a smaller range of water flow. The low flow experiment varied water flow from 0.05GPM to 0.4GPM to better simulate high quality saturated steam. The null shifts are shown against varying water flow rate for the low flow test are shown in Fig. 115. The peak shifts are shown in Fig. 116.

The fine water quality variations were observable using the SQS. The measurement showed good agreement between the shift in the peaks and nulls with varying water flow rate based upon R^2 values shown in Table 15. The most correlated feature shifts with water flow rate were peak 1 and null 1.That is expected as the gap of ring 4 of the CSRR has the largest area opening and thus passes the majority of the air and water flow.
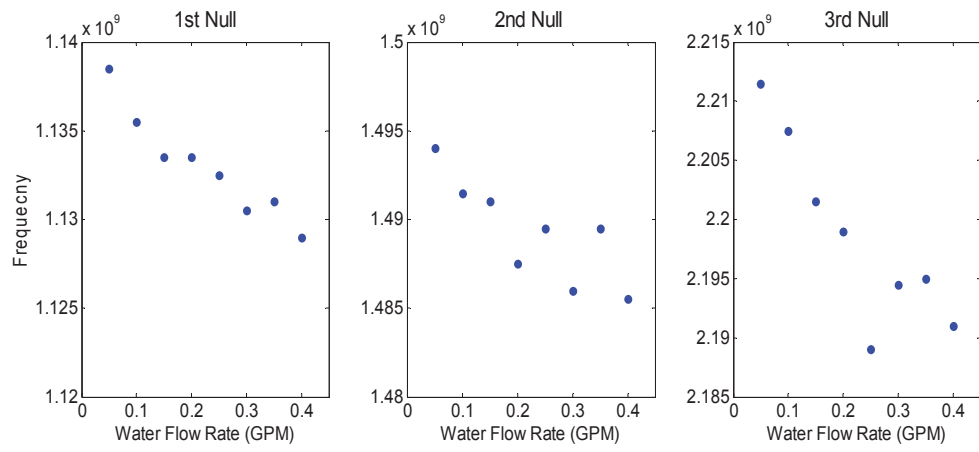
Fig. 115: SQS Measured Null Shift with Low Water Flow
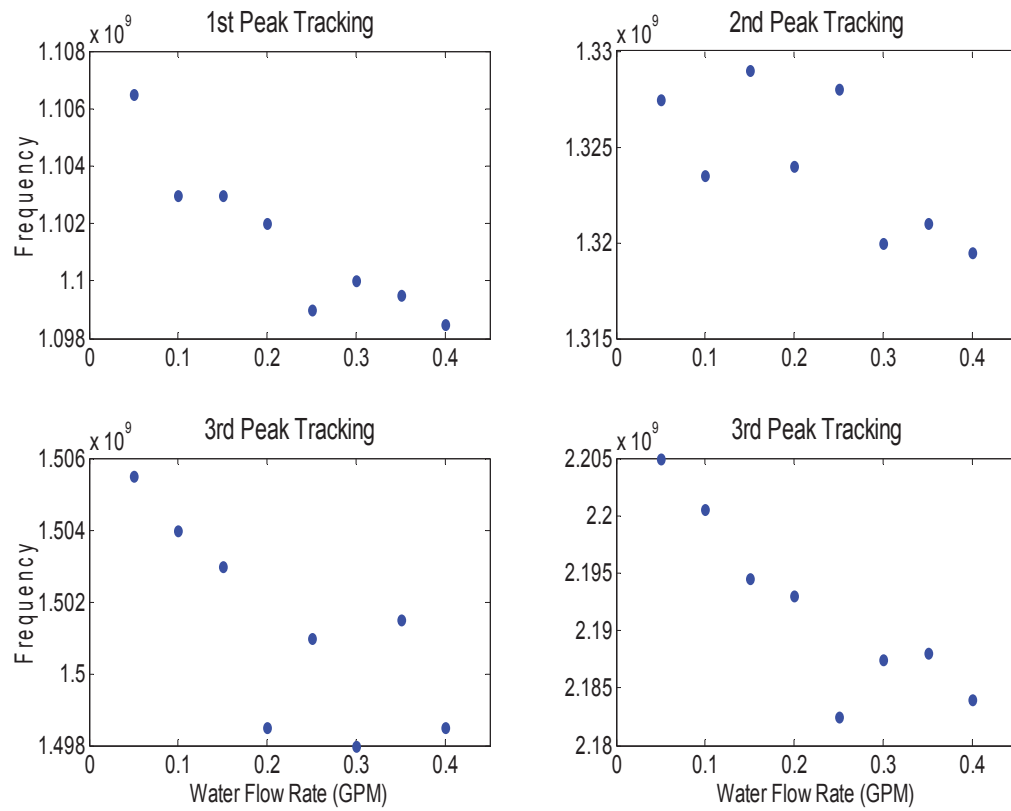
Fig. 116: SQS Measured Peak Shifts with Low Water Flow

113

Table 15: R^2 Values for SQS Null and Peak Shift from Low Flow Dataset

S21 Null/Peak	R^2 value
Peak 1	0.8653
Peak 2	0.4884
Peak 3	0.6206
Peak 4	0.8131
Null 1	0.9407
Null 2	0.7115
Null 3	0.7960

A final calculation was done to equate the permittivity of the air-water mixture used in the SQS measurements to that of saturated steam. Table 16 provides a list of the equivalent steam quality of the measurements modelled by the variable water flow rate used. The equivalent steam quality was calculated for saturated steam at 175^0C and 1.03MPa. The steam quality listed in the fourth column was determined by calculating the equivalent permittivity of the measurements air-water ratio and comparing it the expected permittivity of saturated steam at 175^0C and 1.03MPa. The calculations used 20^0C water with a permittivity of 80 and density 1000kg/m^3. The air was calculated as air with density 1.19 kg/m^3 and static permittivity of 1.001. The mass flow rate of the dry air was set to 0.1544kg/s based upon the experimental differential pressure measurement 946.8Pa across the 3.014-inch OP on the air-water test apparatus. This calculation assumes a homogeneous and uniformly distributed flow through the pipe and the rings of the CSRR.

The measurement shows that the SQS is more than capable of very fine detection of permittivity shifts in the steam quality using the resonance of the CSRR rings. The SQS is

capable of detecting 0.0008 relative permittivity shifts in the steam using the first position of

the first null with an average frequency shift of around 1MHz.

Table 16: Water Flow Rate to Steam Quality at Equivalent Permittivity

Water Flow Rate	Air Flow Rate to Air-Water Flow Rate	Effective Relative Permittivity of Air-Water Mixture	Steam Quality at Equivalent Permittivity
0.0063 kg/s (0.1GPM)	0.9608	1.0018	>100% *
0.0126 kg/s (0.2GPM)	0.9245	1.0026	>100% *
0.0189 kg/s (0.3GPM)	0.8908	1.0034	>100% *
0.0252 kg/s (0.4GPM)	0.8596	1.0041	>100% *
0.0315 kg/s (0.5GPM)	0.8304	1.0049	>100% *
0.0379 kg/s (0.6GPM)	0.8032	1.0057	>100% *
0.0442 kg/s (0.7GPM)	0.7776	1.0065	>100% *
0.0505 kg/s (0.8GPM)	0.7537	1.0073	>100% *
0.0568 kg/s (0.9GPM)	0.7312	1.0081	99%
0.0631 kg/s (1.0GPM)	0.7100	1.0088	98%
0.0694 kg/s (1.1GPM)	0.6900	1.0096	97%
0.0757 kg/s (1.2GPM)	0.6711	1.0104	96%
0.0820 kg/s (1.3GPM)	0.6531	1.0112	95%
0.0883 kg/s (1.4GPM)	0.6362	1.0120	94%
0.0946 kg/s (1.5GPM)	0.6201	1.0128	93%

indicative of superheated steam

CHAPTER FIVE

Culmination and Reflection

This work culminates with a design that shows the capability to meet the needs of in-line steam quality measurement in a simulated steam loop. The SQS was taken from a theoretical idea to design then implementation that was able to perform well given the budgetary compromises made. The alpha SQS was constructed on a budget of under $300 and performs very well considering. It was able to attain a simulated 1% steam quality reading and was able to detect permittivity shifts expected from steam in the superheated range. The following are reflective notes on potential topics of future research and sensor development.

A beta model should address the design from a more mechanical perspective with focus on the effect the CSRR has on the flow on of the steam to verify that it can be used as an orifice plate substitute for differential pressure measurement. The SQS would benefit from a new CSRR design with a lower beta for improved permittivity sensitivity. The high beta aluminum version, while functional, provides the bare minimum sensitivity to permittivity changes and is therefore quite susceptible to process noise .The reduction of the gaps between the rings would intensify the electric fields between the rings lending to larger frequency shifts with smaller changes in the permittivity of the material in the gaps. It may be difficult to have a CSRR that is both "high beta" and very sensitive as they proportional and inversely proportional to the size of the gaps between the rings. The choice of CSRR beta should ultimately be determined by the minimum accepted value a customer will accept.

Further investigation into the modeling of steam should be conducted. The real permittivity of steam is able to be modeled though use of the volumetric mixing equation but is unable to account for mixing of vapor and liquid steam's imaginary permittivity components. These effects may not play a large role at low temperature and low frequency, but should be developed for a more complete model of impurities in the steam used in real systems. Ideally, a low pressure saturated steam system for available for testing and measurement would eliminate the need for robust modeling of the steam and be able to prove-out the performance of the SQS.

The next revision should also take into account the use of graphite gaskets between the flanges and the CSRR. The alpha model of the SQS does not employ the use of gaskets to provide a watertight seal around the CSRR OP and thus leaks at high water flows. The use of conductive graphite gaskets should ensure the CSRR is at the same electric potential as the rest of the SQS.

The next revision should also use either a higher dielectric for loading the RWGs or increase the width such that the RWGs begin to propagate at a lower frequency. It should also be pertinent to redesign the end caps at the back side of the RWGs. The planar back wall of the RWG does not provide a wideband match to the excitation and would be worth investigating to improve the S11 of the SQS. The manner in which the probe connects to the A hermetically sealed connector between the probe and the SMA cable would reduce the likelihood of leakage should the alumina filling the RWG crack or lose seal in the field.

The materials with which the SQS is built need to also be changed to alumina and stainless steel for temperature and corrosion resistance. The use of mild steel is poor and the SQS begins to oxidize rapidly if not dried properly after testing with water. A stainless steel

will mitigate this oxidation as well as provide a stronger structure. Alumina dielectrics should be used in the next revision as well unless a less costly ceramic is obtained Class 150 slip flanges should also.be used.

Ideally the whole structure should be milled from a single disc of stainless steel 8-9cm thick. This would incorporate the CSRR parallel plate waveguides and flanges all into one assembly and allow for easy field installation. This would eliminate many problems and allow the PPWG to move closer to the CSRR for better coupling.

APPENDIX

Mechanical Drawings

R.12

R.16

R1.20

R1.08

R.77

R1.52

R1.65

R2.13

R.20

R.16

R.20

R.63

DETAIL B
SCALE 1 : 1

Multi Ring Orifice
Plate C150 ASME
Mounts

OP Sch 10 4"NPS

DO NOT SCALE DRAWING

A3

SS 316 or AL

UNLESS OTHERWISE SPECIFIED:
DIMENSIONS ARE IN INCHES
SURFACE FINISH
TOLERANCES:
LINEAR ±.00
ANGULAR: ±.00

BREAK ALL
DECK SHARP
EDGES

NAME   SIGNATURE   DATE

DRAWN   Fischer   CF   7/24/13

CHK'D   CF

APPV'D   CF

MFG

Q.A

MATERIAL: WEIGHT:

SHEET 1 OF

SCALE:1:2

Ø 9.00

3.75

B

Ø .75

.94

.04 X 45.00°

Bolt Holes are at
45 degree spacing

0.02
45 degree
chamfer on bolt holes

Optional Thinner
Thickness 0.5

1.25

1.08

2.00

1.83

R.14

R.07

1.62

1.62

Thickness of the Flange does not matter in so long as it is thick enough not to deform when bolts are tightened. 0.25" or thicker is recommended.

.94 Important

Ø.16

1.00

1.14

8.19

Ø.16

2.00

1.00

1.14

7.87

UNLESS OTHERWISE SPECIFIED:

DIMENSIONS ARE IN INCHES
TOLERANCES:
FRACTIONAL±
ANGULAR: MACH± BEND ±
TWO PLACE DECIMAL ±
THREE PLACE DECIMAL ±

INTERPRET GEOMETRIC
TOLERANCING PER:

MATERIAL

FINISH

DO NOT SCALE DRAWING

NAME DATE

DRAWN
CHECKED
ENG APPR.
MFG APPR.
Q.A.
COMMENTS:

TITLE:

CST EXPORT SBJS PWCS - Main Assm

SIZE DWG. NO.   REV

SCALE: 1:1 WEIGHT: SHEET 1 OF 3

NEXT ASSY USED ON

APPLICATION

TITLE:

UNLESS OTHERWISE SPECIFIED:

DIMENSIONS ARE IN INCHES
TOLERANCES:
FRACTIONAL:
ANGULAR: MACH± BEND ±
TWO PLACE DECIMAL ±
THREE PLACE DECIMAL ±

INTERPRET GEOMETRIC
TOLERANCING PER:
MATERIAL
FINISH

DO NOT SCALE DRAWING

NAME   DATE
DRAWN
CHECKED
ENG APPR.
MFG APPR.
Q.A.
COMMENTS:

NEXT ASSY   USED ON
APPLICATION

.08
.50
1.08

Ø9.00
3.75
Ø.75

123

DETAIL A
SCALE 2 : 1.5

Ø.16

1.00
.83
.17

1.00
.83
.17
.34

1.14
.97
.24
.34

Ø.16

Center Conductor Feedthrough
Through Hole use a size 20 drill

Tap these to 2-56
Not necessary to tap all the way through
but metal is only 0.083" thick so it will be unavoidable
These are for mounting screws for a panel mount SMA Connector

UNLESS OTHERWISE SPECIFIED:

DIMENSIONS ARE IN INCHES
TOLERANCES:
FRACTIONAL±
ANGULAR: MACH±   BEND ±
TWO PLACE DECIMAL ±
THREE PLACE DECIMAL ±

INTERPRET GEOMETRIC
TOLERANCING PER:

MATERIAL

FINISH

DO NOT SCALE DRAWING

NAME | DATE
DRAWN | CDF | 11/8/13
CHECKED
ENG APPR.
MFG APPR.
Q.A.
COMMENTS:

SQS-ES
Drill And Tap

TITLE:

SIZE | DWG. NO. | REV
B | SQS PWCS-Main Assm

SCALE: 1:1 | WEIGHT: | SHEET 3 OF 3

NEXT ASSY | USED ON
APPLICATION

Chamfer dimensions aren't important. Chamfer purpose is for easy slide on.

Holes are on both sides

0.88

0.70

R0.09

1.60

2.05

2.30

R0.09

1.30

Thread Hole for 6-32 Machine Screw

Thread Hole for 6-32 Machine Screw

Thread Hole for 6-32 Machine Screw

Holes are on both sides

0.55

1.15

1.75

0.55

0.40

UNLESS OTHERWISE SPECIFIED:
DIMENSIONS ARE IN MILLIMETERS
SURFACE FINISH:
TOLERANCES:
  LINEAR:
  ANGULAR:

FINISH:

DEBUR AND
BREAK SHARP
EDGES

DO NOT SCALE DRAWING

REVISION

NAME   SIGNATURE   DATE

DRAWN   Chris

CHK'D

APPV'D

MFG

Q.A

MATERIAL:

Aluminum

WEIGHT:

TITLE:

Slide On, Set Screw End Cap for SQS

DWG NO.

END CAP Set Screw

SCALE:2:1

SHEET 1 OF 1

A3

125

BIBLIOGRAPHY

[1] J. J. Baum, "Steam Quality, Sampling and Analysis," in *Association of Water Technologies Spring Conference*, Chicago, Not Listed.

[2] Lemmon et. al, "Thermophysical Properties of Fluid Systems," in *NIST Standard Reference Database Number 69, Eds. P.J. Linstrom and W.G. Mallard*, Gaithersburg MD, National Institute of Standards and Technology, 2014, p. 1.

[3] Munson et. al, Funadamentals of Fluid Mechanics, Hoboken,NJ: John Wiley and Sons,Inc., 2009.

[4] B. Jean, "A Microwave Sensor For Steam Quality," *IEEE Transactions on Instrumentation and Measurement,* vol. 57, no. 4, pp. 741-754, 2008.

[5] Fernadez. et. al., "A Database for the Static Dielectric Constant of Water and Steam," 6 1 1995. [Online]. Available: http://www.nist.gov/data/PDFfiles/jpcrd487.pdf. [Accessed 2 1 2014].

[6] Brandon. J. Herrara, *A Low-Cost Pulsed Fourier Transform Network Analyzer,* Waco, Tx: Baylor University, 2011.

[7] J. Bonache, I. Gil, J. Garcia-Garcia and Ferran Martin, "Novel Microstrip Bandpass Filters Based on Complementary Split-Ring Design," *IEEE Transactions on Microwave Theory and Techniques,* vol. 54, no. 1, pp. 265-271, 2006.

[8] D. Pozar, Microwave Engineering, Hoboken,NJ: Wiley and Sons, Inc., 2005.

[9] E. Donaho, J. Tarjan, M. Hagewood, M. Area, D. Clubbs, C. Cruthirds and J. O'Brien, *Centrifugal Fan Test Stand:Laboratory Mode Operations Manual,* Waco,Texas: Baylor University, 2003.

[10] Agilent E5071B Network Analyzer.

[11] CST Microwave Studio 2nd Edition.

[12] Beana. et. al., "Equivalent-Circuit Models for Split-Ring Resonators and Complementary Split-Ring Resonators Coupled to Planar Transmission Lines," *IEEE Transactions on Microwave Theory and Techniques,* vol. 53, no. 4, pp. 1451-1461, 2005.

[13] *Design Guide for High-Speed Controlled Impedance Circuit Boards,* IPC 2141A,1996.

[14] Ortiz. et. al., "Complentary Split-Ring Resonator for Compact Waveguide Filter Design," *Microwave and Optical Technology Letters,* vol. 46, no. 1, pp. 88-92, 2005.

[15] Coorstek, "Ceramic Material Properties," 2013. [Online]. Available: http://www.coorstek.com/resource-library/library/8510-1042_ceramic_material_properties.pdf. [Accessed 5 7 2013].

[16] J. M. Gere and B. J. Goodno, Mechanics of Materials, Stamford,CT: Cengage Learning, 2012.

[17] F. T. Ulaby, E. Michielssen and U. Ravaioli, Fundamentals of Applied Electromagnetics, Upper Saddle River, NJ: Pearson Education, Inc., 2010.

[18] M. Bombay, "Material Characterization Using Complementary Split-Ring Resonators," *IEEE Transactions on Instrumentation and Measurement,* vol. 61, no. 11, pp. 3039-3046, 2012.

[19] Jean et. al., "Meter and Method for In Situ Measurement of the Electromagnetic Properties of Various Process Materials using Cutoff Frequency Characterization and Anaylsis". United States of America Patent 5,331,284, 19 July 1994.

[20] P. Wade, "Rectangular Waveguide to Coax Transistion Design," 10 Nov 2006. [Online]. Available: http://www.w1ghz.org/QEX/Rectangular_Waveguide_to_Coax_Transition_Design.pdf. [Accessed 10 July 2013].

[21] UC Davis, "Waveguide Impedance," 1 09 2008. [Online]. Available: http://www.ece.ucdavis.edu/courses/notes/fall2008/EEC132A/pswd/wgimpedance.pdf. [Accessed 1 7 2013].

[22] S. B. Cohn, "Design of Simple Broad-Band Wave-Guide-to-Coaxial-Line Junctions," *PROCEEDINGS OF THE I.R.E.,* vol. 35, no. 9, pp. 920-926, 1947.

[23] Ferguson Enterprises, Inc., "FNW Flange Dimensions," 2012. [Online]. Available: http://www.fnwvalve.com/FNWValve/assets/images/PDFs/FNW/tech_FLGDIMS.pdf. [Accessed 8 7 2013].

[24] ASME, *Pipe Flanges and Flanged Fittings:NPS 1/2 through NPS 24 Metric/Inch:B16.5,* ASME, 2013.

[25] P-N Designs,Inc, "Waveguide Mathematics," 3 11 2012. [Online]. Available: http://www.microwaves101.com/encyclopedia/waveguidemath.cfm. [Accessed 5 7 2013].

[26] Emerson and Cuming Microwave Products, "Eccostock Hi-K Cement," 2013. [Online]. Available: http://www.eccosorb.com/products-eccostock-hik-cement.htm. [Accessed 2 7 2013].

[27] Ashley Orr, Baylor University Machinist.

[28] Emerson and Cuming, "Eccostock Hi-K Cement Technical Bulletin," 22 8 2012. [Online]. Available: http://www.eccosorb.com/Collateral/Documents/English-US/HiK%20Cement.pdf. [Accessed 5 7 2013].